TU Delft

Delft University of Technology

PV Potential in Urban Environment and Innovative Module Demonstrators

Zhou, Y.

DOI
10.4233/uuid:389613f2-8c94-4213-8bea-d7ffd05bd4ff

Publication date
2025

Document Version
Final published version

Citation (APA)
Zhou, Y. (2025). *PV Potential in Urban Environment and Innovative Module Demonstrators*. [Dissertation (TU Delft), Delft University of Technology]. https://doi.org/10.4233/uuid:389613f2-8c94-4213-8bea-d7ffd05bd4ff

Important note
To cite this publication, please use the final published version (if applicable).
Please check the document version above.

Copyright
Other than for strictly personal use, it is not permitted to download, forward or distribute the text or part of it, without the consent of the author(s) and/or copyright holder(s), unless the work is under an open content license such as Creative Commons.

Takedown policy
Please contact us and provide details if you believe this document breaches copyrights.
We will remove access to the work immediately and investigate your claim.

This work is downloaded from Delft University of Technology.
For technical reasons the number of authors shown on this cover page is limited to a maximum of 10.

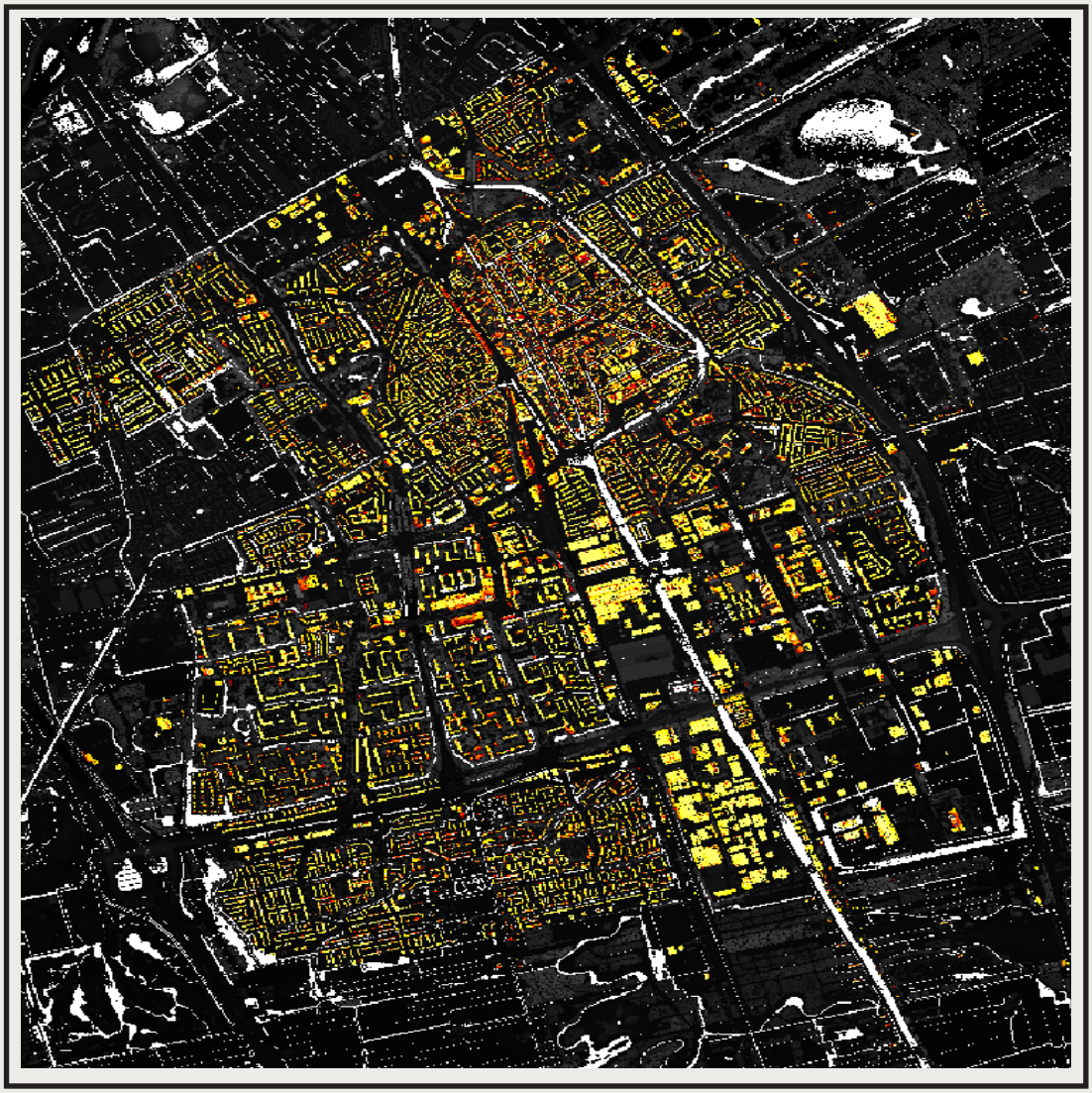

PV Potential in Urban Environment and Innovative Module Demonstrators

YILONG ZHOU

PV Potential in Urban Environment and Innovative Module Demonstrators

Yilong ZHOU

周逸龙

PV Potential in Urban Environment and Innovative Module Demonstrators

Dissertation

for the purpose of obtaining the degree of doctor
at Delft University of Technology,
by the authority of the Rector Magnificus Prof.dr.ir. T.H.J.J. van der Hagen,
Chair of the Board for Doctorates,
to be defended publicly on
Thursday 16 October 2025 at 10:00

by

Yilong ZHOU

Master of Science in Sustainable Energy Technology,
Delft University of Technology, the Netherlands,
born in Hunan, China.

This dissertation has been approved by the promotors.

Composition of the doctoral committee:

Em. prof. ir. P.G. Luscuere	chairperson
Em. prof. dr. ir. M. Zeman	Delft University of Technology, promotor
Prof. dr. ir. O. Isabella	Delft University of Technology, promotor
Dr. ir. H. Ziar	Delft University of Technology, copromotor

Independent members:

Prof. dr. ir. P.J.M. van Oosterom	Delft University of Technology
Prof. dr. R. Saive	University of Twente
Prof. dr. ir. S. Stremke	Wageningen University & Research
Prof. dr. A.W. Weeber	Delft University of Technology
Prof. dr. ir. A.H.M. Smets	Delft University of Technology, reserved

Copyright © 2025 by Y. Zhou
No part of this material may be reproduced, stored in a retrieval system, nor transmitted in any form or by any means without the prior written permission of the copyright owner.

ISBN 978-94-6473-952-7

Printed by Ipskamp Printing

An electronic version of this dissertation is available at
http://repository.tudelft.nl/.

To all the remarkable souls I have encountered, those I love, and those who have enriched my life in ways big and small.

Contents

Summary ix

Samenvatting xi

Nomenclature 1

1 Introduction 5
- 1.1 The role of Photovoltaics (PVs) . . . 6
- 1.2 PV in the urban environments . . . 6
- 1.3 Aim and outline of this work . . . 8
- 1.4 Main contributions to the PV field . . . 9

2 Solar PV potential in urban environment 11
- 2.1 Introduction . . . 11
- 2.2 Methodology . . . 13
  - 2.2.1 Input data preparation . . . 13
  - 2.2.2 Reconstruction of 3D building models . . . 16
  - 2.2.3 Annual solar irradiation map on buildings . . . 19
  - 2.2.4 Annual DC yield map on buildings . . . 23
  - 2.2.5 Annual AC yield map on buildings . . . 32
  - 2.2.6 Roof segments classification . . . 32
- 2.3 Results and discussion . . . 33
  - 2.3.1 Computational speed . . . 33
  - 2.3.2 Solar PV potential maps on TU Delft campus . . . 35
- 2.4 Validation study . . . 40
- 2.5 Conclusions . . . 40

3 Social impact of urban PV deployment 43
- 3.1 Introduction . . . 43
- 3.2 Methodology . . . 45
  - 3.2.1 Input data preparation . . . 45
  - 3.2.2 Roof plane detection and extraction . . . 47
  - 3.2.3 Roof surface visibility assessment and optimization . . . 49
- 3.3 Results and Discussion . . . 60
  - 3.3.1 Roof detection and extraction . . . 60
  - 3.3.2 Roof binary visibility and VA maps . . . 60
  - 3.3.3 Roof module placement and AC yield map . . . 63
  - 3.3.4 Roof PV visibility map . . . 63
  - 3.3.5 Computation speed . . . 65
  - 3.3.6 Accuracy evaluation . . . 68

3.4 Conclusions . . . 69

4 Climate impact of urban PV deployment 71
4.1 Introduction . . . 71
4.2 Methodology . . . 73
4.2.1 Geometric Spectral Albedo (GSA) model . . . 74
4.2.2 Rooftop PV yield calculation . . . 83
4.2.3 Radiative forcing calculation . . . 83
4.2.4 MODIS albedo products . . . 84
4.3 Restuls and discussion . . . 84
4.3.1 Albedo results from the GSA model . . . 84
4.3.2 Annual roof PV energy from simplified skyline-based method . . . 90
4.3.3 Positive and negative radiative forcings . . . 90
4.4 Conclusions . . . 93

5 Multi-functional PV demonstrator 97
5.1 Introduction . . . 97
5.2 Experimental setup . . . 100
5.2.1 I-V curve measurement of PV laminates . . . 103
5.2.2 Bandwidth measurement of PV laminates . . . 104
5.3 Methodology . . . 107
5.3.1 Offset the ballast resistance in bias driver . . . 107
5.3.2 Include the inductance-induced resonance . . . 108
5.4 Results and discussion . . . 108
5.4.1 Bandwidth vs PV operating voltages . . . 109
5.4.2 Bandwidth vs irradiance levels . . . 111
5.4.3 Bandwidth vs LED colors . . . 112
5.4.4 Bandwidth vs architecture of commercial c-Si PV cells . . . 113
5.4.5 Trade-off between energy harvesting and communication . . . 118
5.5 Conclusions . . . 121
5.6 Appendix: Determination of damping ratio condition and inductance . . . 122

6 Conclusion and outlook 125
6.1 Conclusions . . . 125
6.2 Outlook . . . 127

References 133

Acknowledgement 151

List of publications 153

Curriculum Vitae 155

Summary

As a key pillar of the long-term decarbonization efforts, Photovoltaic (PV) is expected to grow significantly, driven by continuous technology development, cost reduction, and long-term climate action strategies targeting net-zero greenhouse gas (GHG) emissions by 2050. A major advantage of PV over other renewable energy sources is its ability to be integrated seamlessly into the urban environment without demanding additional land use. With the ongoing urbanization, the expansion of decentralized solar energy solutions will be essential in facilitating the transition to a green energy future. However, despite these incentives, designing, allocating, and maintaining urban PV systems present challenges.

This dissertation explores potential solutions to these challenges from various perspectives, aiming to improve understanding of the dynamics between PV systems and the urban environment. To achieve this, simulation models are developed and implemented to evaluate large-scale urban PV potential while incorporating social and climate concerns. Meanwhile, experimental approaches are taken to investigate the multifunctional capabilities of PVs that can be integrated into the future urban infrastructure.

Chapter 2 addresses urban PV deployment from a technical perspective. A comprehensive simulation workflow is established utilizing Light Detection and Ranging (LiDAR) data and building footprint inputs, enabling large-scale solar PV potential assessment in the urban environment. This framework delivers multiple outputs, including accurate geo-referenced 3D building models, annual solar irradiation maps, annual DC/AC yield maps, and roof classifications based on the specific yield of installed PV systems. These high-resolution 3D solar PV potential maps for building roofs and facades, along with potential PV system layouts, support the estimation of annual PV yield and the identification of the most viable building candidates for PV integration. Applying this simulation framework on the campus of Delft University of Technology (TU Delft) reports a total of 8.1 GWh/year PV potential from the building roofs and facades.

Chapter 3 studies urban PV deployment from a social perspective by designing a geographic information system (GIS) based large-scale visibility assessment tool to quantify the roof visibility for PV planning. This tool quantifies roof visibility through line-of-sight (LOS) assessments between roof surface points and hypothetical observers represented by points along road networks. The outputs offer not only binary visibility information of roof points (indicating whether roof points are visible or obscured) but also their visual amplitude (measuring the degree of visibility to the public domain). Moreover, the tool is able to suggest feasible PV system layouts, and the visibility of PV modules within the system is categorized into low, medium, and high categories, providing valuable insights into the multi-criteria decision-making process for urban PV planning. The simulation results for twelve monumental buildings on the TU Delft campus indicate annual PV potentials of 2.68, 0.42, and 0.37 GWh for PV modules categorized as low, medium, and high visibility, respectively.

Chapter 4 investigates urban PV deployment from a climate perspective by assessing its impact on the Earth's energy balance. A set of numerical and analytical frameworks is established to simulate urban albedo and quantify the radiative forcing (RF) effects associated with urban rooftop PV integration. These effects include 1) enhanced positive RF due to reduced albedo and 2) compensatory negative RF from the decreased CO_2 emission due to the replacement of fossil fuel with PV electricity. The albedo results are validated with the Moderate Resolution Imaging Spectroradiometer (MODIS [1]) satellite products, with 90% of investigated coordinates showing ±0.03 difference. The RF results reveal that the negative RF can offset the positive RF within around forty days under the current grid carbon emission intensity (437 g CO_2-eq/kWh) when PV is deployed across all rooftops in Delft. This finding provides a more comprehensive understanding of the role of urban PV in sustainable engineering and highlights its rapid climate mitigation potential.

Chapter 5 explores urban PV deployment from an application perspective by studying the dual functionality of laminated crystalline silicon (c-Si) PV cells in a visible light communication (VLC) system for simultaneous energy harvesting and data transmission. Seven different c-Si architectures are examined, with their bandwidth characterized across a voltage range from short-circuit to open-circuit under three light-emitting diode (LED) colors at three irradiance levels. The findings reveal a trade-off between energy harvesting and communication when PV cells are used as VLC receivers. LED color has minimal influence on the bandwidth across the entire operating voltage range. However, higher LED intensity enhances communication performance when PV laminates are working at lower operating voltages, while its impact is negligible at the maximum power point (MPP).

[1] MODIS albedo product is a daily 16-day data, which provides both black sky albedo and white sky albedo for 10 wavelength bands.

Samenvatting

Als een belangrijke pilaar van de langetermijnstrategie voor decarbonisatie, zal zonne-energie met fotovoltaïsche (PV) systemen naar verwachting sterk groeien, gedreven door voortdurende technologische ontwikkelingen, kostenreductie en klimaatstrategieën die mikken op netto-nul broeikasgasemissies (GHG) in 2050. Een groot voordeel van PV ten opzichte van andere hernieuwbare energiebronnen is de mogelijkheid om naadloos te worden geïntegreerd in de stedelijke omgeving, zonder extra landgebruik te vereisen. Met de voortgaande verstedelijking zal de uitbreiding van decentrale zonne-energie systemen essentieel zijn bij het faciliteren van de overgang naar een groene energietoekomst. Ondanks deze voordelen brengt het ontwerpen, toewijzen en beheren van stedelijke PV-systemen echter aanzienlijke uitdagingen met zich mee.

Dit proefschrift onderzoekt mogelijke oplossingen voor deze uitdagingen vanuit verschillende perspectieven, met als doel het inzicht te vergroten in de dynamiek tussen PV-systemen en de stedelijke omgeving. Hiervoor zijn simulatiemodellen ontwikkeld en toegepast om het grootschalige stedelijke PV-potentieel te evalueren, waarbij sociale en klimatologische aspecten zijn meegenomen. Daarnaast zijn experimentele benaderingen ingezet om de multifunctionele mogelijkheden van PV te onderzoeken in toekomstige stedelijke infrastructuren.

Hoofdstuk 2 behandelt stedelijke PV-implementatie vanuit een technisch perspectief. Een uitgebreid simulatiekader is ontwikkeld op basis van Light Detection and Ranging (LiDAR)-data en gebouwcontouren, waarmee het stedelijke PV-potentieel grootschalig kan worden ingeschat. Dit kader levert meerdere resultaten op, waaronder nauwkeurige geo-gerefereerde 3D-gebouwmodellen, jaarlijkse zoninstralingskaarten, jaarlijkse DC/AC-opbrengstkaarten en dakclassificaties op basis van de specifieke opbrengst van geïnstalleerde PV-systemen. Deze hoog-resolutie 3D-kaarten van het zonne-energiepotentieel voor daken en gevels van gebouwen, gecombineerd met mogelijke PV-systeemindelingen, ondersteunen zowel de schatting van de jaarlijkse PV-opbrengst als de identificatie van de meest kansrijke gebouwen. Toepassing van dit kader op de campus van de Technische Universiteit Delft (TU Delft) toont een totaal potentieel van 8.1 GWh/jaar aan PV-opbrengst op daken en gevels.

Hoofdstuk 3 onderzoekt stedelijke PV vanuit een sociaal perspectief door middel van een geografisch informatiesysteem (GIS) voor grootschalige zichtbaarheidsevaluatie. Dit instrument kwantificeert de zichtbaarheid van daken via lijn-van-zicht (LOS)-analyses tussen dakpunten en hypothetische waarnemers weergegeven door punten langs wegennetwerken. De resultaten omvatten niet alleen binaire zichtbaarheid (waarbij wordt aangegeven of dakpunten zichtbaar of verborgen zijn), maar ook de visuele amplitude (de mate van zichtbaarheid vanuit het publieke domein). Daarnaast genereert het instrument mogelijke PV-systeemindelingen, waarbij de zichtbaarheid van de modules wordt ingedeeld in laag, middel en hoog. Dit biedt waardevolle input voor multi-criteria besluitvorming rond PV-planning. Toepassing op twaalf monumentale gebouwen van

de TU Delft-campus toont jaarlijkse PV-opbrengsten van respectievelijk 2.68, 0.42 en 0.37 GWh voor modules met lage, middelhoge en hoge zichtbaarheid.

Hoofdstuk 4 bekijkt stedelijke PV vanuit een klimaatperspectief door de impact op de energiebalans van de aarde te analyseren. Een reeks numerieke en analytische kaders is ontwikkeld om stedelijke albedo te simuleren en de effecten van stralingsforcering (RF) door stedelijke PV-integratie te kwantificeren. Deze effecten omvatten 1) verhoogde positieve RF door verminderde albedo en 2) compenserende negatieve RF door lagere CO_2-emissies dankzij vervanging van fossiele brandstoffen door PV-elektriciteit. De albedoresultaten zijn gevalideerd met de Moderate Resolution Imaging Spectroradiometer (MODIS[1]) satellietproducten, waarbij 90% van de onderzochte coördinaten een verschil van ± 0.03 vertoonden. De resultaten tonen aan dat negatieve RF de positieve RF binnen circa veertig dagen kan compenseren bij de huidige emissie-intensiteit van het net (437 g CO_2-eq/kWh) wanneer alle daken in Delft worden bedekt met PV. Deze bevinding geeft een vollediger beeld van de rol van stedelijke PV in duurzame engineering en benadrukt het snelle klimaatmitigerende potentieel.

Hoofdstuk 5 onderzoekt stedelijke PV vanuit een toepassingsperspectief door de dubbele functionaliteit van gelamineerde kristallijn-silicium (c-Si) PV-cellen in een zichtbare-lichtcommunicatie (VLC) systeem te bestuderen, waarbij energieopwekking en datatransmissie gelijktijdig plaatsvinden. Zeven verschillende c-Si-architecturen zijn onderzocht, waarbij hun bandbreedte is gekarakteriseerd over een spanningsbereik van short circuit tot open circuit onder drie kleuren licht-emitterende diodes (LED) en drie irradiantieniveaus. De resultaten tonen een afweging tussen energieopwekking en communicatie wanneer PV-cellen als VLC-ontvangers worden ingezet. De LED-kleur heeft nauwelijks invloed op de bandbreedte, maar hogere lichtintensiteit verbetert de communicatieprestaties bij lage spanningen, terwijl dit effect verwaarloosbaar is bij het maximum power point (MPP).

[1] Het MODIS-albedoproduct is een dagelijkse 16-daagse dataset die zowel black-sky- als white-sky-albedo biedt voor 10 golflengtebanden.

Nomenclature

AHN	Actueel Hoogtebestand Nederland.
Al-BSF	Aluminum back surface field.
ASTER	Advanced Spaceborne Thermal Emission Reflection Radiometer.
BAG	Basisregistratie Adressen en Gebouwen.
BIPV	Building integrated PV.
BOS	Balance of system.
BRDF	Bidirectional reflectance distribution function.
c-Si	Crystalline silicon.
CC	Constant current.
DHI	Diffuse horizontal irradiance.
DNI	Direct normal irradiance.
DSM	Digital surface model.
EEMCS	Electrical Engineering, Mathematics, and Computer Science.
EnCE	Energy-communication efficiency.
ESP	Electrical sustainable power.
ET	Equilibrium time.
GaAs	Gallium arsenide.
GHG	Greenhouse gases.
GHI	Global horizontal irradiance.
GIS	Geographic information system.
GPS	Global positioning system.
GSA	Geometric spectral albedo.

IBC Interdigitated back contact.

IoT Internet of things.

LCoE Levelized Cost of Electricity.

LED Light-emitting diode.

LiDAR Light detection and ranging.

LiFi Light fidelity.

LoD Level of details.

LOS Line-of-sight.

MIMO Multi-input multi-output.

MODIS Moderate resolution imaging spectroradiometer.

MPP Maximum power point.

nB Normalized bandwidth.

nPD Normalized power density.

nVA Normalized visual amplitutde.

NZE Net Zero Emissions.

OFDM Orthogonal frequency division multiplexing.

OOK On-off keying.

OPV Organic PV.

OWC Optical wireless communication.

PDs Photodiodes.

PERC Passivated emitter and rear contact.

POA Plane-of-array.

ppm Parts per million.

PV Photovoltaic.

RF Radiative forcing.

RFreq Radio frequency.

RMS	Root mean square.
SCF	Sun coverage factor.
SD	Standard deviation.
SHJ	Silicon heterojunction.
SMARTS	Simple Model of the Atmospheric Radiative Transfer of Sunshine.
SNL	Sandia National Laboratories.
STC	Standard test conditions.
SVF	Sky view factor.
TMY	Typical Meteorological Year.
TOA	Top-of-the-atmosphere.
TOPCon	Tunnel oxide passivated contact.
UHI	Urban heat islands.
VA	Visual amplitutde.
VLC	Visible light communication.
WDM	Wavelength division multiplexing.
WiFi	Wireless fidelity.

1

Introduction

The Industrial Revolution marked the dawn of modern society, fundamentally transforming how people live and work through large-scale mechanization. This shift dramatically increased production and transportation efficiency, enhancing overall comfort and convenience. However, this groundbreaking transformation has required burning fossil fuels, releasing enormous amounts of heat-trapping greenhouse gases (GHG), particularly CO_2, into the atmosphere, driving global warming.

Over millions of years, atmospheric CO_2 levels remained below 300 parts per million (ppm), but this number started rocketing since the Industrial Revolution [1]. Between 2002 and 2022 alone, CO_2 levels jumped from 365 ppm to 420 ppm, as shown in Figure 1.1, which warms up the globe by approximately 1.47 °C in 2024 than the pre-industrial average [2]. This rise in temperature poses severe consequences for lives on Earth, affecting natural ecosystems, climate cycles, public health, economic stability, and other critical aspects [3]. Therefore, urgent actions need to be taken to combat the climate crisis and mitigate further escalation.

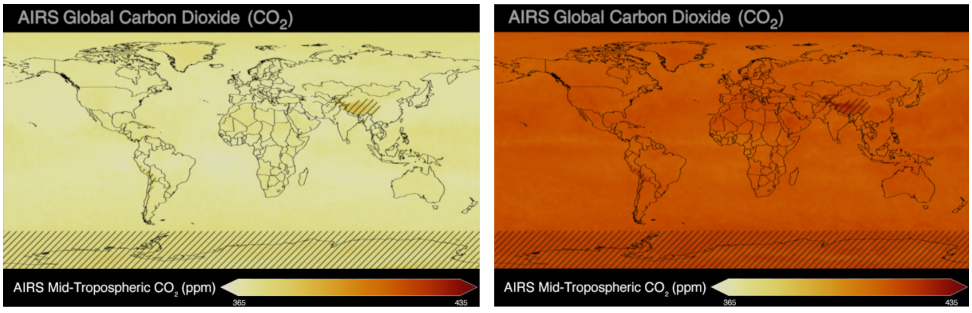

September 2002 September 2022

Figure 1.1: The change in atmospheric CO_2 concentration over two decades from 2002 to 2022 [1].

1

1.1. The role of Photovoltaics (PVs)

In 2015, the Paris Agreement was adopted to limit global warming to well below 2 °C, preferably to 1.5 °C, above pre-industrial levels [4, 5]. This is certainly an ambitious target, and achieving this goal requires slashing GHG emissions by replacing fossil fuels with renewable energy sources.

As of 2023, renewable energy sources accounted for 13% of the world's total energy supply, with projections indicating an increase to 20% by 2030 [6]. Particularly in the electricity sector, renewable energy sources are expected to provide 60% of electricity generation in 2030 under the Net Zero Emissions (NZE) Scenario [7]. Among these sources, solar energy is a key pillar in the long-term decarbonization efforts. Although PV currently contributes a relatively small share of global electricity generation (5.5% as of 2023), significant growth is anticipated due to continuous technology development and cost reduction [8]. As shown in Figure 1.2, a recent study predicts an annual PV growth rate of 25%, and the worldwide installed PV capacity could reach up to 75 TW by 2050 [9]. To realize such a boost in PV penetration in the energy system, developments are required not only in large-scale solar farms but also in the widespread deployment of PV systems in urban settings, especially considering the ongoing progress of urbanization with population influx [10].

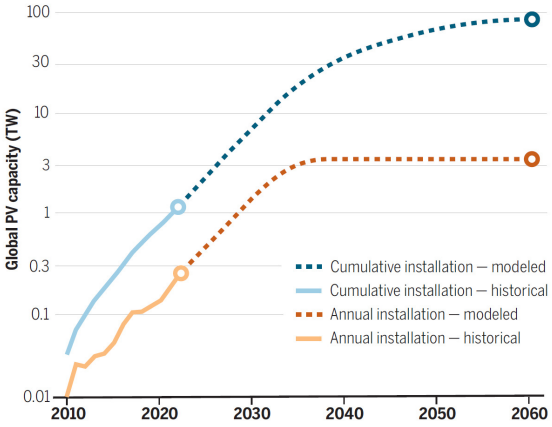

Figure 1.2: Modelled annual and cumulative installation of PV, which maintains 25% growth rate until 2030, then reduces slowly to steady state [9].

1.2. PV in the urban environments

The current electrical energy distribution system predominantly features centralized generation and a mono-directional distribution network. This system relies on large power plants producing electricity and long-distance grid networks transporting the electricity to consumers. However, achieving a sustainable future cannot be simply accomplished by replacing conventional power plants with large-scale renewable energy farms. One potential limitation of this centralized approach is reduced reliability because a failure at the central power plant can impact the broader grid [11]. Considering the intermittent

nature of renewable energies, optimizing the reliability of the energy system will be even more challenging. Another significant issue is the energy loss during the long-distance transmission and distribution of electricity. In addition, as the electrification of end-uses accelerates, the finite grid capacity can also become the bottleneck. As an alternative, decentralized renewable energy sources offer the ability to produce electricity locally, spreading the responsibility of electricity generation across numerous smaller producers. This configuration reduces power loss by placing generations close to consumers, enhancing energy independence, and relieve the electricity imports from the grid when the generation coincides with the demand. Meanwhile, considering that most of the world's population (68% by 2050) will be living in cities in the future, the development of decentralized renewable energy solutions in urban environments will play a significant role in facilitating the transition to green energy [12, 13].

PV systems emerge as the most viable option to meet this goal due to their adaptability in urban settings. Unlike other renewable technologies, they offer great advantages for urban integration, including ease of local implementation and efficient use of existing surfaces [14, 15]. PV can be seamlessly integrated onto a variety of urban structures, such as buildings, roads, and waterways, all without requiring additional land [16–19]. This high integrability has already driven the growing adoption of PV in urban environment, and considerable growth potential still remains. For example, building envelopes in Germany can offer a technical potential of around 1000 GW_p, of which less than 10% has been utilized [20, 21].

Although PV technology is highly compatible with urban environments, designing, allocating and maintaining these systems within such contexts presents challenges:

- From a technical perspective, densely constructed cities often limit the incoming sunlight, while rich urban morphology – including buildings, infrastructures, and vegetation – can cause complex shading patterns. As a result, not all urban surfaces are suitable for PV installation, and designing urban PV systems is more challenging than simply optimizing tilt and orientation for a given location. Installing PV modules in areas with low irradiation or frequent shading reduces their specific yield, undermining the system's economic viability.

- From a social perspective, PV generally has relatively high public acceptance [22]. Nevertheless, urban PV installations are subject to more strict social regulations, requiring designs that preserve the visual integrity of the urban landscape. This is especially crucial for historical buildings and cultural heritages, where PV modules must be aesthetically integrated or remain invisible to the public [23]. These constraints further limit the deployment of urban PV systems.

- From a climate perspective, the expansion of urban PV systems can give rise to adverse effects [24]. The substitution of original urban surfaces with highly absorptive PV modules usually reduces the urban albedo. Locally, this reduced albedo contributes to the formation of urban heat islands (UHI), degrading the thermal comfort of urban dwellers, adversely affecting their health and potentially reducing life expectancy [25]. Globally, it increases the energy absorbed by Earth, enhancing the warming effect [26, 27].

- From an application perspective, the growing accessibility with the widespread deployment of PV modules presents the opportunity to explore its multi-functional potential. Beyond serving as passive energy harvesters, PV systems can also fulfill additional design purposes, such as enhancing aesthetics [28], incorporating thermal management [29], and improving shading tolerance [30]. To further maximize the benefits of urban PV integration, exploring their potential for information communication is also a promising application. The photons absorbed by the PV modules not only generate electricity but can also be modulated to transmit data. In this way, PV technology evolves from a purely energy-generating system to an active, multifunctional component of urban infrastructure [31].

Solving these challenges helps understanding the dynamics between PV systems and the urban environment, facilitating the streamlining of large-scale urban PV deployment.

1.3. Aim and outline of this work

The objective of this work is to evaluate the large-scale urban PV potential while incorporating social and climate concerns. Additionally, it investigates the multi-functional capabilities of PV systems that can be integrated into the urban infrastructure.

The first part of this work focuses on developing a simulation framework to assess the PV potential in complex urban settings. The second part extends the analysis by addressing social and climate factors related to urban PV deployment. Finally, the third part of this research explores the potential of using c-Si solar cells as data receivers. The methodology employed for each study is described in detail within the corresponding chapter. The structure of the dissertation can be broken down into the following chapters:

Chapter 1, being the current chapter, highlights the significance of urban PV deployment and the challenges it faces. It also outlines the contributions of this work in potentially solving these challenges.

Chapter 2 addresses first the technical aspects of urban PV deployment, and a comprehensive simulation workflow is presented for high-resolution 3D solar PV potential mapping on building roofs and facades. This framework estimates the PV yield within the urban environment and identifies the most favorable roof surfaces for PV integration.

Based on the developed simulation workflow, Chapter 3 dives into the social challenge of urban PV integration. Particularly, a framework is established for assessing the PV module's visibility from the public domain at the street level, which helps facilitating the streamlined integration of PV on restricted buildings such as monuments and cultural heritages.

Chapter 4 is dedicated to studying the impact of urban PV integration on albedo and its implications for Earth's energy balance. It presents two simulation stages: the first one computes the change of albedo due to urban PV deployment and the resulting additional solar energy absorbed by the Earth, and the second one calculates the CO_2 emission reduction due to the displacement of fossil fuels with PV and estimates the time required to offset the initial albedo-related warming.

In Chapter 5, the potential of using solar cells to receive data is explored. Specifically,

it analyses the bandwidth characteristics of c-Si PV cells, from the first to the latest generation, under different current-voltage operating points, LED colors, and light intensities.

Finally, the conclusions are drawn in Chapter 6, where future research recommendations are presented.

1.4. Main contributions to the PV field

The main highlights of this research are listed below:

- A comprehensive workflow for solar PV assessment in dense urban environments, generating multiple geo-referenced outputs including 3D building models, annual solar irradiation map, annual DC yield map, annual AC yield map, roof PV system layout, and roof classification based on the PV system's specific yield.
- A line-of-sight (LOS) assessment method for quantifying the visibility of roof surfaces from the public street level, categorizing them into low, medium, and high visibility categories and computing their corresponding PV potential.
- An in-depth analysis of the dual consequences of urban PV integration for the Earth's energy balance, offering insights into the urban albedo modification and its implications for radiative forcing dynamics.
- A systematic study of using c-Si PV cells for simultaneous energy harvesting and information receiving in visible light communication.

2

Solar PV potential in urban environment

This chapter is based on the following publication:

Y. Zhou, M. Verkou, M. Zeman, H. Ziar, and O. Isabella, *A Comprehensive Workflow for High Resolution 3D Solar Photovoltaic (PV) Potential Mapping in Dense Urban Environment: A Case Study on Campus of Delft University of Technology*, Solar RRL **6**, 2100478 (2021). (DOI: https://doi.org/10.1002/solr.202100478)

2.1. Introduction

Following the directive of the Paris Agreement, the Dutch government launched the National Climate Agreement in 2019, and an ambitious goal was set to reduce GHG emissions by 49% by 2030, relative to 1990 levels [32]. Additionally, it also projects that 70% of the electricity will be sourced from renewable energy by 2030, with a target to achieve nearly complete GHG reduction by 2050. To realize these objectives, a boost of green energy penetration in the domestic energy system is essential.

In alignment with these goals, TU Delft aims to achieve a climate-neutral campus by 2030 [33]. Among various renewable energy technologies, PV systems emerge as the most viable option due to their adaptability in urban settings. According to the latest available report, only 1.2 MW_p of solar capacity is installed on campus buildings, and a significant expansion of PV deployment is needed to minimize the campus's carbon footprint [34, 35]. Designing PV systems in complex urban settings can be challenging, and to facilitate the road mapping of renovating existing campus buildings with PV technology, it is crucial to understand the urban context so that available building surfaces can be identified and their PV potential can be assessed [36, 37]. One innovative method involves using aerial imagery combined with image recognition to identify the geometry of suitable roof surfaces for PV integration [38–40]. Among others, orthographic aerial images provide a direct view of building areas, and the height of buildings is generally

estimated by fitting a normal distribution function. In contrast, aerial stereo images allow the generation of the digital surface model (DSM) through stereophotogrammetry, using overlapping images from different angles [41]. Another approach is based on light detection and ranging (LiDAR), which is currently the most widely used spatial data to represent and reconstruct the urban environment [42]. This remote sensing technology densely samples earth surfaces by transmitting laser pulses and analyzing the reflected signals [43].

Generally, the assessment of renewable energy potential, specifically solar energy, can be structured hierarchically: i) physical potential that represents the total amount of solar irradiation impinging on the study area; ii) geographical potential that considers only the solar irradiation on surfaces that are available for PV integration; iii) technical potential considering the efficiency of specific PV technologies and the balance of system (BOS) components; and iv) economic potential which assesses the financial viability of the PV system installation [44]. Over the past few decades, extensive research has focused on estimating urban solar energy potential, each tailored to different hierarchical levels depending on project goals and data availability [45–49]. Jaroslav et al. assessed the PV potential in a small city in eastern Slovakia by using open-source tools, beginning with the creation of a 3D city model and utilizing the $r.sun$ solar radiation model and PVGIS to calculate the roof's technical potential [50]. T. Santos et al. proposed a two-stage process that also models population distribution at the building level [51]. However, both studies primarily examined building roofs and did not consider shading from trees, infrastructure, or other artifacts. C. Catita et al. extended the solar potential analysis to vertical building facades using hyperpoints, which involve a set of points with the same XY coordinates but varying Z values [52]. This approach facilitated 3D mapping of solar potential on building surfaces, but more in-depth results, such as geographical or technical potential, were not delivered. Similar work has been done by M. C. Brito et al. on the city of Lisbon and A. Vulkan et al. on a neighborhood in Rishon LeZion in Israel [53]. Both works based their analysis on a relatively low spatial resolution (1 by 1 m^2), and only the physical potential on building surfaces is calculated. Particularly in the work from A. Vulkan, small-scale artifacts are excluded, and the solar irradiation calculation only considers the direct component. A .V .Vo et al. reported a comprehensive workflow for estimating urban solar potential by processing each LiDAR point, but it demands a high-resolution LiDAR dataset (300 points/m^2) and is computationally intensive [54]. Another detailed model, PLANTING, developed by S. M. Murshed et al., calculates the economic potential of solar installations on both roofs and facades but requires hourly analysis and access to semantically and topologically accurate CityGML data, which are challenging to prepare [55]. N. Alam et al. conducted a detailed analysis of different resolution settings in PV potential calculation, including temporal resolution, 3D city model resolution, and sky dome subdivision. It was demonstrated that higher resolution generally improves accuracy while at the cost of increased computational time [56].

In this work, we developed a large-scale urban PV modeling workflow up to the AC level that utilizes a minimum set of freely available input datasets. This workflow is semi-automatic and requires only LiDAR data and building footprints as inputs, which is a unique approach compared to other studies that typically demand additional data, including aerial images or expensive 3D building models [57, 58]. Meanwhile, the work-

flow is capable of delivering PV AC yield for both building roofs and facades, providing decision-makers with broader insights into urban solar planning. Notably, this method enhances existing models by investigating i) portrait and dual-tilt mounting configurations on flat roofs, ii) partial shading losses induced by mutual shading, iii) skyline variation for each module, and iv) dynamic inverter efficiency based on Sandia National Laboratories (SNL) model. Furthermore, instead of calculating hourly irradiance on the plane-of-array (POA) and aggregating these over the year to estimate annual solar irradiation, which requires significant computational resources, this work employs an in-house developed simplified skyline-based model to map solar PV potential efficiently [59]. This model accurately estimates annual solar PV potential on various surfaces while significantly reducing computational demands. The complete workflow is shown in the Figure 2.1.

2.2. Methodology

2.2.1. Input data preparation

Airborne LiDAR data offers precise topographical information, which details the physical representation of natural and artificial surface features. During collection, LiDAR equipment, typically mounted on aircraft, emits laser light toward the ground. This light reflects off surfaces and is captured by the sensor, which records the time taken for the light to travel to and from the objects. Analyzing this travel time allows for the calculation of distances, which are combined with the Global Positioning System (GPS) to generate elevation data with geographical coordinates [60]. The resulting dataset is presented as a geo-referenced point cloud, meaning each point is assigned 3D geographic coordinates that allow it to be accurately located in space. LiDAR technology can identify basic objects on the ground, such as vegetation, buildings, etc. As laser light traverses trees, for instance, the photons may be partially reflected off branches or leaves since they are small in size and full of gaps. The remaining photons continue their journey until they encounter a solid surface. Thus, multiple returns can be captured and recorded by the sensor from one pulse of light to create a waveform. Different objects can be identified by analyzing these waveforms.

The Dutch government initiated its first batch of LiDAR data collection in 1997. The dataset is called Actueel Hoogtebestand Nederl (AHN), and the latest accessible version (AHN5) is currently under collection. For the purposes of this research, the AHN3 LiDAR dataset was utilized, as it represented the most current available batch during the research period. Generally, the time span of LiDAR acquisition stretches over a few years. The AHN3 data was collected between 2014 and 2019 and has a resolution of around 6 to 10 points per square meter [61]. Figure 2.2 displays the AHN3 LiDAR data of part of the TU Delft campus, in which the elevation of the points, from low to high, is indicated by the color from grey to yellow.

The management and process of LiDAR data are facilitated by the GIS [62]. The raw LiDAR data, often voluminous and complex, can pose significant challenges for direct analysis. To enhance manageability and for the ease of application, this data is typically transformed into a raster-based DSM. This conversion is efficiently carried out using the built-in geoprocessing tools available in ArcGIS Pro, which streamline the handling of

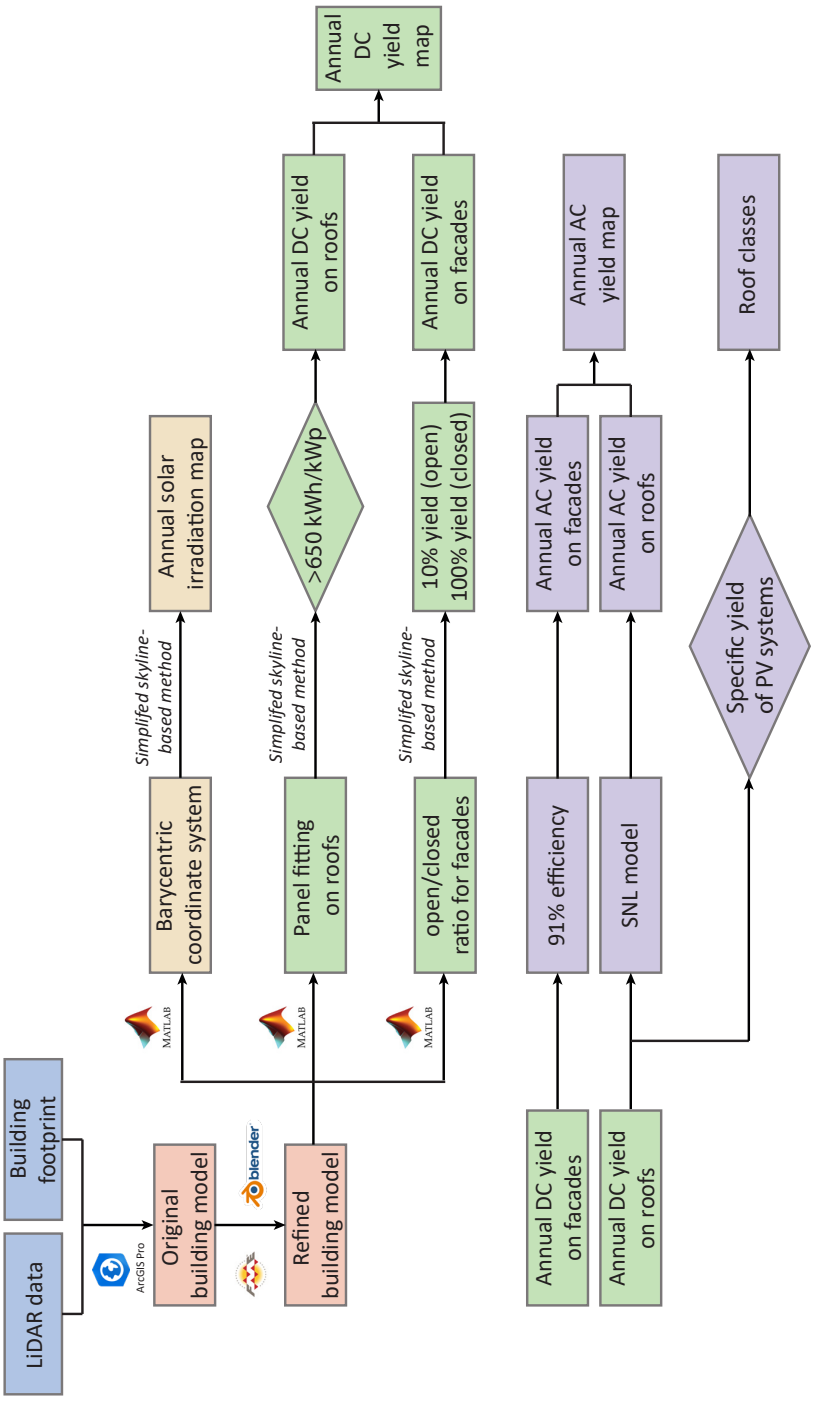

Figure 2.1: The workflow showcases the developed methodology, where the input data are depicted by the blue blocks. The simulation steps are represented in different colors where: red for 3D building model reconstruction, yellow for annual solar irradiation map generation, green for annual DC yield map generation, and purple for both annual AC yield map generation and roof classification. LiDAR and SNL are light detecting and ranging and Sandia National Laboratory, respectively.

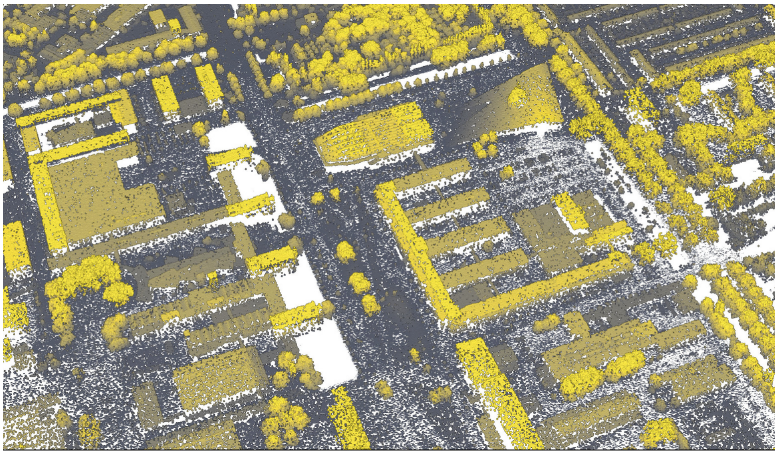

Figure 2.2: The AHN3 LiDAR data of part of the TU Delft campus, in which the elevation of the points, from low to high, is indicated by the color from grey to yellow.

large datasets by simplifying the rich point clouds into a more accessible format [63]. The DSM serves as the input to the projects carried out during the research period, and it is essentially a grid that consists of equally sized cells, with each cell assigned a single height representing the height of that complete cell.

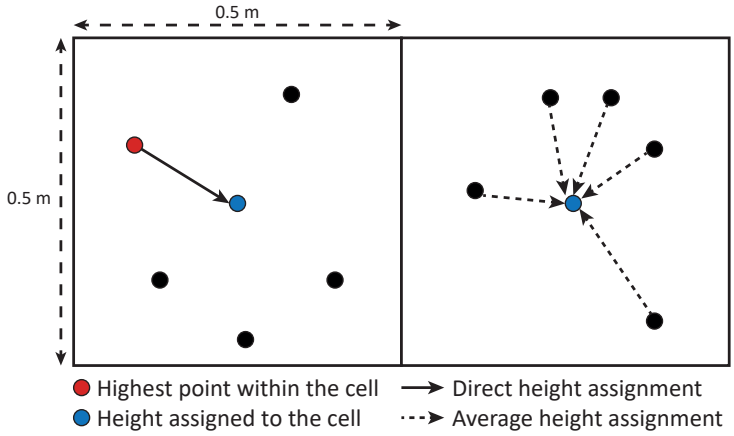

Figure 2.3: This illustration shows the conversion of two cells into a raster format from raw LiDAR data. The blue point indicates the height value assigned to each cell, which is determined by either taking the average height of all points within the cell or by adopting the height of the highest point (represented by the red point).

Depending on the intended use, the height value assigned to each cell can represent various aspects. Commonly, it may adopt the average height of all LiDAR points captured within that cell, providing a general representation of the terrain. Alternatively, it can reflect the maximum or minimum height recorded within the cell, which is useful

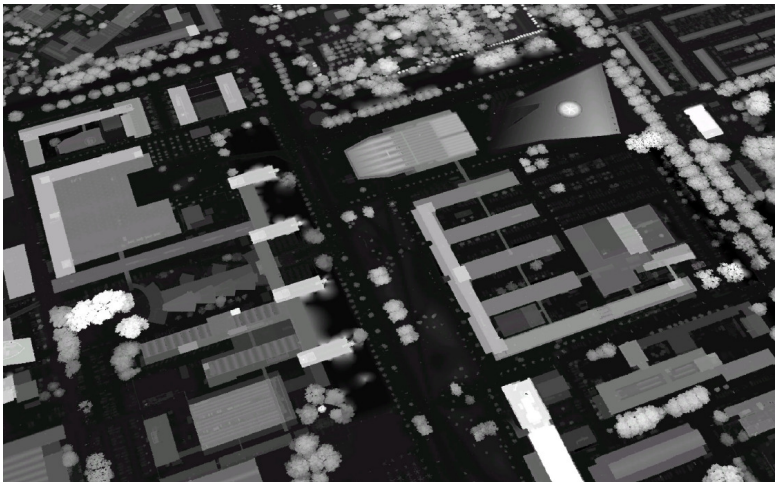

Figure 2.4: DSM of part of the TU Delft campus, in which each pixel represents one single height value. The elevation, from low to high, is indicated by the color transitioning from black to white.

for terrains with abrupt height variance. For example, in applications involving natural terrain mapping, averaging the heights of all points in a cell is preferred, ensuring a continuous representation of the overall landscape. Conversely, in urban settings where a cell might encompass the building and its surrounding environment, using the average height could lead to distortion of the representation of building shapes. In such scenarios, using the maximum height of the points within the cell provides a more precise representation of the urban features. Given the resolution of the AHN3 dataset, the cell size (also referred to as pixel size) can be minimally chosen as 0.5 meters, meaning that each cell covers an area of 0.25 m^2. Figure 2.3 illustrates this process, where raw LiDAR data from two cells are converted into raster formats. In the approach shown on the left, the highest point within the cell is identified, and its height is assigned to the cell center to represent its height. Conversely, the approach on the right calculates the average height of all points within the cell, assigning the mean value to the cell center to represent the cell's height. The resulting DSM of the same TU Delft campus section is shown in Figure 2.4, where the elevation (from low to high) representing each pixel is indicated by the color transitioning from black to white.

2.2.2. Reconstruction of 3D building models

The reconstruction of 3D building models leverages two key datasets: building footprints and LiDAR data, both of which are provided freely by the Dutch government [64]. The building footprint represents the outermost boundaries of a building's exterior walls, defining the planimetric layout of the structure. To illustrate the practical application of this workflow, the Electrical Engineering, Mathematics, and Computer Science (EEMCS) faculty building is used as a case study whose building footprint and corresponding LiDAR data are shown in Figure 2.5.

Initially, the original building models are generated in ArcGIS Pro with the LAS Build-

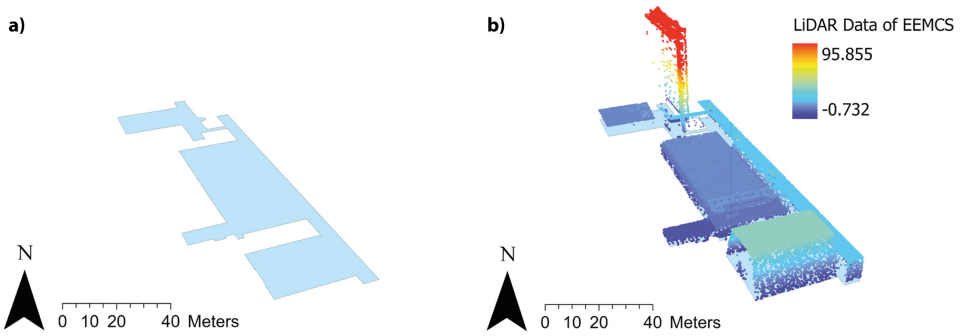

Figure 2.5: a) Building footprint of the EEMCS faculty building; b) LiDAR data of the EEMCS faculty building, with the height (in meters) indicated by a color bar.

ing Multipatch tool [65]. This model reconstructs the building models by creating a network of triangular meshes that connect all the adjacent LiDAR points within the building footprint. Figure 2.6 illustrates the original 3D building model of EEMCS faculty, which consists of numerous triangular meshes covering the entire building surface. However, due to the irregularity of the original LiDAR data, adjacent triangular meshes within a roof segment may not align properly, leading to significant discrepancies in slope and orientation. This misalignment ultimately compromises the accuracy of solar PV potential simulation results. Therefore, it is essential to refine the geometry to ensure that precise models are available for subsequent analysis.

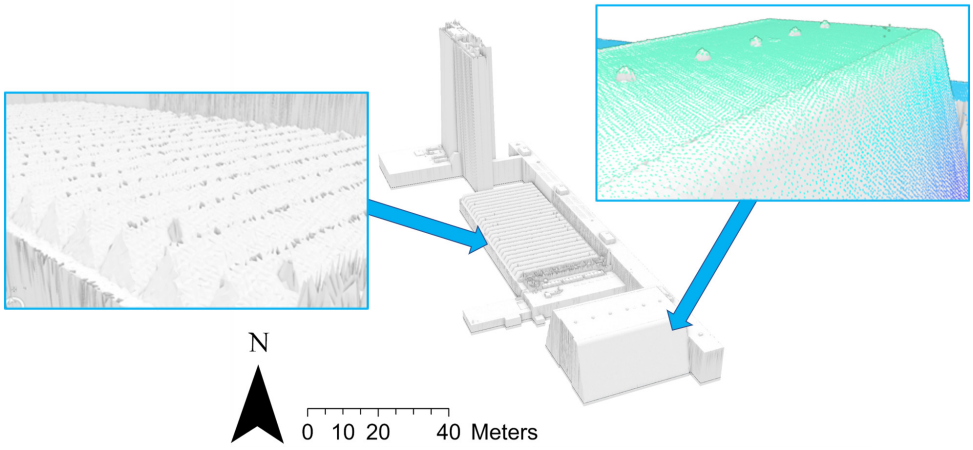

Figure 2.6: The original 3D model of the EEMCS faculty building. The building surfaces consist of triangular meshes that are generated from LiDAR points.

To achieve this, a free 3D creation suite, Blender, is used. Its built-in mesh simplification tool enables users to eliminate unnecessary vertices or meshes while maintaining minimal alterations to the overall model shape [66]. After applying this tool over multiple

iterations, the number of vertices and meshes is reduced to 1% of the original building model. Figure 2.7 presents a comparison of the EEMCS faculty building model before and after mesh simplification, clearly showing a dramatic decrease in the number of meshes while the shape of the building remains largely intact.

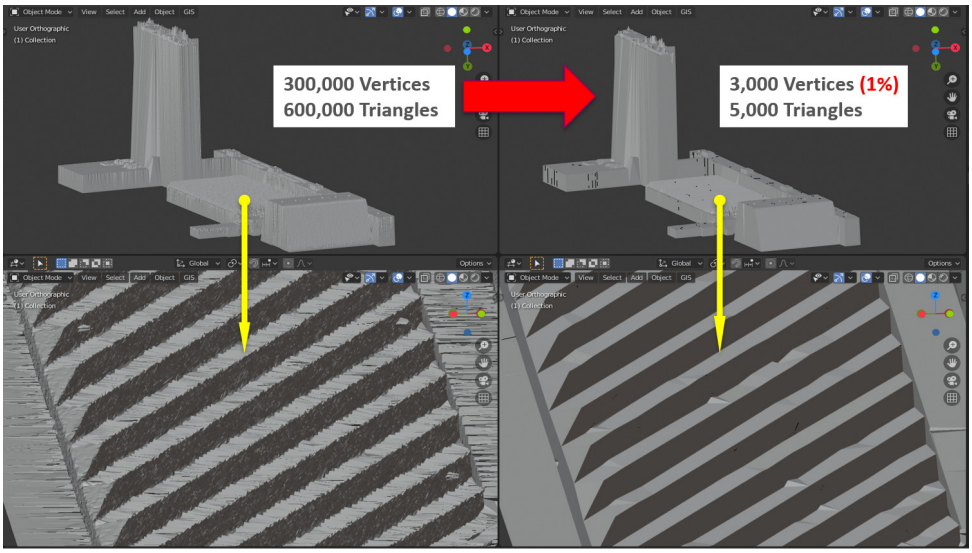

Figure 2.7: The Building model of EEMCS faculty before and after mesh simplification. The number of vertices and triangles is reduced to 1% by using the built-in tool in Blender while the shape of the building remains largely intact.

The final building model is achieved through manual adjustments to eliminate outliers and align edges effectively. Figure 2.8 displays the refined EEMCS building model. Upon closer inspection of various model sections, it becomes evident that only essential roof and facade polygons remain. Notably, building features such as ventilation systems, antennas, and chimneys have been excluded, as they do not contribute to the usable area for PV installation. The time required for our semi-automatic method to reconstruct geo-referenced building models varies based on the building's complexity, typically ranging from several minutes to a few hours. This significantly reduces the time needed for manual reconstruction with software like SketchUp, which often necessitates detailed building floor plans and several days to complete a single model [67]. In contrast to other recreation methods, such as drone-based photogrammetry, our approach does not require travel or specialized drone operation skills [68]. Nonetheless, it still produces highly accurate geo-referenced building models, relying solely on LiDAR data and building footprints.

One of the primary limitations of this methodology is the inadequate modeling of building facade details, as illustrated in Figure 2.9. The aperture at the top of the high-rise building is absent from the model, and the open space at the base of the low-rise building is also not accurately represented. This limitation arises primarily from the lack of digital facade information, as the locations of windows, ledges, and gaps are generally

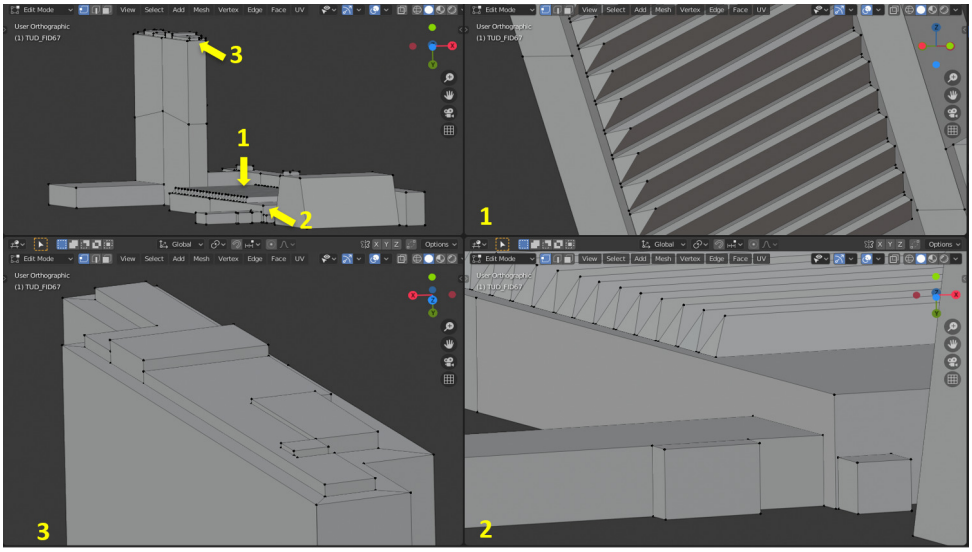

Figure 2.8: The final refined 3D model of EEMCS faculty building, which only includes essential roof and facade polygons.

not captured by LiDAR data. Consequently, only sharply defined closed facades are reconstructed by connecting the roof edges to the building footprint. Another limitation of this methodology is the workload involved in reconstructing buildings, as it relies on a semi-automatic approach. An alternative is to use the 3D BAG dataset, which provides the 3D building models to the level of detail (LoD) 2.2 for the entire Netherlands based on LiDAR data and building footprints [69]. Although these building models offer decent roof geometries, the noises that the building model contains (such as redundant vertices and faces) often complicate the subsequent solar PV potential simulations. Figure 2.10 illustrates this difference for the EEMCS faculty building: the refined semi-automatic reconstruction in Figure 2.10a is free from the noises circled out in Figure 2.10b, where these noises can confuse the developed MATLAB algorithm to accurately merge the triangular faces into coherent roof surface for further solar PV computation.

2.2.3. Annual solar irradiation map on buildings

The first step in mapping annual solar irradiation on buildings involves creating a uniformly distributed grid on the building surface. Each point on this grid represents a specific surface area, allowing for the calculation of incident solar irradiation using the simplified skyline-based method. The surface grid is generated using a barycentric coordinate system, which enables the location of any point within a triangle to be expressed using the following formula [70]:

$$P = \alpha \cdot A + \beta \cdot B + \gamma \cdot C \tag{2.1}$$

where P represents the coordinates of the point of interest, while A, B, and C denote the

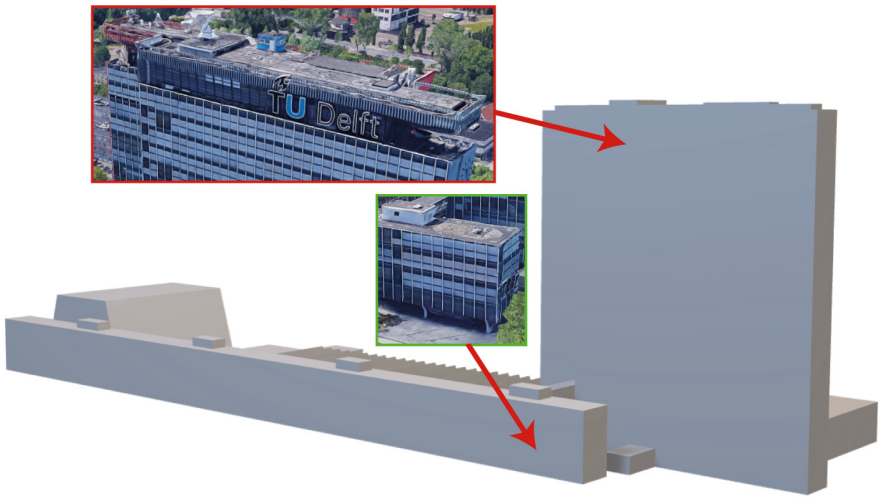

Figure 2.9: Limitation of the 3D building model reconstruction. The building facade cannot be properly recreated due to the lack of facade information. The aerial photo is obtained from GoogleMap (Imagery © 2021 Google, Imagery © 2021 Aerodata International Surveys, Maxar Technologies, Map data © 2021).

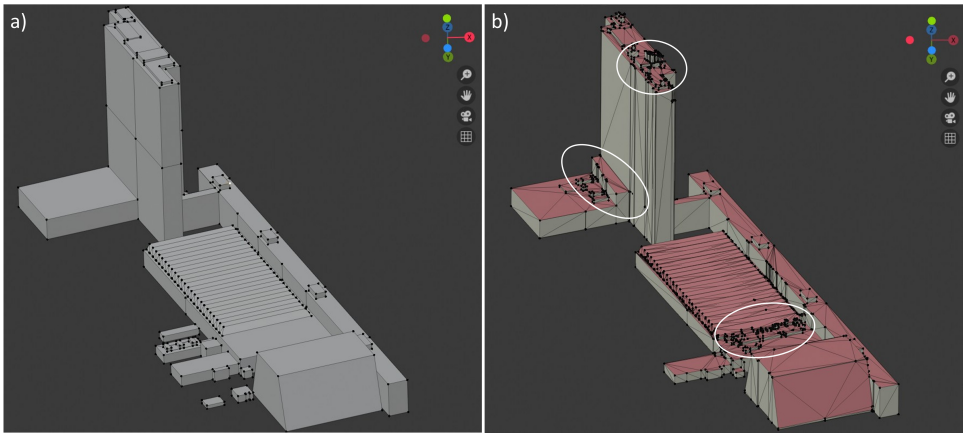

Figure 2.10: Comparison between the EEMCS faculty building model: a) refined model using semi-automatic approach, b) retrieved model from 3D BAG database. The noises in model b (e.g., redundant vertices and faces) complicate the subsequent solar PV potential simulations.

coordinates of the triangle's vertices. To ensure that the point of interest lies within the triangle, the following constraints must be satisfied:

$$\begin{cases} \alpha, \beta, \gamma \in [0,1] \\ \alpha + \beta + \gamma = 1 \end{cases} \tag{2.2}$$

Figure 2.11 demonstrates the application of the barycentric coordinate system to obtain the location of point P. In this illustration, point P divides the original triangle into three sub-triangles. The coefficients α, β, and γ are then calculated by determining the ratio of the area of each sub-triangle to the area of the original triangle. For instance, the coefficient α is computed by dividing the area of the blue sub-triangle by that of the original triangle, and a similar process is repeated for the coefficients β and γ. Adjusting the area ratios of triangles enables the mapping of an evenly distributed grid onto building surfaces. For this study, a grid size of 0.5 meters was chosen. Figure 2.12 illustrates the result of applying the barycentric coordinate system to one of the facades of the EEMCS faculty building. The zoomed-in image clearly shows that the points are uniformly distributed across the facade surface, maintaining a consistent gap of 0.5 meters.

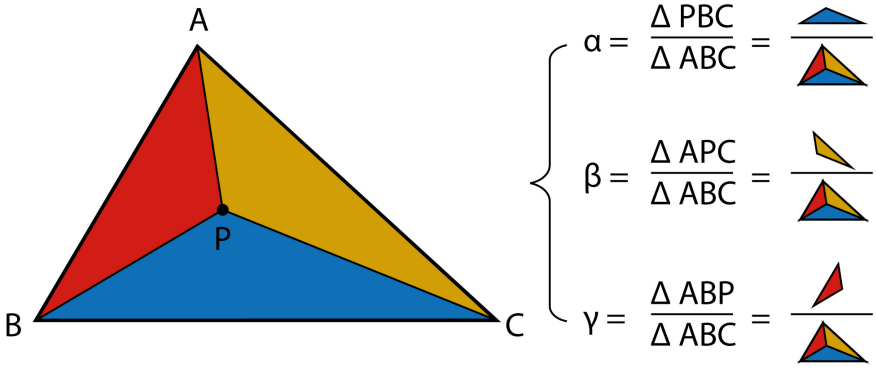

Figure 2.11: Using barycentric coordinate system to decide the location of the points. In this illustration, point P is the point of interest and subdivides the original triangle into three small triangles.

The annual solar irradiation for each point is determined using a simplified skyline-based model, which fits a polynomial function with a set of synthetic skylines [59]. This function is characterized by five coefficients and two primary parameters: Sky View Factor (SVF) and Sun Coverage Factor (SCF). The SVF quantifies how much of the sky hemisphere is freely visible, while the SCF indicates whether the horizon blocks the sun. These five coefficients, unique for every tilt and orientation within a given climate, were calculated for the local climate in Delft, the Netherlands, for each 45° azimuth and 5° tilt angle, with intermediate values derived through linear interpolation. Implementing this method requires information about roof property (tilt and azimuth) and the SVF and SCF derived from the skyline profile. The building surface's tilt and azimuth angles are inferred from the face normal vector, as depicted in Figure 2.13. Specifically, roof tilt θ_R is calculated as the angle between the face normal n_R and the ground normal [0,0,1], while

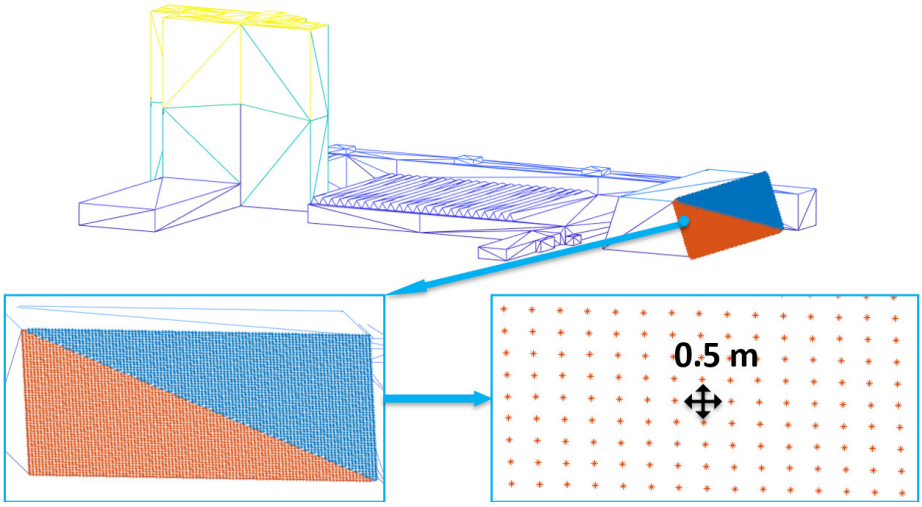

Figure 2.12: Applying the barycentric coordinate system to one of the facades of the EEMCS faculty building. The zoomed-in image clearly shows that the points are uniformly distributed across the facade surface, maintaining a consistent gap of 0.5 meters.

the roof azimuth A_R is derived from the angle between the due North vector [0,1,0] and the projection of the face normal onto the ground plane. To determine the SVF and SCF, an in-house developed MATLAB script is utilized to generate the skyline profile from the DSM [71]. This script constructs the skyline for any specified tilt and azimuth angle by first segmenting the full azimuth range into slices, and then assessing the height points within these segments. The highest point within each azimuth slice defines the horizon altitude for that segment. Combining the skyline profile with the sky hemisphere allows for determining the SVF and SCF.

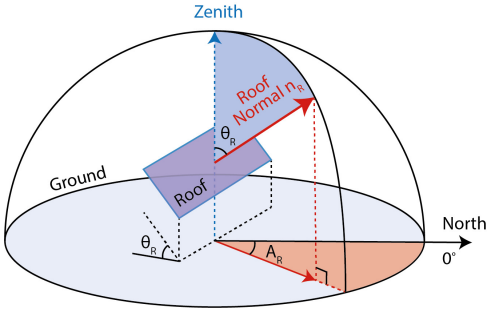

Figure 2.13: Determination of roof tilt θ_R and azimuth A_R from roof surface normal n_R.

Figure 2.14 presents a bird's eye view of the solar irradiation map of the EEMCS faculty building. Although rooftop artifacts were excluded during the building model reconstruction phase, their shading effects are still considered in the solar potential assessment based on the DSM-extracted skyline profile. These obstacles reduce the sun-

light reaching roof sections, resulting in areas depicted in dark red on the irradiation map. By comparing this map with the GoogleMap aerial photo, one can easily identify the types of obstacles present. For instance, the high-rise building's rooftop is shaded by antennas, while the low-rise building's rooftop is shaded by the ventilation system. Furthermore, the surrounding urban environment also influences the solar irradiation received by building surfaces. Figure 2.15 illustrates the solar irradiation map from a side view of the EEMCS faculty building, showing significant shading on the lower region of the southern facade of the Electrical Sustainable Power (ESP) lab due to trees. In contrast, the saw-tooth-shaped rooftop of the low-rise receives the highest annual solar irradiation, suggesting a high PV potential yield.

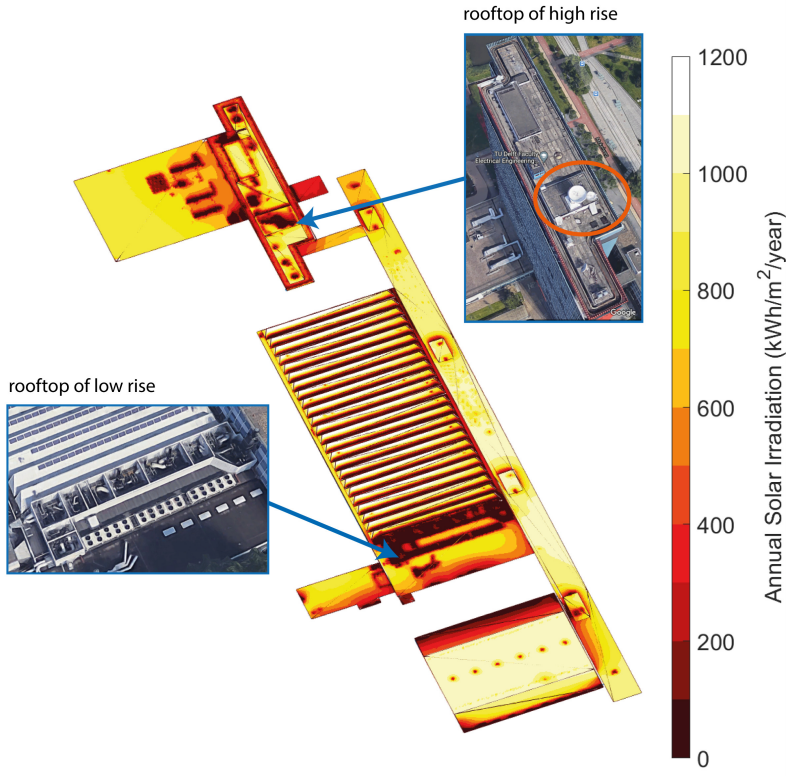

Figure 2.14: Annual solar irradiation map of the EEMCS faculty building from a bird view. The aerial photos are obtained from GoogleMap.

2.2.4. Annual DC yield map on buildings

The annual solar irradiation map provides information on the physical potential of building surfaces. However, directly applying the same grid points from this map to calculate DC yield often leads to an overestimation of the actual capacity of PV systems. This discrepancy primarily arises because certain portions of the roof surfaces are unsuitable for

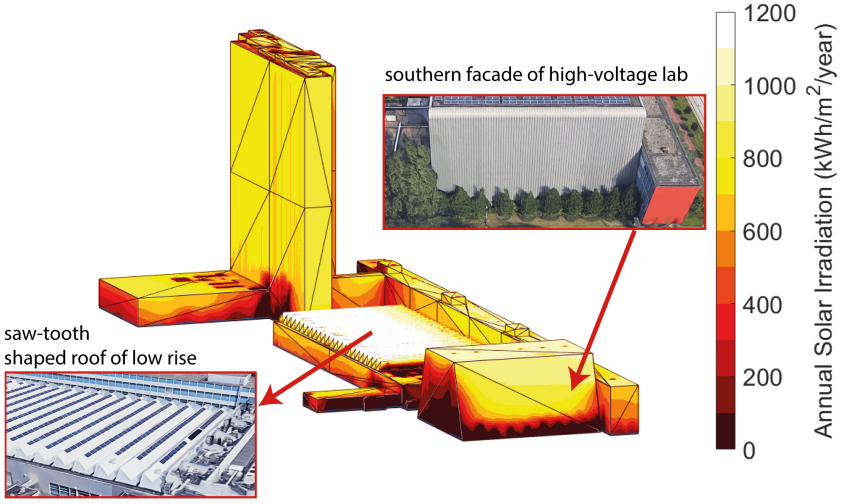

Figure 2.15: Annual solar irradiation map of the EEMCS faculty building from a side view. The aerial photos are obtained from GoogleMap.

PV module installation. Such areas may include spaces already occupied by rooftop artifacts or locations where the installation of PV systems is economically unviable, given current PV technology costs. Besides, general rules of PV system installation must also be followed, such as maintaining a certain distance from the roof edge and ensuring adequate row-to-row clearance. These guidelines inherently reduce the roof coverage ratio achievable by the PV system, consequently reducing system DC yield.

To more accurately simulate the annual DC yield, a panel-fitting algorithm is implemented across all building roof surfaces. This algorithm facilitates the arrangements of PV modules on these roof surfaces, accommodating user-defined dimensions and clearances. Figure 2.16 schematically illustrates the panel fitting process in a landscape configuration on a slanted roof. It starts with the projection of the roof surface onto the ground. A rotation matrix, M_R, is then applied to align the projected roof polygon with the intrinsic coordinate system. Depending on the roof orientation, this rotation may be clockwise or counter-clockwise to prevent inversion of the polygon. Subsequently, an original bounding box is defined for each roof polygon, within which a grid of PV modules is populated, considering the dimensions and clearances of the selected PV module, as shown in Figure 2.16d. For slanted roofs, no offset from the roof edge is considered, and the clearance between PV modules is maintained at 5 cm to facilitate maintenance access. After that, the algorithm evaluates the suitability of each module by verifying that all four corners of the module reside within the roof polygon and that the overlap between roof and module polygons is larger than 99%. Modules that fail to meet these criteria, marked in red in Figure 2.16e, are excluded from the configuration. Optimal panel placement is achieved through iterative adjustments, shifting the entire grid by predefined distances along the x and y axes in each iteration to maximize the number of

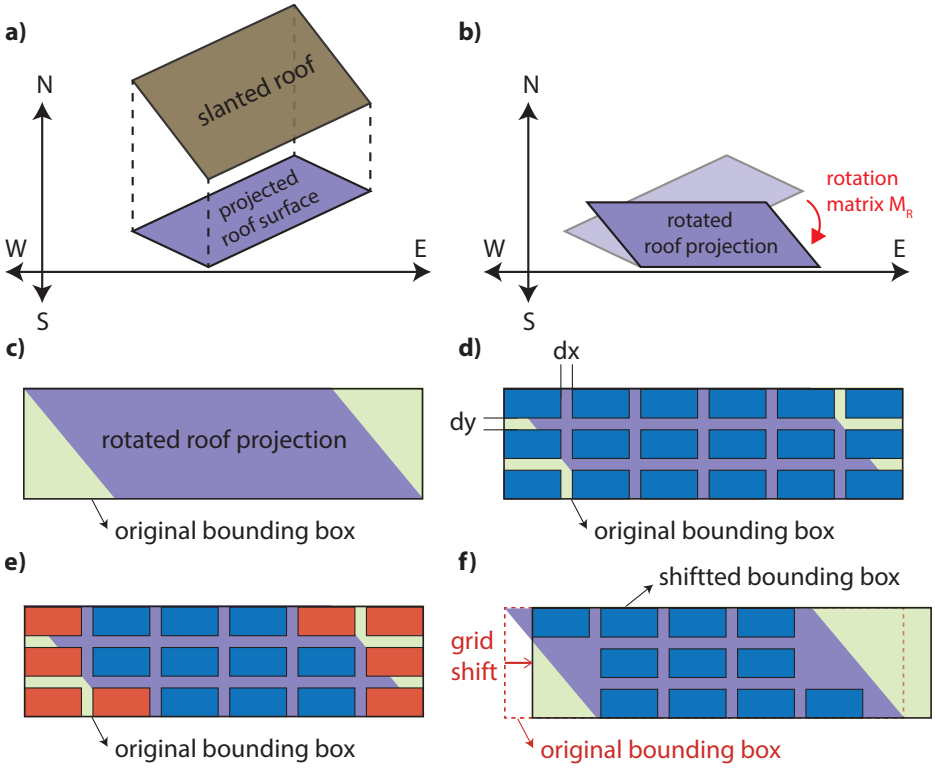

Figure 2.16: Schematic demonstration of the panel fitting algorithm: a) the roof surface is projected onto the ground plane; b) the roof projection is rotated using a rotation matrix to align with the intrinsic coordinate system; c) an original bounding box is created for the rotated roof projection; d) a grid of PV modules is established, adhering to the dimensions of the selected PV module and user-defined clearance; e) PV modules that cannot be accommodated on the roof surface are identified, and they are marked in red and removed; f) a grid shift is applied to the entire grid of PV modules to optimize the panel fitting result.

PV modules. The distances for grid shifting are defined by:

$$\begin{cases} x_{shift} = -(L_M + G_x) \cdot \dfrac{i-1}{i} \\ y_{shift} = -(W_M + G_y) \cdot \dfrac{i-1}{i} \end{cases} \tag{2.3}$$

where L_M is the module length, W_M is the module width, G_x is the clearance along the x-axis, G_y is the clearance along the y-axis, and i is the number of iterations. In a portrait configuration, module length and width in the equation are interchanged. To minimize computational effort, the number of iterations is adjusted based on the roof size: large roofs exceeding 300 m^2 undergo three iterations, small roofs under 100 m^2 are iterated eight times, while roofs of intermediate size execute five iterations. Figure 2.16f displays the panel fitting outcome following the grid shift, revealing that an additional PV module is accommodated in this revised arrangement compared to the initial setup. Finally, the fitted modules are reoriented using the transpose of rotation matrix M_R, and all module corners are projected back onto the roof plane so that the skyline can be correctly generated for PV output calculation. This step involves finding the intersection between the normal of PV corner points and the roof plane, as depicted in Figure 2.17. The coordinates of the intersection C can be calculated with variable t according to the following equation:

$$\begin{cases} x = b_1 + v_1 \cdot t \\ y = b_2 + v_2 \cdot t \\ z = b_3 + v_3 \cdot t \end{cases} \tag{2.4}$$

where

$$t = \frac{(a_1 - b_1) \cdot n_1 + (a_2 - b_2) \cdot n_2 + (a_3 - b_3) \cdot n_3}{n_1 \cdot v_1 + n_2 \cdot v_2 + n_3 \cdot v_3} \tag{2.5}$$

Here, point B represents the coordinates of a fitted PV module corner, while vector $\vec{v}$ is set to [0,0,1]. Point A specifies the coordinates of a roof surface corner, and the vector $\vec{n}$ denotes the normal vector of the PV module face, which is aligned with the roof surface normal in the case of slanted roofs.

Fitting panels onto flat roofs is more complicated. One challenge is that the roof surface normal cannot be directly used to determine its orientation, as the projection of the face normal vector onto the ground is only a 1D point. This issue is solved by using the directional vector of the longest roof edge as a reference to define roof orientation. Another challenge is determining the tilt and orientation of PV modules because they cannot be inherited directly from the roof. Given that the Netherlands is located in the northern hemisphere, PV systems on flat roofs should ideally face south to maximize POA irradiation. This optimal orientation is achieved by dividing the intrinsic coordinate system along its diagonals, as shown in Figure 2.18a, then the roof orientation is matched to the corresponding segment. If the roof orientation falls within the angle range segments A or C, the modules adopt this orientation. If the roof orientation is

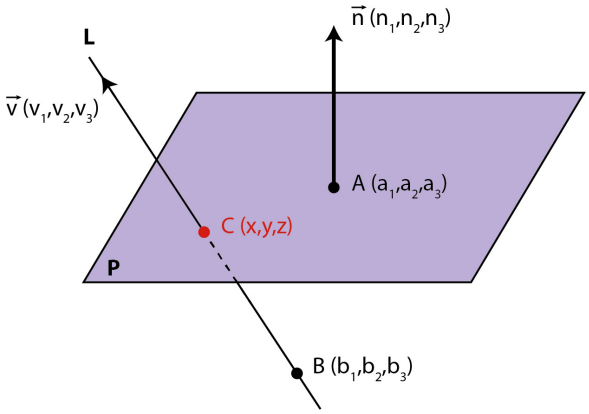

Figure 2.17: Schematic illustration of finding the intersection between the normal of PV module corners and the roof plane. Here, A represents a point on the plane, $\vec{n}$ is the plane's normal vector, and B is an arbitrary point that is not on the plane which defines line L with direction vector $\vec{v}$. Point C denotes the intersection between plane P and line L.

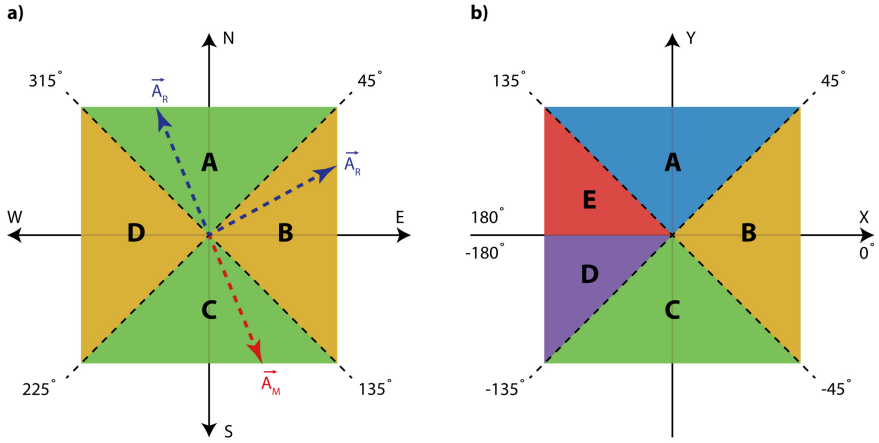

Figure 2.18: a) The intrinsic coordinate system, divided into four angle range segments. The module orientation vector $\vec{A}_M$ is aligned parallel to the roof orientation vector $\vec{A}_R$ for segments A or C, and perpendicular to $\vec{A}_R$ for segments B or D; b) The coordinate system is segmented into five sectors, each associated with a specific rotation matrix.

found in either angle range segment B or D, the module orientation is adjusted to be perpendicular to the roof orientation. Additional angle shifts are applied to ensure that roof orientation always ends up in segment C to face south.

The final challenge involves defining the correct rotation matrices to align the roof polygon with the intrinsic coordinate system. As depicted in Figure 2.19, the coordinates of the module polygon corners are arranged in a fixed order. Therefore, the projected roof polygon must be rotated to align with the appropriate axis to ensure that when the module polygons are projected back to the original flat roof surface, module corners 2 and 3 correctly represent the module tilt by lifting off from the roof surface geometrically. As an example, Figure 2.19c contains a projected flat roof polygon with the orientation $\vec{v}(v_1,v_2)$ defined by its longest edge. The rotation matrix M_R is applied so that the polygon is aligned with the x-axis for panel fitting. However, this can result in incorrect geometric module tilts due to improper lifting of the module corners when projected back. To mitigate this, different rotation matrices are employed, utilizing a four-quadrant coordinate system that mirrors the intrinsic system but spans an angle range of [-180°, 180°]. This system is divided into five segments as shown in Figure 2.18b, with each segment assigned a specific rotation matrix from Table 2.1, enabling the roof polygon to rotate minimally to align with either the X or Y axis for optimal panel fitting. Figure 2.19d demonstrates a scenario where the projected roof polygon is aligned parallel to the Y-axis, resulting in a correct geometric module tilt. The module grid generation follows the standard PV system mounting configuration on flat roofs in the Netherlands, where modules are tilted at 15° with a row-to-row spacing of 0.7 meters. Besides landscape and portrait configurations, a dual-tilt configuration is also investigated where PV modules are tilted at 12° with a row-to-row clearance of 0.2 meters. Its orientation is perpendicular to that of single-tilt PV systems rather than being exactly east-west oriented because this ensures an optimal packing density. It is worth mentioning that the dual-tilt configuration is not subject to power reduction when its orientation is off from the east-west. In fact, it benefits from such angle deviation by producing slightly more energy [72]. Additionally, flat-mounted PV systems with 0° tilt are considered for buildings under strict visual constraints, such as monumental buildings or those along the streets with a protected view, ensuring PV modules remain unseen from street level.

After obtaining the geographical coordinates of the fitted PV modules, a grid of eighteen uniformly distributed points is generated on each module plane for the annual DC yield calculation. Each point represents a group of four solar cells, totaling seventy-two solar cells per module. This approach effectively balances accuracy with computational efficiency. Before proceeding with the DC yield mapping, one more issue needs to be tackled. As noted in section 2.2.2, the reconstruction of 3D building models does not account for rooftop artifacts. Consequently, this oversight leads to an overestimation of the feasible PV module placement, as illustrated in Figure 2.20a. To solve this, annual solar irradiation is first calculated for each point on the module, and points falling below the irradiation threshold (<600 kWh/year) are filtered out. This threshold also helps to eliminate modules that suffer from moderate shading caused by nearby tall buildings or large vegetation. The DC yield for the remaining modules is computed using the simplified skyline-based method, with the results averaged across the 18 points. Modules yielding less than 650 kWh/kW$_p$ are excluded due to their economic infeasibility. The final

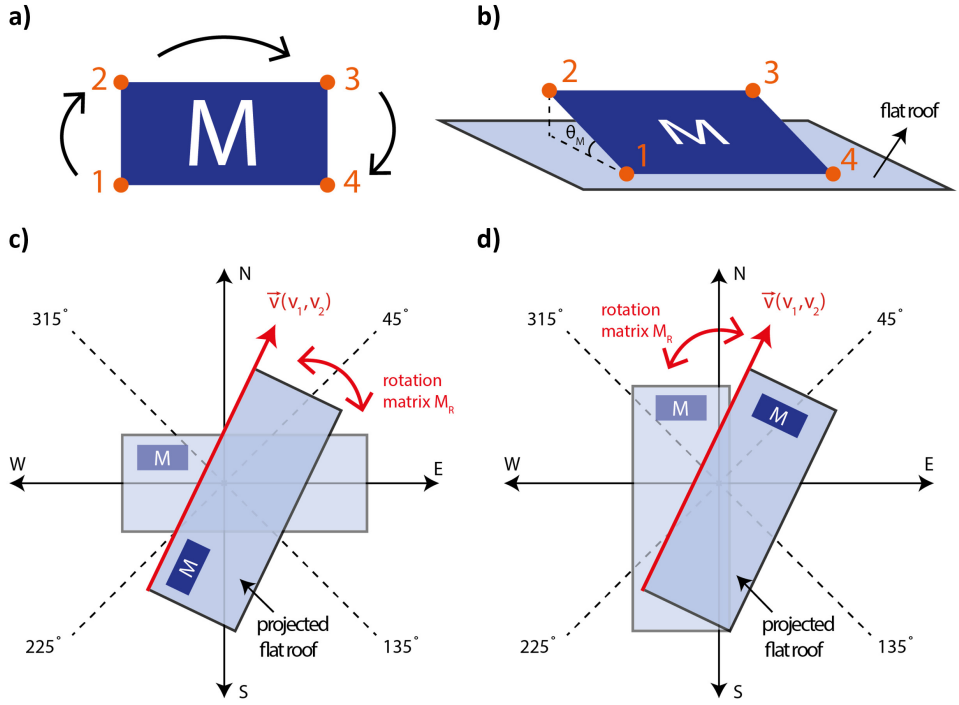

Figure 2.19: Illustration of the panel fitting process on flat roofs: a) Module corners are stored in a fixed order to facilitate the creation of the geometrical module tilt; b) Module corners 2 and 3 are elevated from the flat roof at a predefined tilt angle; c) Incorrect alignment of the rotated roof projection with the wrong axis, resulting in an improper representation of the module tilt; d) Correct alignment of the rotated roof projection with the proper axis, ensuring an accurate geometrical module tilt representation.

Table 2.1: Rotation matrices for different segments

Segment	Rotation Matrix
A	$\begin{bmatrix} \cos\left(\frac{\pi}{2}-\alpha\right) & -\sin\left(\frac{\pi}{2}-\alpha\right) \\ \sin\left(\frac{\pi}{2}-\alpha\right) & \cos\left(\frac{\pi}{2}-\alpha\right) \end{bmatrix}$
B	$\begin{bmatrix} \cos(-\alpha) & -\sin(-\alpha) \\ \sin(-\alpha) & \cos(-\alpha) \end{bmatrix}$
C	$\begin{bmatrix} \cos\left(\frac{\pi}{2}-\alpha\right) & -\sin\left(\frac{\pi}{2}-\alpha\right) \\ \sin\left(\frac{\pi}{2}-\alpha\right) & \cos\left(\frac{\pi}{2}-\alpha\right) \end{bmatrix}$
D	$\begin{bmatrix} \cos(-\pi-\alpha) & -\sin(-\pi-\alpha) \\ \sin(-\pi-\alpha) & \cos(-\pi-\alpha) \end{bmatrix}$
E	$\begin{bmatrix} \cos(\pi-\alpha) & -\sin(\pi-\alpha) \\ \sin(\pi-\alpha) & \cos(\pi-\alpha) \end{bmatrix}$

PV system layout, displayed in Figure 2.20b, shows that this filtering process effectively removes several modules, particularly those conflicting with the positioning of rooftop ventilation systems.

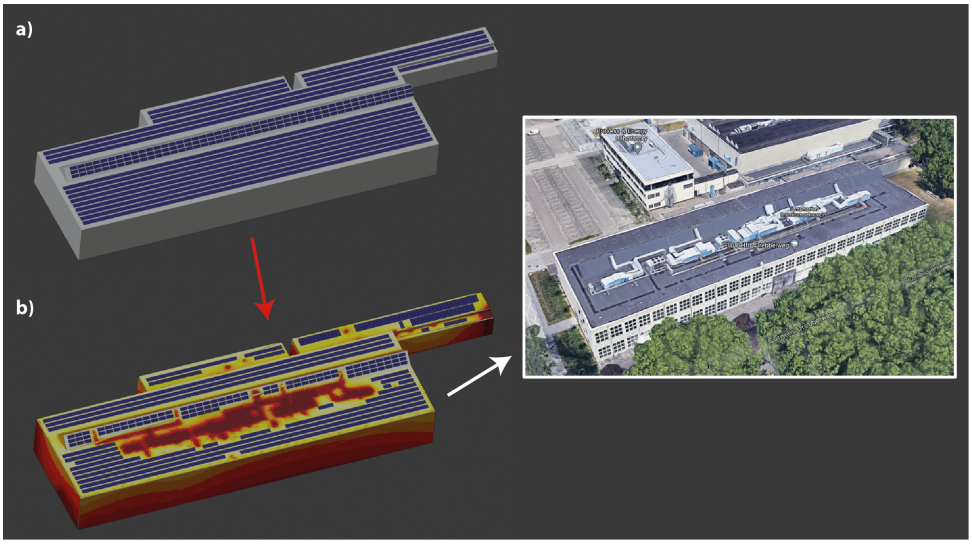

Figure 2.20: Panel fitting results for Building 35 on the TU Delft campus: (a) The rooftop is fully populated with PV modules based on the module dimensions and mounting configuration; (b) Modules receiving minimum irradiation below 600 kWh/year and specific yields less than 650 kWh/kW$_p$ are excluded. The aerial photo is sourced from GoogleMap (Imagery © 2021 Google, Imagery © 2021 Aerodata International Surveys, Maxar Technologies, Map data © 2021).

Another challenge with the current PV system configuration on flat roofs involves the row-to-row mutual shading. N. Alam et al. developed a real-time shadow simulation model based on LiDAR and CityGML models, where line-plane intersection checks are applied to capture various shading scenarios on PV modules [73]. Considering the input data availability and the objective of this work, the power reduction caused by mutual shading is accounted for by incorporating the points representing the fitted PV modules into the DSM. Figure 2.21 compares the DSM of building 35 with or without the inclusion of module geometry. It is clear in Figure 2.21c that the DSM modification replaces the original roof surface points with those of the module points. This update in environmental features is integrated into the skyline profile generation, leading to a different set of SVF and SCF for DC yield calculation. Meanwhile, particularly for portrait configuration, the DC yield for each module is determined by the annual energy output of the bottom cell string due to the by-pass diode effect. This effect is not accounted for in landscape configurations, where the connection of solar cells to the bypass diodes typically offers greater resilience to mutual shading.

The DC yield for facades is mapped without panel fitting due to the shortage of digital facade information, such as the location of windows. Therefore, the facade DC yield map is generated based on surface points, similar to the method used for generating the annual solar irradiation map. To quantitatively assess facades, we employ the open/closed

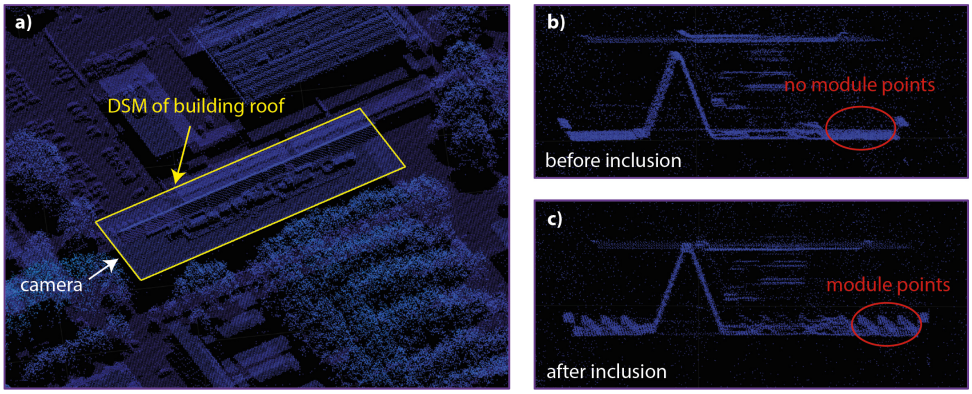

Figure 2.21: Modification of the urban environment demonstrated through the DSM of Building 35: a) DSM overview of the building roof, with 'camera' indicating the perspective for generating subfigures b and c; b) original roof plane DSM without the inclusion of module points; c) manipulated roof plane DSM where points representing fitted modules are integrated into the urban context.

ratio, which is derived from GoogleMap StreetView images. This involves visually estimating the areas covered by windows and walls, as depicted in Figure 2.22. Windows, indicated by red polygons, are classified as open surfaces. They are good candidates for transparent PVs, and it is assumed these surfaces will generate 10% of the power compared to traditional PV modules. Walls, as indicated by the green polygons, are classified as closed surfaces. Their DC yield is computed by multiplying the closed ratio by the total facade DC yield, which is aggregated from all surface points. Economic thresholds are not applied in this analysis to prevent excessive filtering of viable facade surfaces.

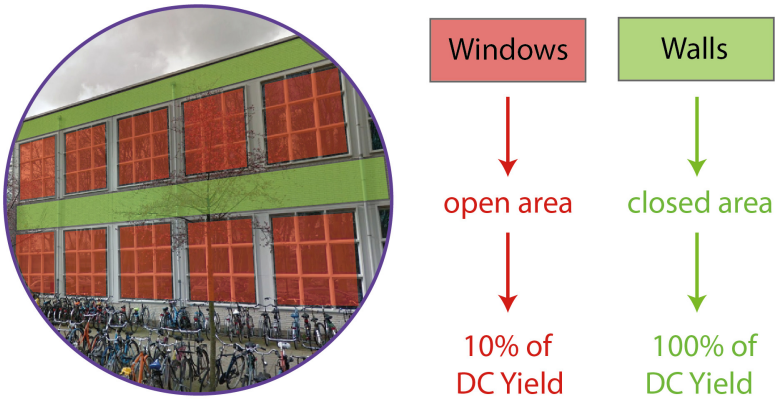

Figure 2.22: Facade DC yield mapping: Windows, marked by red polygons, are assumed to deliver 10% of the power compared to classic PV modules, suitable for transparent PV applications. Walls, highlighted in green polygons, are calculated to deliver full power.

2.2.5. Annual AC yield map on buildings

Energy yield on the AC side is calculated by considering a series of system losses. A key factor in this calculation is the inverter conversion efficiency, determined using the SNL model, where 4 inverters with different nominal AC output power are chosen (1.5 kW, 3 kW, 6 kW, and 12 kW) [74]. These are designed to accommodate 5, 10, 20, and 40 selected PV modules, respectively. The type and number of inverters assigned to each rooftop PV system are estimated based on the maximum number of PV modules determined from the panel fitting results. The workflow for selecting inverters is schematically illustrated in Figure 2.23. To calculate inversion efficiency, efficiency curves for each inverter are generated using the SNL model coefficients. The conversion efficiency for each PV system is then determined by locating the ratio of the system's annual DC yield to the estimated annual P_{dc0} of the inverters on these curves (here 4380 hours of operating time are assumed). Fixed conversion efficiencies are also considered for MPPT (98%), ohmic loss (99%), module mismatch (99%), and soiling loss (98%), which are used to compute the overall DC-AC conversion efficiency [75]. For facades where panel fitting is not performed, a fixed DC-AC conversion efficiency of 91% is assumed.

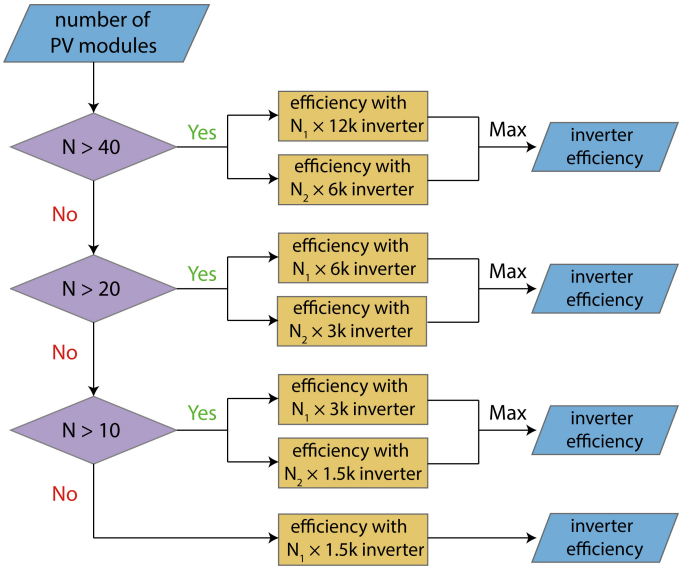

Figure 2.23: Algorithm of determining the type and number of inverters used to estimate the inversion efficiency of rooftop PV systems, where N_1 and N_2 indicate the number of inverters.

2.2.6. Roof segments classification

Finally, the roof segments are categorized based on the specific yield of the PV systems installed. Three categories are defined, and each is assigned a distinct color: red for yields between 650 and 800 kWh/kW$_p$, yellow for yields between 800 and 950 kWh/kW$_p$, and green for yields exceeding 950 kWh/kW$_p$. The results of each step in the workflow are illustrated in Figure 2.24, showcasing Building 35 at the TU Delft campus. The AC

yield map appears generally darker than the DC yield map, reflecting system losses. Additionally, the roof classification map provides insights into which roof surfaces should be prioritized for PV integration based on their potential yield.

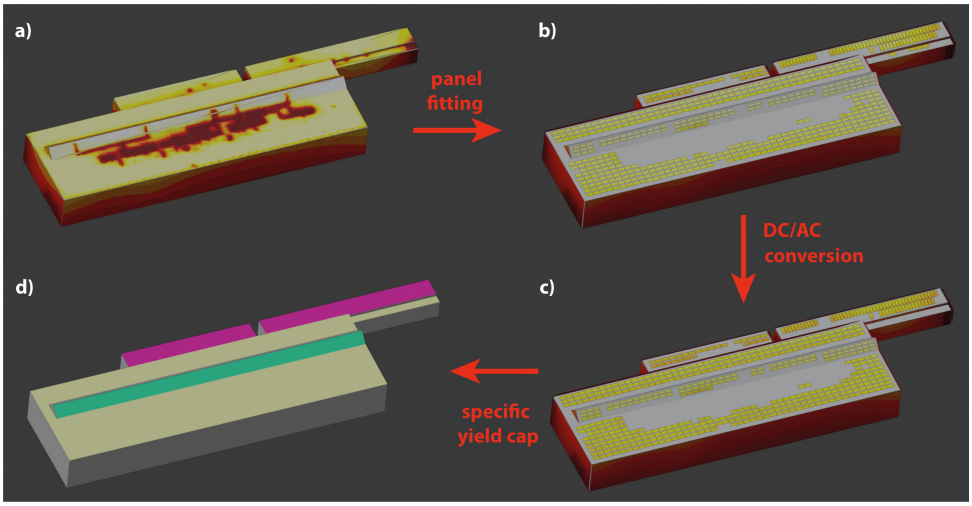

Figure 2.24: The simulation results on Building 35 on the TUD campus include a) the annual solar irradiation map, b) the annual DC yield map, c) the annual AC yield map, and d) the roof classes categorized based on the specific yield of the rooftop PV system.

2.3. Results and discussion

2.3.1. Computational speed

The simulation time for each step involving Building 35 is detailed in Table 2.2, highlighting that the mapping of DC/AC yield is the most time-consuming process, followed by annual solar irradiation mapping. Generating DC/AC yield maps consumes time primarily because prior to this step, each point on the POA requires solar irradiation calculation to identify modules significantly affected by shading. This shading may result from conflicts with rooftop obstacles or the surrounding environment. Additionally, the DC/AC yield mapping is conducted on a denser grid of 18 points per module, with each point representing an area of approximately 0.1 m^2. This naturally leads to longer computational effort in contrast to the 0.25 m^2 point density used for the solar irradiation map. One approach to reducing the computational time for DC/AC yield map generation would be simultaneously calculating the module DC/AC yield during the exclusion of shaded modules. Currently, these two operations are executed independently, meaning that the HorizonScanner is executed doubly to generate the skyline. Another potential approach to significantly reduce computational time could utilize machine learning or look-up tables. By leveraging the results from the annual solar irradiation map, primary values could be used to predict secondary values for DC/AC yield, streamlining the entire process.

The computational speed per step is averaged over the area of all simulated TU Delft

Table 2.2: Breakdown of the simulation time of Building 35 on TU Delft Campus

Process	**Time [s]**
Barycentric coordinate system	0.3
Generation of solar irradiation map	172
Panel fitting on roofs	76
Generation of DC & AC yield maps	276
Roof segment classification	0.1
Total simulation time	**524 [s] = 8.7 [min]**

buildings, and the results are listed in Table 2.3. The overall computational speed is found at 0.085 s/m^2 with a standard deviation (SD) of 0.044 s/m^2. Panel fitting shows relatively the highest SD because the iteration of grid shift depends on the size of the roof. Roofs with an area larger than 300 m^2 iterate 3 times while those with an area smaller than 100 m^2 iterate 8 times. The rest of the roofs undergo 5 iterations. Therefore, for buildings with many small roofs, the speed is lowered due to more iterations.

Table 2.3: Computational speed per step for solar PV potential map generation in MATLAB

Process	**Averaged Speed [s/m^2]**	**Standard Deviation [s/m^2]**
Barycentric coordinate system	5.67E-05	3.98E-05
Generation of solar irradiation map	0.016	0.006
Panel fitting on roofs	0.015	0.011
Generation of DC & AC yield maps	0.054	0.027
Overall computational speed	**0.085**	**0.044**

Figure 2.25 compares the annual solar irradiation maps generated before and after building model refinement. A key limitation of using the unrefined model for solar potential calculations is the discrepancy in tilt and orientation between adjacent triangles, which can yield significantly varied results. This discrepancy often manifests as unexpected dark spots scattered across the roof surface, as depicted in the figure. Additionally, in the unrefined scenario, solar irradiation calculation is performed for rooftop obstacles. This is evident from the higher irradiation value at the region where obstacles sit, which can overestimate the geographical potential. In terms of computational efficiency, the unrefined model requires 37 minutes to generate surface sampling points (the center point of each triangular mesh) and to perform solar irradiation mapping. In contrast, the refined model operates 13 times faster, as detailed in Table 2.4. For the unrefined model, the roof surface area is calculated by aggregating the areas of all triangular meshes, yielding a total that is approximately 8% larger than that obtained with the refined model. This discrepancy is primarily attributed to the misalignment of the triangular meshes. A more accurate approach would involve using the projection area of the triangular meshes for calculations. Despite these discrepancies, the total annual irradiation reported for both models is closely aligned, with the unrefined model showing a roughly 3% higher result. This increase is partly due to the undesired inclusion of irra-

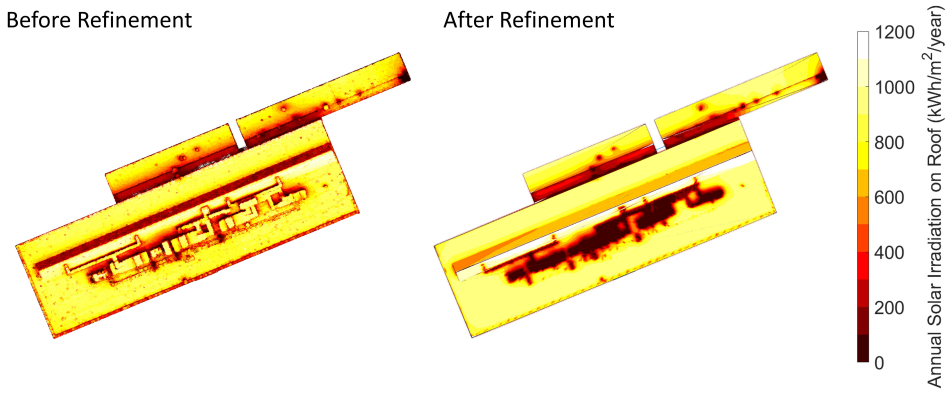

Figure 2.25: Annual solar irradiation maps on building 55 before and after 3D building model refinement.

diation from rooftop obstacles. While misalignment between triangular meshes might also contribute to this deviation, its effects could potentially offset when considered at the scale of the entire roof plane.

Table 2.4: Comparison of computational speed and simulation results of building 55 before and after 3D building model refinement

Metric	**Unrefined Model**	**Refined Model**
Surface points generation [s]	79.9	0.31
Generation of solar irradiation map [s]	2149.9	172.1
Roof surface area [m^2]	4417	4075
Total roof annual irradiation [GWh/year]	3.03	2.95

2.3.2. Solar PV potential maps on TU Delft campus

Table 2.5 lists the simulation results of Building 35, detailing three specific building surfaces as shown in Figure 2.26. Given the unrestricted conditions of this building, three mounting configurations are evaluated for the flat roof surface. The dual-tilt configuration delivers the highest number of PV modules on roof 1, primarily due to a reduction in row-to-row clearance, which substantially increases packing density. The landscape configuration exhibits the highest specific yield, whereas the portrait configuration yields the lowest. This discrepancy is largely attributed to mutual shading between rows, which significantly reduces the power output in portrait configurations. Despite not offering the highest specific yield, the dual-tilt configuration produces the greatest system DC and AC yield, owing to its larger overall system size. In fact, dual-tilt is found to be the optimal mounting configuration for the majority of flat roofs in this study in terms of energy output, as it effectively offers higher packing density against a modest decrease in power production per module. For roof 2, both landscape and portrait configurations deliver comparable specific yields, peaking at approximately 1014 kWh/kW_p.

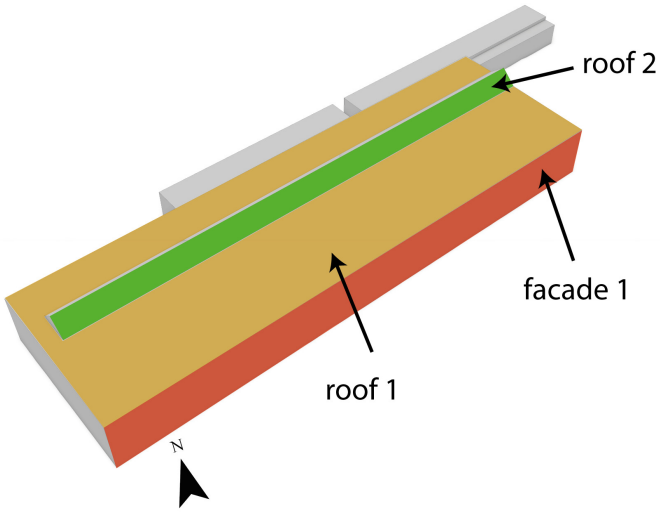

Figure 2.26: Three specific building surfaces of Building 35 on the TUD campus, including the flat roof (colored in yellow), the slanted roof (colored in green), and the facade (colored in red).

Table 2.5: The numerical simulation results of Building 35 on the TUD campus, where three building surfaces are analyzed in detail.

Mounting Configuration	**Number of Modules**	**Specific Yield [kWh/kWp]**	**DC Yield [MWh]**	**AC Yield [MWh]**
		Roof 1 (flat)		
Landscape	376	921.9	126.5	116.3
Portrait	442	772.3	124.6	114.3
Dual-tilt	549	835.5	167.4	153.7
		Roof 2 (slanted)		
Landscape	94	1003.9	34.4	31.7
Portrait	80	1013.9	29.6	27.2
		Facade 1		
Area [m^2]	**Closed Ratio**	**Open Ratio**	**DC Yield [MWh]**	**AC Yield [MWh]**
1104.4	45%	55%	32.1	29.0

This better system performance compared to roof 1 is mainly due to an optimal module tilt of 41°directly inherited from the roof. Conversely, the facade demonstrates significantly lower energy yield, with a unit AC yield of 26 kWh/m^2/year. This low performance can be attributed to two factors: i) vertical facades are generally subject to lower SVF, which limits the amount of incident irradiance, and ii) the presence of tall trees in front of the building, which cast extensive shadows on the facade, as illustrated in Figure 2.15.

The same simulation was conducted across all buildings on the TU Delft campus, revealing that a total of 8.1 GWh/year of PV potential could be harvested. Roofs contribute approximately 4.7 GWh/year, while facades account for the remaining 3.4 GWh/year. Given that no panel fitting was performed for the facades, the economic threshold of 650 kWh/kW$_p$ was adjusted to 113 kWh/m^2, based on the peak power and dimensions of the selected module. This analysis identified only two facades across the campus that meet this threshold, with their combined annual AC yield totaling 118.2 MWh/year, representing only 3.5% of the potential yield without filtering. Applying the same economic threshold to the facades results in a lower total annual AC yield of 4.8 GWh/year, demonstrating roof surfaces as low-hanging fruits for PV integration on campus. To effectively present these findings, a high-resolution 3D solar PV potential map has been published as a web scene, with a screenshot of the annual solar irradiation map available in Figure 2.27. This web map is accessible via a personal Google account and includes visualizations of all simulation results, including 3D building models, annual solar irradiation, panel fitting on roofs, DC yield map, AC yield map, and roof classifications. The detailed modeling methods applied to roofs provide a high level of confidence in the rooftop solar PV potential, whereas the potential for facades is considered less reliable due to the scarcity of detailed digital facade information. Consequently, the technical potential for facades is likely overestimated, as calculations unexpectedly include surfaces unsuitable for module installation, such as narrow walls between windows.

The total electricity demand on the entire campus is 82.6 GWh/year, meaning that roughly 10% of the current electricity demand can be supplied by roof and facade PVs based on this study [76]. It is important to note that this estimate presumes all generated PV electricity is directly consumed on-site, without accounting for possible losses during storage or retrieval from the grid, which effectively acts as a large battery. Furthermore, this analysis assumes grid parity, where the Levelized Cost of Electricity (LCoE) from PV systems is equal to or less than the cost of purchasing grid electricity. However, achieving the ambitious goal of covering 50% of the campus's electricity consumption with renewable sources by 2030 remains a significant challenge. To enhance PV penetration, ongoing studies are essential. These should explore expanding solar PV mapping to include open areas and waterways and employ higher efficiency PV modules in simulations to boost potential yield. Additionally, the development of new buildings in the south of the TU Delft campus presents further opportunities for PV integration. If these new constructions are designed to be more energy-efficient and PV installation-friendly, they can potentially increase the proportion of campus electricity needs met by solar power beyond the current 10%.

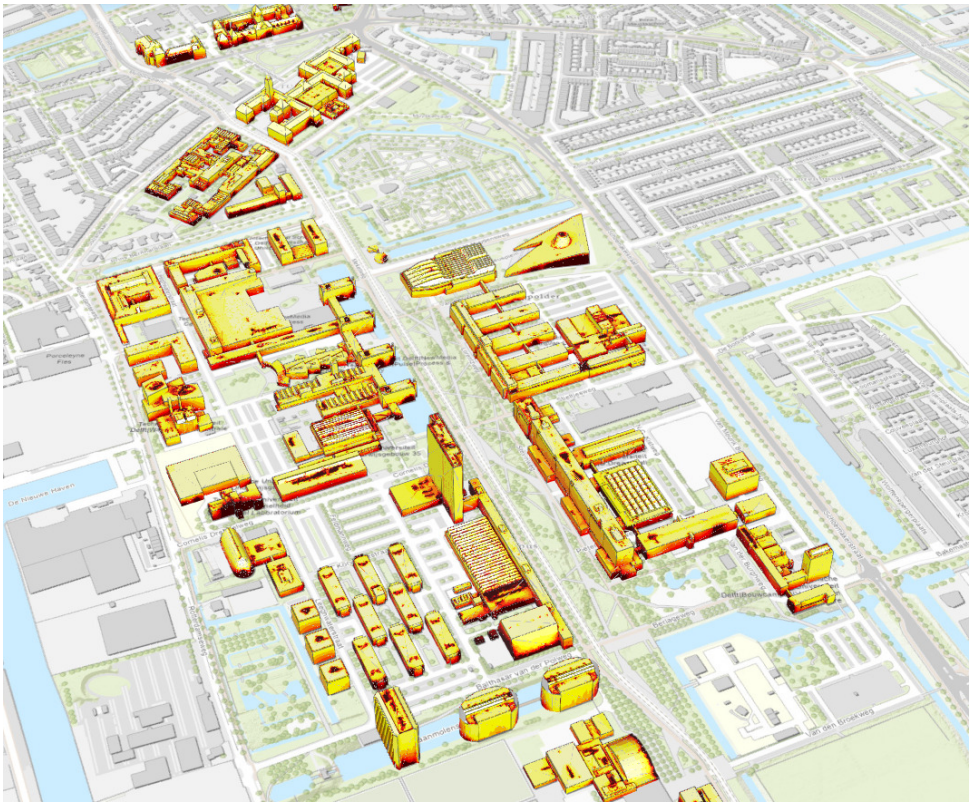

Figure 2.27: Annual solar irradiation map for the TU Delft campus (https://arcg.is/1iP9nb1). All simulation results are accessible by logging in with a personal Google account.

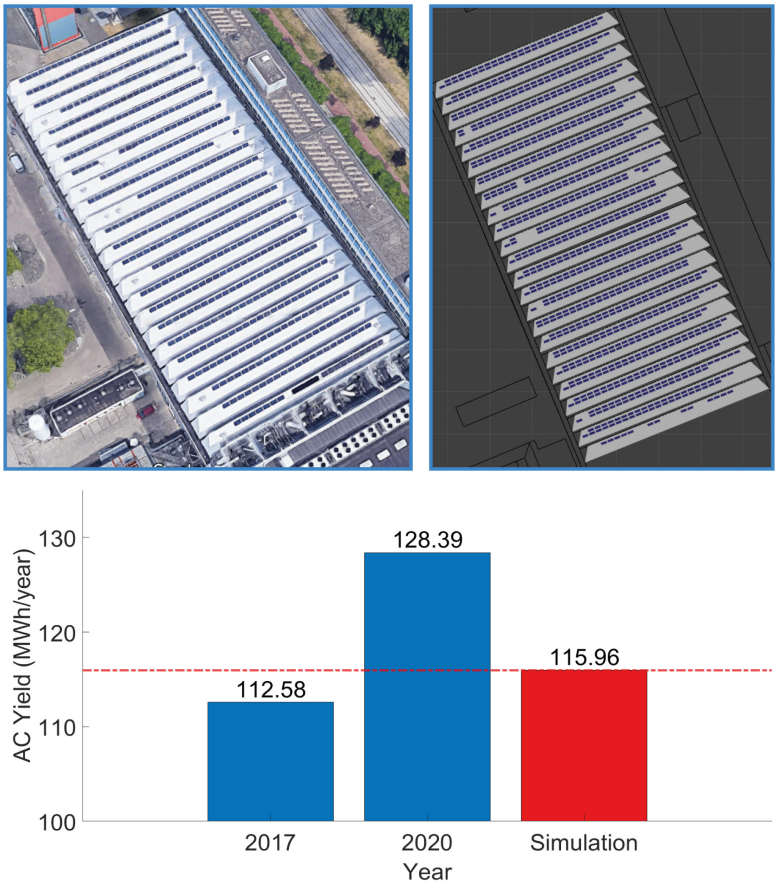

Figure 2.28: Validation of the simulation results by analyzing the PV system installed on the low-rise building of the EEMCS faculty. The algorithm maximizes roof utilization as long as the economic thresholds are met, leading to a double amount of PV modules compared to the actual case. The simulation result aligns well within the variation range provided by CRE, with actual system output data in 2017 and 2020 presented.

2.4. Validation study

The PV system installed on the low-rise building of the EEMCS faculty is analyzed to validate the simulation results. Currently, the roof hosts 521 PV modules, as depicted in the GoogleMap image in Figure 2.28. Based on the data provided by Campus Real Estate (CRE), this system has a total capacity of 133.56 kW_p, which corresponds to a peak power of 255 W_p per module. Figure 2.28 also displays the final panel fitting results, where our algorithm accommodates 1064 PV modules. This nearly doubles the actual number of modules, as our algorithm maximizes roof utilization as long as the economic thresholds are met. In terms of energy yield, our simulation predicts an annual AC output of 236.82 MWh/year. After applying a module number correction factor of 0.4896, this figure is adjusted to 115.96 MWh/year. When compared to actual system outputs of 112.58 MWh/year in 2017 and 128.39 MWh/year in 2020 provided by the system operators, our simulation aligns well within this variation range, demonstrating high fidelity in our modeling approach.

2.5. Conclusions

In this chapter, an innovative workflow designed to assess solar PV potential within urban areas was presented, with the TU Delft campus serving as a case study. This approach begins with the semi-automatic reconstruction of 3D building models, utilizing LiDAR data and building footprints. It initially reconstructs the original building models in ArcGIS Pro, and then these models are refined using Blender to enhance their accuracy and suitability for further analysis. Once refined, the highly precise 3D models are imported into MATLAB, and a barycentric coordinate system is applied to create a uniformly distributed grid with a resolution of 0.5 meters on the building surfaces. These sampling points are used to calculate the annual solar irradiation, using a simplified skyline-based method developed in-house.

This workflow extends beyond assessing the physical potential of PV installations to include additional analyses of both technical and economic viability. Initially, each roof segment is populated with PV modules of specified dimensions and clearance requirements. A grid shift method is then applied to determine the maximum feasible panel fitting scenario. The same simplified skyline-based method is employed to compute the annual POA solar irradiation and DC yield. To maintain a balance between accuracy and computational efficiency, a grid of eighteen points per module is utilized. Modules obstructed by rooftop features are excluded if any of these eighteen points receives less than 600 kWh/m^2/year of solar irradiation. Additionally, modules yielding less than 650 kWh/kW_p are discarded to ensure economic feasibility. The study specifically addresses the challenges associated with flat roofs by examining three mounting configurations: landscape, portrait, and dual-tilt. These configurations consider not only their physical feasibility but also potential yield reductions due to row-to-row mutual shading and the bypass diode effect. Roof segments are then categorized into three classes based on the specific yield of the installed PV systems. To further calculate the AC yield of rooftop PV systems, the SNL model is used, and their inverter efficiency is estimated.

The approach to calculating DC and AC yields for facades differs due to the lack of digital facade data. Instead, the open/closed ratio, estimated from Google Street View

images, is used to determine facade DC yields. It is assumed that closed surfaces (walls) deliver 100% of the calculated DC yield, while open surfaces (windows) contribute 10% of the DC yield. The final solar PV potential maps have been published in an ArcGIS web scene and are accessible using a personal Google account. This allows for dynamic interaction with the data and visualization of the spatial distribution of PV potential yields across different building surfaces.

The simulation result shows that a total of 8.1 GWh/year PV potential can be harvested from campus building roofs and facades. As the study demonstrates, this contributed modeling framework paves the way for a quick and accurate assessment of PV potential (from physical potential to economic potential) across large-scale and complex urban environments.

3

Social impact of urban PV deployment

This chapter is based on the following publication:

Y. Zhou, D. Wilmink, M. Zeman, O. Isabella, and H. Ziar, *A geographic information system-based large scale visibility assessment tool for multi-criteria photovoltaic planning on urban building roofs*, Renewable and Sustainable Energy Reviews **188**, 113885 (2023). (DOI: https://doi.org/10.1016/j.rser.2023.113885)

3.1. Introduction

The integration of PV into urban environment is set to be the main contributor to the global transition to green energy. Building rooftops are particularly good hosts for PV system installations, considering their vicinity to energy consumption and the open space scarcity in urban areas. In fact, studies have shown that rooftop PV systems have substantial potential for green electricity generation. It is stated in a report published in 2014 that the annual rooftop solar electricity production in the Netherlands can reach up to approximately 50 TWh, which comes down to almost 46% of the total national electricity consumption in 2023 [77, 78].

Despite the promising energy potential, designing, allocating, and maintaining urban PV systems are often challenging due to sub-optimal irradiation caused by unfavorable roof tilt and orientation. Additionally, the complex urban morphology creates intricate shading patterns, which significantly reduce solar access and impede the deployment of PV systems. To overcome these challenges, a comprehensive workflow was presented in Chapter 2 to assess the PV potential in the urban environment from physical to economic levels. However, the decision-making process in urban PV planning is not solely limited to technical or economic concerns. Social considerations will also play a crucial role in determining the viability of rooftop PV system installation [79]. Monumental buildings, for instance, are often restricted from changing their appearance due to their architectural and historical values. Installing and integrating PV systems on such

buildings requires additional visual impact analysis, as the contrasting color of PV modules compared to traditional building materials can affect the building's identity in its context [80]. This means that in some cases, identifying suitable roof surfaces for PV installation is not only dependent on the potential energy yield but also highly influenced by the visibility of these roof surfaces to the public domain and their social value. In the Dutch city of Delft alone, there are over 1500 monumental buildings. This makes large-scale visibility assessment of roof surface useful to find as much suitable roof surface area as possible for PV installation. In general, there are three primary methods to perform the visibility assessment: i) consulting the urban planning experts, ii) surveying the general public, and iii) using spatial modeling and analysis [81]. These three methods are applied flexibly in the context of solar energy planning, with one or more methods being used depending on the specific requirements of the project and data source availability.

For the utility-scale solar power plant which is typically large and features centralized installations, it may pose a negative visual impact on the nearby residents by introducing contrasting artifacts into the natural landscape [82]. Ana et al. have conducted a combined analysis on the aesthetic impact of solar power plants, where they proposed an expert model that derives four key indicators from photographs: visibility, color, fractality, and the local atmospheric condition. By calculating the weighted sum of these factors, the visual impact of the facility is determined and further validated with the public preference approach [83]. The same model is adapted and utilized to study the aesthetic impact of four PV power plants, but the accuracy of obtaining the color indicator from photographs is constrained by the weather condition under which the photo is captured [84]. Another method addressing both spatial and perceptual aspects was developed by Marcos et al. [85]. This approach delivers two visibility maps where the Boolean map indicates the binary visibility of the PV plant from a given location, and the visual perception map conveys the view angle of the PV plant from the affected location. Additionally, by taking into account the number of daylight hours, the potential observation hour can also be calculated which represents the aggregated value of the maximum number of hours in an average day that an object may be visible to each potential observer [86]. A comprehensive methodology that incorporates all three visibility assessment methods is introduced by J.C. Diego et al., in which seven perceptual parameters are used to conduct the visual impact analysis in both quantitative and qualitative manners [87].

Rooftop solar PV systems, which are typically smaller in size and feature decentralized installations, pose a greater visual impact on the built landscape. The fact that these systems are usually spread across various locations on different buildings makes the visibility analysis more fragmented. A widely used approach to evaluate the visibility and integrity of PV placement is the LESO-QSV method [88]. This method establishes two main categories: urban surface criticity including system visibility and context sensitivity, and the system integration quality, which is dependent on the factors such as system geometry, materiality, and pattern obtained from photographs. It generates an acceptability grid that offers users an indication of the aesthetic impact of the PV system, thereby assisting in the decision-making processes. The system visibility is determined with a spatial model that is extensively explored in the research conducted by Florio et al. [81]. Based on this model, a comprehensive method is proposed to estimate the energy generation potential of visually-accepted PVs, building energy consumption and

economically viable microgrid operation [89]. Lingfors et al. approached the visibility analysis from the perspective of vantage points on the ground rather than the building envelope itself [90]. It is found that using vantage area instead of discrete vantage points leads to higher visibility for roofs. Drawing on alternative multi-criteria decision-making approaches, Thebault et al. utilized the ELECTRE TRI method to categorize the suitability of roofs for PV integration [91]. In a related study, Sun et al. assessed the feasibility of building-integrated PV (BIPV) by examining both solar energy harvesting potential and visual impact [92]. Additionally, they investigated the visual impact of hypothetical colored BIPV retrofits within the urban context using saliency mapping algorithm [93].

These methods necessitate inputs such as photographs or vector-based building models, which are either weather condition dependent or difficult to acquire; thus, their applications are limited for scaling up and vast area assessment. The aim of this research is to develop a GIS-based large-scale visibility assessment tool that relies on minimal input datasets. In this work, a tool is developed that evaluates both the visibility of the surface and its visibility degree. This tool operates in a raster-based representation of the environment generated from freely available LiDAR data, along with cadastral data and road networks representing the public domain. The output contains the roof surface visual amplitude map which not only tells the binary visibility of the roof cell, but also shows how visible they are by categorizing the roof cells into low, medium and high visibility groups. The computational demand is reduced by using parallel computing and an observer filter based on the roof surface tilt and orientation. The visibility assessment target can be alternated between roof cells and observer points, depending on which has fewer points. A sensitivity analysis is also incorporated for every roof surface, and the assessment terminates when the optimal assessment range and observer spacing are found. Additionally, the in-house developed solar PV mapping tool is employed to perform the solar PV potential analysis [15]. As a result, in addition to visibility maps for roof surfaces, this tool can also deliver results including the possible layout of the rooftop PV system, visibility categories for each module, and their annual AC yield. To demonstrate, this tool is applied to all the monumental buildings on the TU Delft campus.

3.2. Methodology

A complete flowchart is shown in Figure 3.1, in which the steps mentioned previously are grouped into two clusters: input data preparation and visibility and yield assessment.

3.2.1. Input data preparation

The difficulties encountered when performing urban studies mainly lie in the perplexing urban morphology. Therefore, the crucial initial step in an urban-centric analysis involves acquiring a precise and comprehensive representation of the urban environment. This is achieved by employing the DSM generated from LiDAR data. Another important input is the public domain which establishes the observer points when performing the visibility assessment. While an infinite number of observer points could exist within the public domain, this is not feasible for practical applications. As such, a finite representation of the possible public domain must be determined. In this project, points that represent roads or streets are chosen, as these are the primary pathways peo-

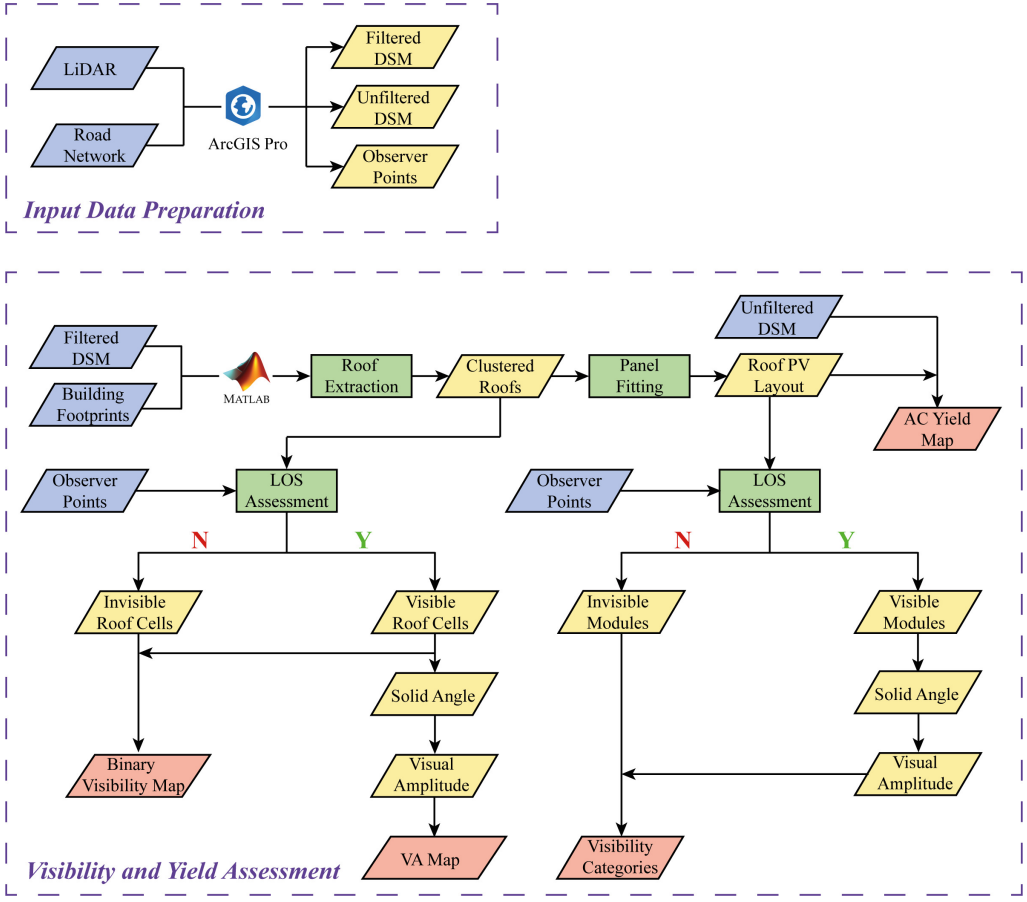

Figure 3.1: Workflow of the methodology divided into two parts: data preparation, and visibility and yield analysis. The color code for the blocks: blue for input data; yellow for intermediate output; green for operation; and red for final output. Acronyms: Digital Surface Model (DSM), Line-of-Sight (LOS), Visual Amplitude (VA).

ple use for transit between locations; in other words, these are the regions where most of the traveling happens and possess a high probability of PV modules being visible. This road network is sourced from GeoFabrik, which provides data in the form of a set of lines that define roadways [94]. Equally-spaced points are generated along the lines and subsequently mapped onto the DSM. An additional 1.7 meters in vertical elevation is added to all the points to simulate the average human eye height. Figure 3.2 examples two DSMs of part of the TUD campus with the public domain featured by red points. The primary distinction between these two DSMs is the presence or absence of vegetation: Figure 3.2a displays the unfiltered environment and is utilized for conducting PV potential analysis, while Figure 3.2b presents the vegetation-filtered environment and is employed for visibility assessment. Removing trees from the DSM is preferred in the visibility assessment because in winter the defoliated trees can be deemed as highly transparent. In fact, the visibility assessment is preferred to be done on a worst-case scenario. In other words, by employing the most open interpretation of the terrain, one can more accurately determine whether the PV system is visible or not. This approach ensures a more stringent analysis, reducing the possibility of overestimating the energy potential and underestimating the visibility of the PV system. An alternative is to perform visibility assessments directly on LiDAR point cloud when vegetation is expected to be included. This approach is not adopted in the current project due to hardware and software limitations. Zhang et al. demonstrated such a workflow by using the detailed representation of vegetation from LiDAR, achieving better analysis quality at the cost of significantly increased computational demand [95].

The last input required for the tool is the building footprints which can be obtained from the cadastral data of Basisregistratie Adressen en Gebouwen (BAG) [96]. It consists of geo-referenced polygons, each corresponding to a registered household in the Netherlands. This dataset serves as a bounding box to pull out the building points for visibility and PV potential analysis. This procedure is country-independent but is obviously thought for and applicable to the Netherlands, as it is enabled by the digital data readily and publicly available for the country. In the case of other locations, more effort should be put by public and private stakeholders to also readily and publicly provide digital data to support a quicker implementation of photovoltaic technology in the urban environment.

3.2.2. Roof plane detection and extraction

The input data need to be processed to identify the roof surfaces as well as determine their tilt and azimuth angles. The algorithm to realize this step has been extensively discussed in the work carried out by J. Azanza [97]. Here, some modifications are introduced to improve its accuracy and computational speed. Figure 3.3 presents the modified steps to detect and extract the roof points. The starting point involves pulling out the building point cloud from the DSM using the building footprint as a clipping mask. Then, the roof points are segmented into distinct clusters based on their spatial distribution [98], where two neighbouring points are grouped into the same cluster if their Euclidean distance is lower than a threshold or the angle between the LiDAR sensor and these two points is greater than a set value. This is exampled in Figure 3.3a in which the red and blue points represent two different clusters. After that, the normal vector of each

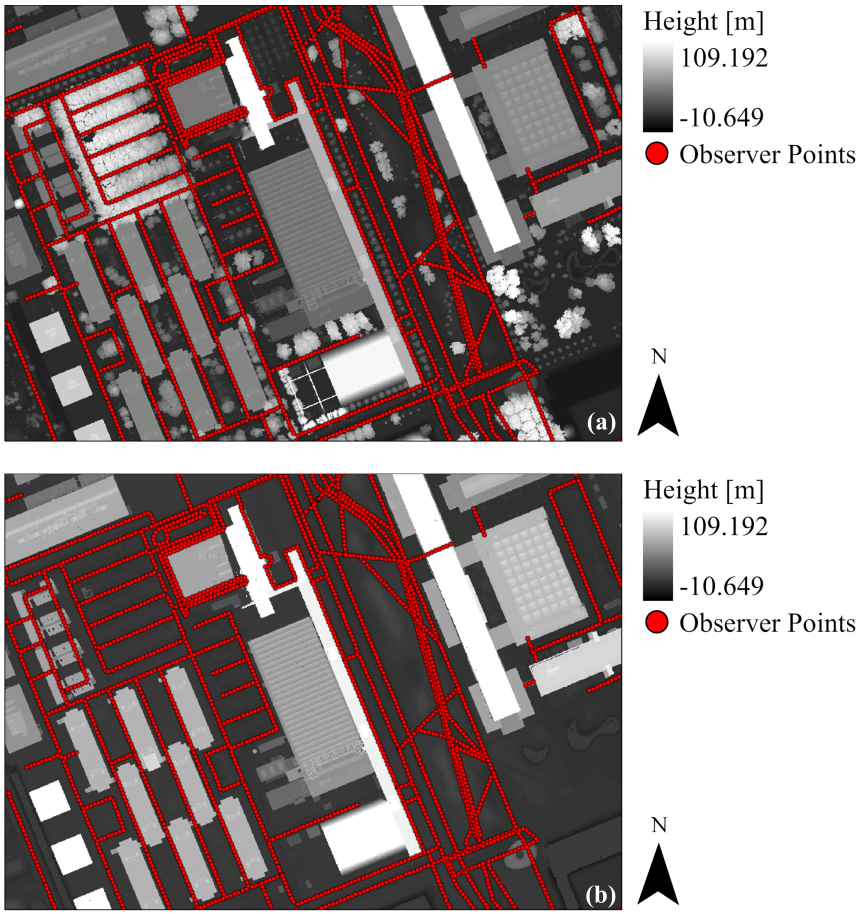

Figure 3.2: DSMs of a section of the TUD campus, featuring the mapped public domain as red points: a) trees included; b) trees removed.

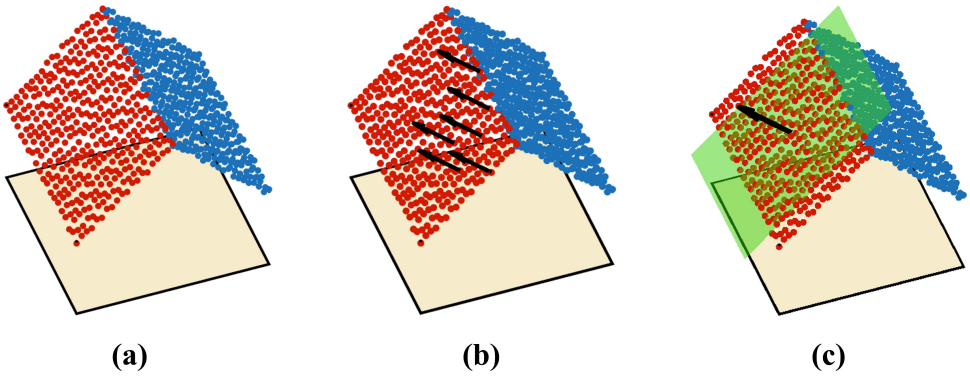

Figure 3.3: Steps for roof detection and extraction: a) The roof points are extracted with the building footprint and segmented into red and blue clusters; b) For each cluster, the normal vector of each roof point is calculated and grouped into bins; c) Finally, the roof plane is fitted using the normal vectors obtained in the previous step as reference vectors. The normal vector that results in the best outcome is assigned to all the points belonging to the plane and further used for tilt and azimuth determination.

roof point is calculated and allocated to different bins considering the smallest polar angle difference. These bins essentially contain various combinations of tilt and azimuth angles, where tilt angles vary from 5 to 85 degrees in 10-degree increments, and azimuth angles are separated by 15-degree intervals, starting from 7.5 degrees and ending at 352.5 degrees. Based on the frequency count for each bin, they are sorted in descending order to identify the most frequently occurring orientation of the roof surface. The normal vector corresponding to the bin with the highest frequency count is selected as the primary reference vector for plane fitting [99]. If the remaining number of points is greater than 1% of all the roof points within the cluster, the normal vector of the bin with the second highest frequency count is passed in as the reference vector. This process is iterated until there are insufficient roof points (less than 1%) remaining to fit a plane. Finally, the normal vector of the fitted plane (colored in green) is determined as shown in Figure 3.3c, with which the tilt and azimuth angles are calculated and assigned to all the points found on the plane. By identifying the most frequently occurring roof orientations and using them as reference vectors for plane fitting, the modified algorithm manages to prioritize the reference vector selection, which enhances the computational speed and accuracy of the plane fitting process.

3.2.3. Roof surface visibility assessment and optimization

Prior to proceeding with the visibility assessment, a couple of assumptions need to be established given the limitation of data input. LiDAR data do not provide information on material properties or surface textures. Even though coupling the LiDAR data with surface context information is possible by means of satellite and street-view images [100], algorithmic processing of this information to obtain quantitative visibility results that are aligned with mathematical psychology is deemed infeasible within the scope of this study due to its complexity. Another limitation lies in the fact that roads are not perfectly

represented by lines, as the latter do not account for the width of the roads, which can affect the final visibility results. Unfortunately, a suitable data source that provides such information on a large scale could not be found. Meanwhile, the social value of the observer points located at different zones of the urban area can also influence the visibility result, as human traffic is expected to be heavier around places with more social value, such as tourist attractions, compared to residential neighborhoods. Therefore, based on these limitations in data availability and implementation practicality, the following assumptions are made for the visibility assessment:

- The material coherency, geometric coherency and modular pattern coherency for a rooftop PV system are not included in this algorithm.
- The observer points are generated based on the line-representation of road networks with various spacings.
- Each observer is assumed to have equal social value in the public domain, meaning that there is no weight assigned to the observer points.
- The PV installations must adopt the tilt of the roof surface, regardless of flat or slanted roofs [101].

Binary visibility

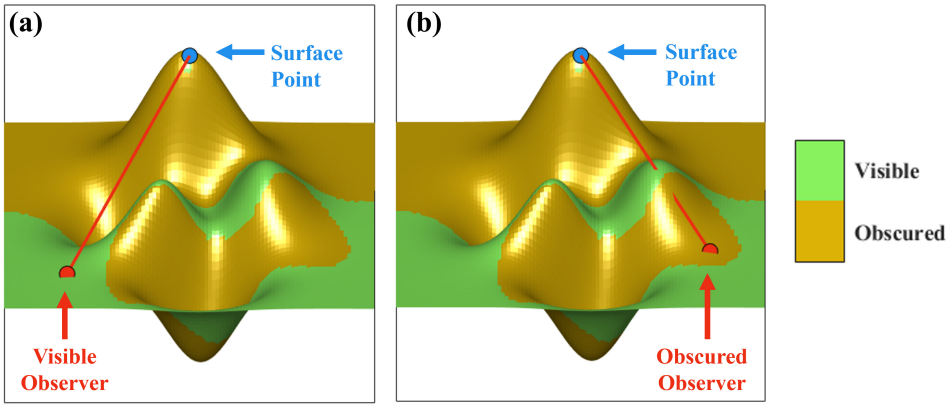

Figure 3.4: Line-of-sight assessment for binary visibility assessment: a) the line of sight is not blocked by the terrain or any artifacts and the observer is visible to the surface point; b) the line of sight is obscured by the terrain and the observer point is invisible to the surface point [102].

By definition, if a photon reflected or originated from any object manages to enter a human's eye and evoke a visual perception in the brain, this object is deemed as visible. Therefore, to perceive an object, it is imperative to have an unobstructed line of sight between the eyes and the object. Based on this feature, it is possible to identify invisible roof surfaces by performing a line-of-sight (LOS) assessment between the roof surface cells and observers [102]. Figure 3.4 demonstrates the binary visibility results obtained

from the proposed algorithm for the evaluation of visibility between observers and roof surface cells. The sub-figures depict two different observer points situated at different locations on the terrain, while the terrain and surface point remain consistent. The LOS assessment establishes a line between the surface point and the observer, subsequently calculating the angle formed between the observer and each of the points that are interpolated along the line. If there exists any angle larger than the one formed between the surface point and the observer, the binary visibility between these two points is marked as invisible. For the case in Figure 3.4a, the observer is visible to the surface point, while in Figure 3.4b, the observer is invisible to the surface point. In the mathematical definition, the binary visibility V_b between a pair of surface cell and observer point can be simply written as:

$$V_b = \begin{cases} 0, & \text{Obstructed LOS} \\ 1, & \text{Unobstructed LOS} \end{cases} \tag{3.1}$$

By performing the LOS assessment between the roof cells and their respective observer points, the frequency with which the roof cell is visible from the public domain can be computed. Additionally, this analysis allows for the determination of the length of the public domain, which is essentially the product of the number of visible observers and the spacing between them. These insights are useful for identifying the low-hanging fruits for PV system installation, as they can reveal invisible areas that are free from regulatory restrictions. Furthermore, they provide an indication of the magnitude of the public domain that is visually impacted by PV modules.

Solid angle and visual amplitude

The detection of photons coming from an object is necessary but not sufficient to guarantee a successful perception. Failure to complete the visual task by evoking a visual perception in the human brain, even with the presence of detected photons, renders the object invisible. A way to incorporate this effect is through calculating the amount of field of view this object subtends to the observer, in other words, the solid angle as illustrated in Figure 3.5 [85]. It is defined as the surface's projection area A_p onto a sphere centered at the observer, divided by the square of the sphere's radius:

$$\Omega = \frac{A_p}{r^2}, \quad A_p \in [0, 2\pi] \tag{3.2}$$

The projection area A_p ranges from 0 to 2π, where the latter corresponds to an observer standing directly on the planar surface, resulting in a hemispherical projection. In this work, an analytical solution is applied, which calculates the solid angle that a triangular surface subtends to an observer point [104]. To compute the solid angle of a square roof cell, this algorithm divides the cell into two triangles and calculates their individual solid angle separately before adding them together. This process is visually described in Figure 3.6 and accomplished with the equations 3.3 and 3.4.

$$\begin{aligned} \tan(\frac{\Omega_1}{2}) &= \frac{|\mathbf{abc}|}{abc + (\mathbf{a}\cdot\mathbf{b})c + (\mathbf{a}\cdot\mathbf{c})b + (\mathbf{b}\cdot\mathbf{c})a} \\ \tan(\frac{\Omega_2}{2}) &= \frac{|\mathbf{adc}|}{adc + (\mathbf{a}\cdot\mathbf{d})c + (\mathbf{a}\cdot\mathbf{c})d + (\mathbf{d}\cdot\mathbf{c})a} \end{aligned} \tag{3.3}$$

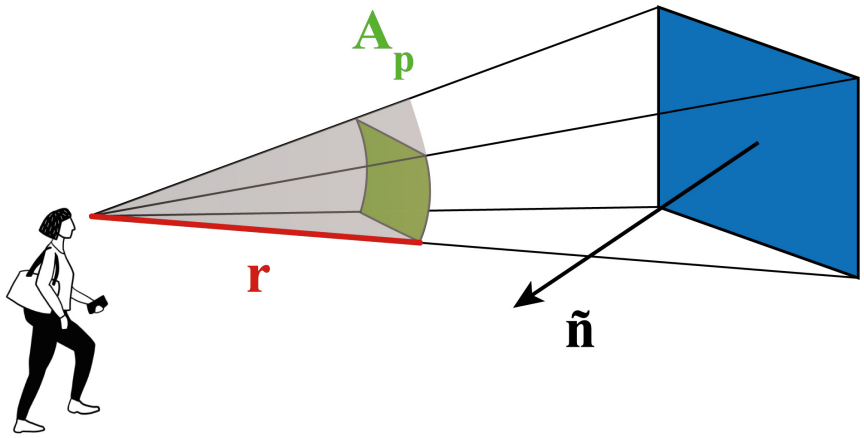

Figure 3.5: Depiction of solid angle subtended by a planar surface as viewed by a person centered at the gazing field with a radius of r, where ñ is the normal vector of the planar surface, and A_p is the projected area of the planar surface on the gazing sphere [103].

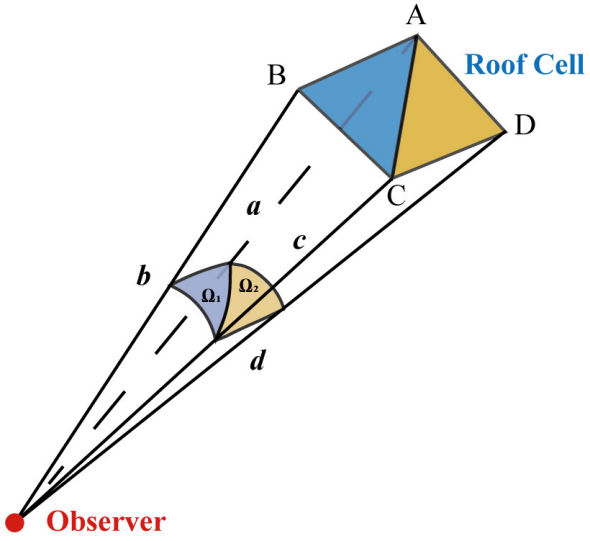

Figure 3.6: The surface cell is divided into two triangles whose solid angles Ω_1 and Ω_2 are calculated separately and summed up to determine the solid angle of the surface cell.

where Ω_1 and Ω_2 define the solid angles of the triangles ABC and ADC; $\boldsymbol{a}$, $\boldsymbol{b}$, $\boldsymbol{c}$ and $\boldsymbol{d}$ are the vectors connecting the corner points A, B, C, and D to the observer point; a, b, c, and d are the distances between the observer point, and the respective corner points A, B, C, and D; $|\boldsymbol{abc}|$ is the determinant of matrix. The total solid angle of the surface cell is calculated as:

$$\Omega = |\Omega_1| + |\Omega_2| \tag{3.4}$$

where Ω is expressed in units of steradians (sr). It should be noted that the inverse tangent function $atan2$ is used in equation 3.3 to keep the calculated solid angle within the range of $[0,\pi]$ [105].

To determine the vectors for the algorithm, the coordinates of the corner points of each visible roof cell are first generated. Figure 3.7 shows a raster-based environment in which two points are depicted. The red point is the observer point, and the blue point represents the center of the visible roof cell. Given the raster resolution of R, the vectors can be found as per:

$$\boldsymbol{a} = \begin{bmatrix} x \\ y \\ z \end{bmatrix} = \begin{bmatrix} X_{cell} - X_{obs} - \frac{R}{2} \\ Y_{cell} - Y_{obs} + \frac{R}{2} \\ z_a - Z_{obs} \end{bmatrix} \tag{3.5}$$

$$\boldsymbol{b} = \begin{bmatrix} x \\ y \\ z \end{bmatrix} = \begin{bmatrix} X_{cell} - X_{obs} - \frac{R}{2} \\ Y_{cell} - Y_{obs} - \frac{R}{2} \\ z_b - Z_{obs} \end{bmatrix} \tag{3.6}$$

$$\boldsymbol{c} = \begin{bmatrix} x \\ y \\ z \end{bmatrix} = \begin{bmatrix} X_{cell} - X_{obs} + \frac{R}{2} \\ Y_{cell} - Y_{obs} - \frac{R}{2} \\ z_c - Z_{obs} \end{bmatrix} \tag{3.7}$$

$$\boldsymbol{d} = \begin{bmatrix} x \\ y \\ z \end{bmatrix} = \begin{bmatrix} X_{cell} - X_{obs} + \frac{R}{2} \\ Y_{cell} - Y_{obs} + \frac{R}{2} \\ z_d - Z_{obs} \end{bmatrix} \tag{3.8}$$

The x and y components of the vectors can be readily obtained, as both the raster resolution and the x, y coordinates of the roof cells and the observer points are known. The latter essentially represent the projection of the corner points at the x-y plane. To find the $z_{a,b,c,d}$ component of the corner points, a vertical line is assumed to be extending from the projection and intersecting the roof surface. This simplifies the problem to determining the precise intersection between a line and a plane. A general illustration of this solution, including the interplay between the geometrical elements, is depicted in Figure 3.8, and further detailed in Equations 3.9 and 3.10:

$$z_{a,b,c,d} = b_3 + v_3 \cdot t \tag{3.9}$$

where

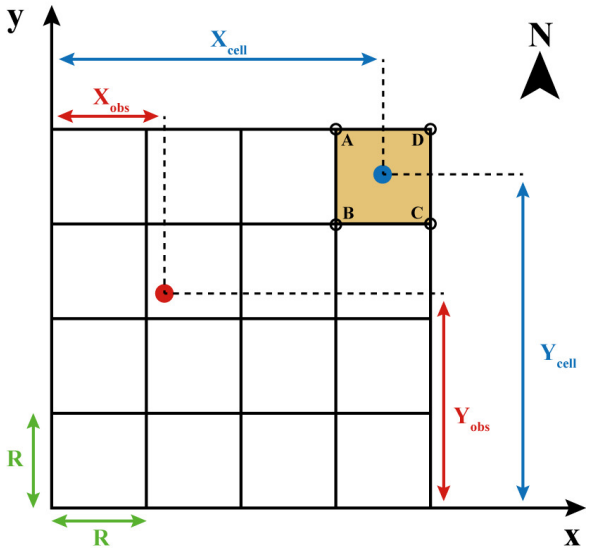

Figure 3.7: The calculation of the Euclidean distance between the observer point and the four corners of the surface cell in a raster-based representation of the environment, where the red point is the observer point, and the blue point is the center of the surface cell.

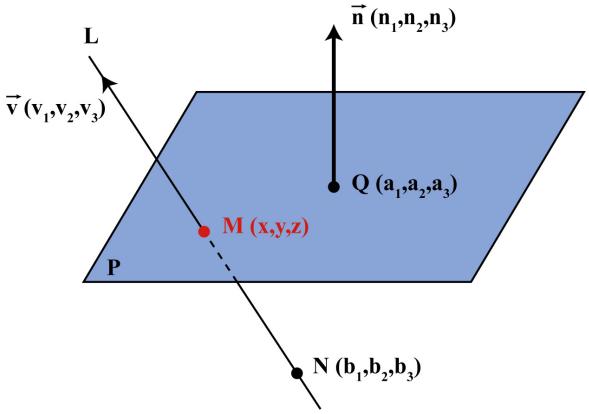

Figure 3.8: Illustration of finding the intersection between a line and a plane. Point Q lies on the plane defined with the normal vector $\vec{n}$. N is an arbitrary point outside the plane, defining line L with direction vector $\vec{v}$. M is the intersection point between line L and the plane P.

$$t = \frac{(a_1 - b_1) \cdot n_1 + (a_2 - b_2) \cdot n_2 + (a_3 - b_3) \cdot n_3}{n_1 \cdot v_1 + n_2 \cdot v_2 + n_3 \cdot v_3} \tag{3.10}$$

In the context of finding the z components of the corner points, point Q in Figure 3.8 represents a point on the roof surface, with its corresponding normal vector denoted by $\vec{n}$. Point N corresponds to the projection of the corner point on the x-y plane, while the direction vector $\vec{v}$ remains fixed as [0,0,1]. Therefore, equation 3.9 can be rewritten as:

$$z_{a,b,c,d} = t_{a,b,c,d} \tag{3.11}$$

The Euclidean length of vectors can be calculated by computing their magnitude.

To give a better insight into the amount of field of view a roof cell takes up for the average observer inside the visible public domain, the average solid angle is proposed. It is given in the equation 3.12, assuming equal weight for all the observer points. The solid angles (Ω_v) for a roof cell are calculated for each visible observer, added up, and the summation is subsequently divided by the number of visible observers n_v.

$$\overline{\Omega_v} = \frac{\sum_{v=1}^{n_v} \Omega_v}{n_v} \tag{3.12}$$

To incorporate the visual threshold used in psychophysics, visual amplitude (VA) is introduced [81, 89]. It is defined as a base-ten logarithm as shown in equation 3.13:

$$VA = \log_{10} \sqrt{\frac{\overline{\Omega}}{\Omega_0}} \tag{3.13}$$

where $\overline{\Omega}$ is the average solid angle of the roof cell seen by n_v observers, and Ω_0 is the minimum angle of resolution presented in steradians. The latter is highly dependent on visual contrast, which refers to the difference in appearance between two objects due to their color, material, and texture variations [106]. It determines the saliency of the target roof cell; in other words, it affects how easily the roof cell can be distinguished from the surroundings if this roof cell was to be covered by PV material. A significant variation in the material properties between PV and roof surface means a greater likelihood for the PV to be perceived given the same visual angle that subtends to the observers. This distinction creates a huge visual contrast, leading to a low minimum angle of resolution. Conversely, when the material properties of PV and the roof surface resemble, the visual contrast decreases and the minimum angle of resolution can be set larger. This adjustment brings down the VA given the same geometrical parameters. Consequently, the roof cell that was previously classified to the high-visibility group, may now be assessed as having medium or low visibility. However, accurately modeling the visual contrast of roof cells poses a significant challenge due to the lack of detailed material data, which can result in large uncertainties in the modeling process. To address this limitation, a fixed minimum angle of resolution of 1 square minute of arc, equivalent to 8.46×10^{-8} [sr], is used in this project. This threshold corresponds to the scenario of a standard observer in conditions of infinite luminance contrast, which is aligned with the worst-case-scenario visibility assessment approach, ensuring that the visibility is not underestimated. This threshold can be adjusted if the material in the context is provided [106].

For a planar surface, the VA ranges from minus infinite to 3.94 where the lower and upper limits can be found in the cases when the surface is infinitesimal, and the surface creates a hemispherical projection of 2π [sr], respectively. Figure 3.9 lists some visual thresholds determined experimentally by assessing the visual response of different groups of volunteers [107]. Three visibility groups are classified where a surface with a visual amplitude lower than zero is classified as having low visibility and can be barely detected by most healthy individuals; a surface with a visual amplitude between 0 and 1.4 is considered as medium visibility and can be perceived by the majority of people; surfaces with a visual amplitude falling within the higher end of the scale are classified as highly visible and are typically perceivable by everyone except those with visual impairments. These categories are adopted in this project to classify the visibility of the roof surface cell, assisting in better understanding and quantifying the visual impact.

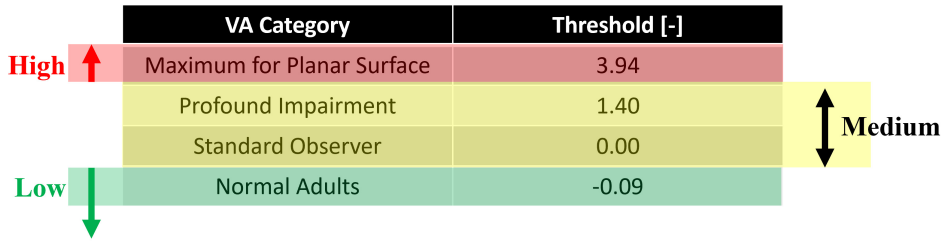

Figure 3.9: Categorization of the VAs based on the thresholds determined experimentally by assessing the visual response of different groups of volunteers. Three groups are classified, indicating a low, medium, and high visual impact [107].

Optimization

Performing many LOS assessments is time-consuming, and it is found to be the primary bottleneck of this algorithm regarding computational speed. Several approaches are adopted to make this algorithm more computationally efficient, including task allocation optimization, unnecessary LOS elimination, and adaptive observer selection. Additionally, the assessment range was increased and the observer spacing was reduced incrementally to further enhance the efficiency of the algorithm while maintaining its accuracy.

The most straightforward way to reduce computational burden is by using parallel computing [108]. Parallel computing allows for the allocation of tasks among multiple cores and processes them simultaneously. Therefore, it optimizes efficiency by harnessing the collective power of multiple processing units, but its performance is ultimately limited by the physical constraints of the computer hardware. In this project, the simulations were performed on a laptop with an Intel(R) i7-8750H CPU (6-core) running at a base frequency of 2.2 GHz and 16 GB of DDR4 RAM.

The second approach used for speed improvement is by eliminating the observers that are lying behind the roof surface, considering the fact that the roof surface is only visible to the hemisphere that it is facing. This process is realized with Equations 3.14, 3.15, 3.16 and illustrated in Figure 3.10.

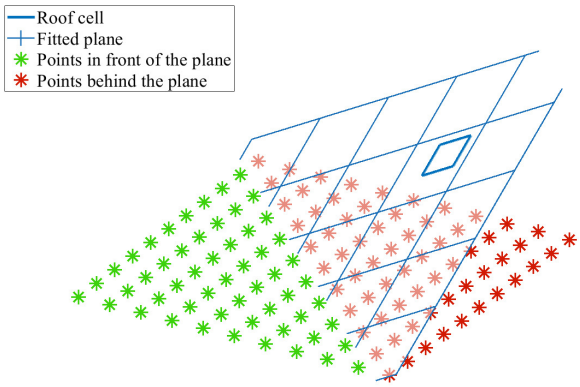

Figure 3.10: Visual depiction of hemisphere filter of a roof plane with a 135° azimuth and 45° tilt. The green points are in front of the roof plane which potentially can be visible; red points are behind the roof plane, and they are eliminated from LOS assessment.

$$\frac{dz}{dx} = tan(\theta)sin(\alpha) \tag{3.14}$$

$$\frac{dz}{dy} = tan(\theta)cos(\alpha) \tag{3.15}$$

$$z_{obs} > z_{cell} - \frac{dz}{dx}(x_{obs} - x_{cell}) - \frac{dz}{dy}(y_{obs} - y_{cell}) \tag{3.16}$$

where θ is roof tilt and α is the roof azimuth. If this condition is satisfied, the observer point is identified to be in front of the roof surface and a LOS assessment is performed. For a flat surface that is lying above the observer height, this observer filter eliminates all the observer points, drastically reducing the computational time without impacting the final results. Additional refinement to the filter is required if the PV module is mounted with a specific tilt on the flat roof. In such cases, PV modules close to the roof edge may still be visible from the public domain.

The third technique employed to reduce computation time is adaptive observer selection as illustrated in Figure 3.11. LOS assessment evaluates the binary visibility between the point of interest and the public domain by constructing multiple lines connecting them. This process can be executed either based on the roof cell or the observer point. By adaptively selecting the assessment target between the roof cell and observer points, depending on which one has fewer points, the number of iterations is decreased. Consequently, this approach minimizes computational time by reducing the number of LOS assessments required.

To achieve an optimal balance between the accuracy of the visibility results and the computational time, it is important to select an appropriate assessment range. Both binary visibility and visual amplitude results are influenced by changes in the assessment

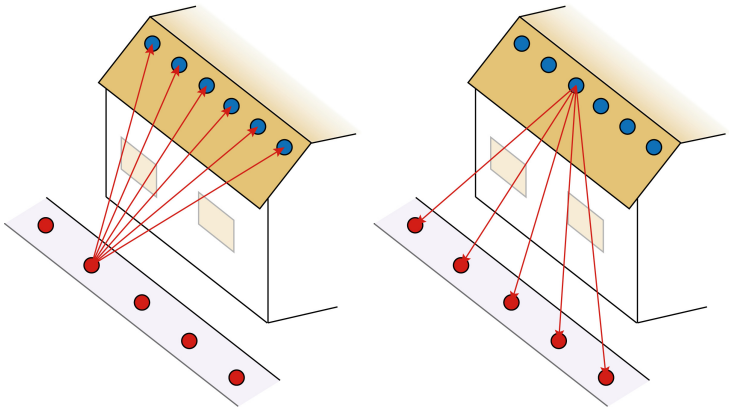

Figure 3.11: Visual depiction of the adaptive observer selection method. The LOS can either be performed from a) the observer point or b) the roof cell, depending on which group has fewer points.

range. Generally, increasing the assessment range results in a larger public domain, potentially leading to the identification of new visible roof surface cells. However, a convergence point will be reached, beyond which further increases in the assessment range yield no significant changes in visibility outcomes. Figure 3.12 visualizes the method for determining the optimal assessment range. The algorithm operates on a roof-specific basis, meaning that the optimal assessment range is found for the entire roof surface rather than one single roof cell. This is achieved by calculating the total binary visibility n_s (the total number of visible roof cells) and the average VA of the roof surface within the assessment radius according to Equations 3.13 and 3.17.

$$\overline{\Omega} = \frac{\sum \overline{\Omega}_{cell}}{n_s} \tag{3.17}$$

where $\overline{\Omega}_{cell}$ is the average solid angle of each visible roof cell defined by Equation 3.12. While executing, the algorithm incrementally increases the assessment range (by 20 m) and calculates the change induced by the inclusion of new observer points. If the difference between the results for both n_s and VA_{avg} after n^{th} and $(n-4)^{th}$ increments is less than 5%, the algorithm terminates, and the optimal assessment range for the specific roof surface is determined. A minimum assessment radius of 100 m is set as default. Roof surfaces that are generally visible to distant observers will automatically be assessed for extended ranges. Conversely, roof surfaces that are visible only to nearby observers will stop further examination. With this approach, the assessment process for each roof surface is tailored, optimizing between both accuracy and computational efficiency.

Besides, another optimization process is conducted on the observer spacing, as it can also influence the visibility results. Given the assessment range determined from the previous step, the observer spacing is halved with each iteration, as illustrated in Figure 3.13. The n_s and VA_{avg} of the roof surface are computed for the newly included observer points, and the results are cumulatively added to the previous iteration. If the difference

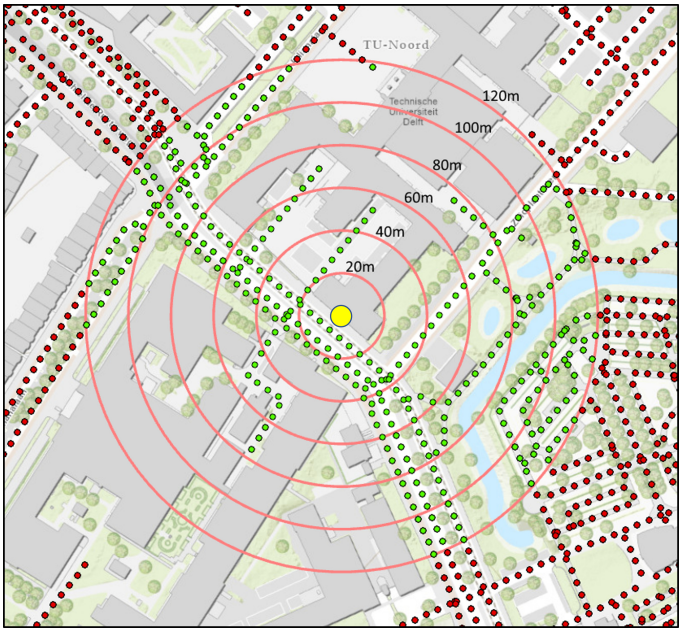

Figure 3.12: Visual depiction of the determination of the assessment range for each roof surface, with an incremental step of 20 meters. The yellow point represents a roof surface cell. The green points are the observer points within the assessment range, while the red points are not falling within the assessment range.

between adjacent iterations is lower than 5%, the observer spacing is determined. In this project, the maximum observer spacing is set to 600 cm.

PV module positioning, yield estimation, and visibility assessment

In the multi-criteria decision-making process for roof PV planning, visibility constitutes only one aspect. As the primary purpose of installing PV modules is solar energy harvesting, evaluating the PV potential of roof-mounted PV systems serves as a vital piece of the puzzle to achieve a comprehensive understanding before concluding the roof PV planning. In this work, the PV potential analysis is conducted using the in-house developed workflow [15, 39, 59]. This workflow fits the PV modules to the detected roof surface and calculates its annual AC yield considering the complex skyline where the PV module is located within [109]. An economic threshold of 650 kWh/kWp is selected to exclude the PV modules whose installation is not economically viable, ensuring that only feasible options are considered in this analysis [15]. Meanwhile, for each fitted PV module, the visibility is evaluated by generating a 2 by 2 grid on the PV module surface; thus, each point represents a quarter of the module surface area. These module surface points are used to first perform the PV potential calculation, followed by LOS analysis and VA calculation considering the previously established roof-specific assessment range and observer spacing. The final VA for each module is determined by averaging the sum of the four fractions, and further categorized based on Figure 3.9. In general, a denser grid results in a more accurate visibility map for the PV module, but this increased accuracy

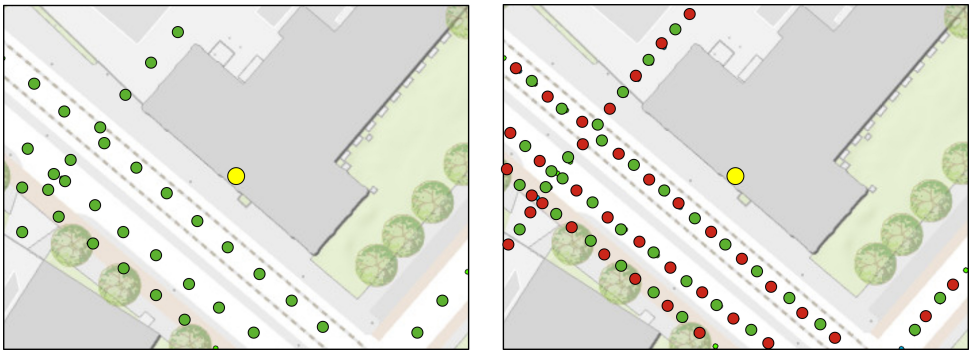

Figure 3.13: Visual depiction of the determination of the optimal observer spacing for each roof surface. The yellow point represents a roof surface cell. The left figure shows the green observer points with spacing S, and the right figure halves the observer spacing by adding red observer points.

comes at the expense of computational time. Eventually, the simulated AC yield for PV modules in each VA category is reported, providing useful insights for rooftop PV planning from both economic and social perspectives.

3.3. Results and Discussion

In this section, the outputs from the visibility assessment tool for multi-criteria urban roof planning are presented. This includes the results for roof detection and extraction, roof binary visibility map, roof VA map, roof PV module layout, roof PV AC yield map, and roof PV visibility map. The computational speed for each step of the workflow is also presented. To better demonstrate the workflow in a consistent manner, the building of EEMCS faculty on the TU Delft campus is selected as a study case. An aerial image of this building can be seen in Figure 3.14.

3.3.1. Roof detection and extraction

The outcomes of the roof detection and extraction algorithm applied to the building of EEMCS faculty are demonstrated in Figure 3.15. The initial point cloud of the building, obtained from cropping the DSM using the building footprint, is illustrated in Figure 3.15a. Subsequently, the extracted roof planes are depicted in Figure 3.15b, with each roof plane assigned a unique color for differentiation. The minimum area for a roof plane to be registered is set to be 10 m^2, which corresponds to a requirement of more than forty points for the identified roof plane. The majority of building points that are excluded due to this threshold are found to be rooftop artifacts or curved edges characterized by distinct normal vectors. Therefore, this exclusion has very little impact on the final results.

3.3.2. Roof binary visibility and VA maps

The binary visibility result is depicted in Figure 3.16, which is essentially a binary map in which the yellow points correspond to visible roof cells and purple points denote invisible roof cells. As expected, flat roof surfaces remain obscured from the public domain.

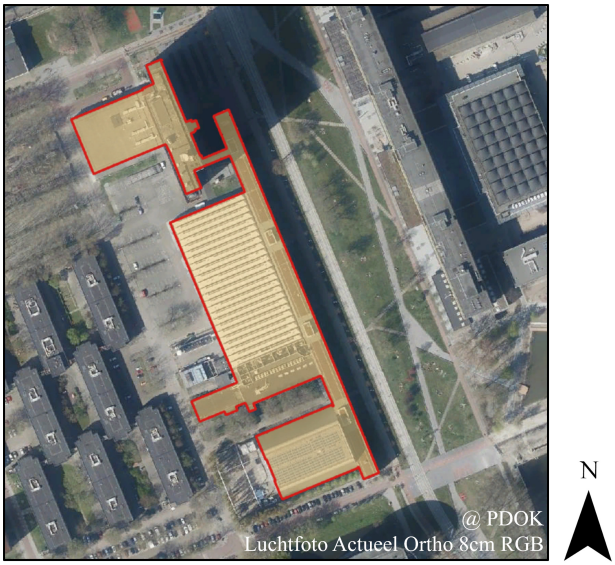

Figure 3.14: Orthogonal aerial image of the building of EEMCS faculty, which is highlighted with its footprint in yellow [110].

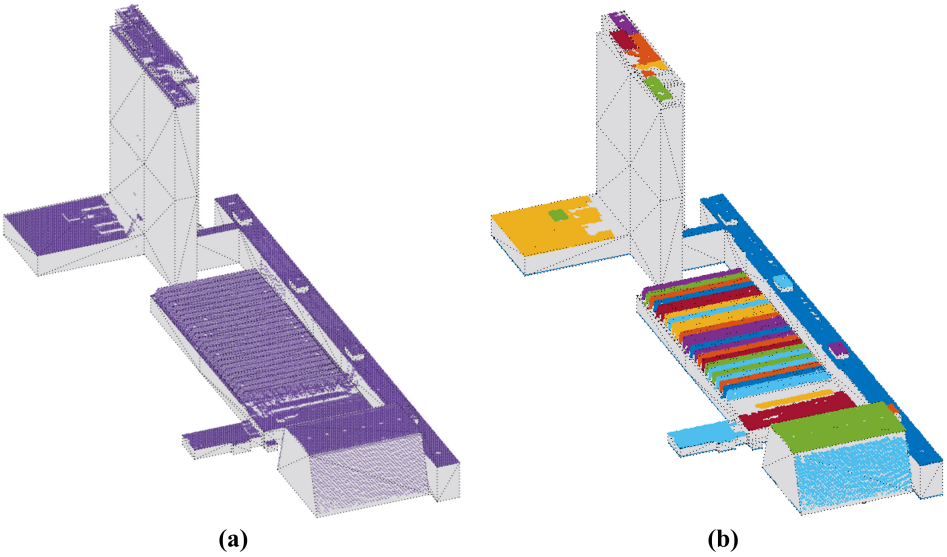

Figure 3.15: Roof detection and extraction from the point cloud of the building of EEMCS faculty, where a) the unclustered original point cloud is shown; b) the detected and extracted roof planes are displayed, and each roof is represented by a different color.

The analysis reveals two distinct visible sections: the first one is located at the saw-tooth-shaped roofs, with a corresponding Google Street View image displayed aside. The west part of this roof section sees the streets, leading to the majority of the western roof cells being visible. The other section includes the southern roof of the ESP lab, which also directly faces the streets, as evidenced by the corresponding Google Street View image. Although trees are present at the lower region of the roof, the visibility analysis was conducted using a DSM in which vegetation has been removed as introduced in section 3.2.1, leading to an unobstructed LOS between the roof cells and the observer points.

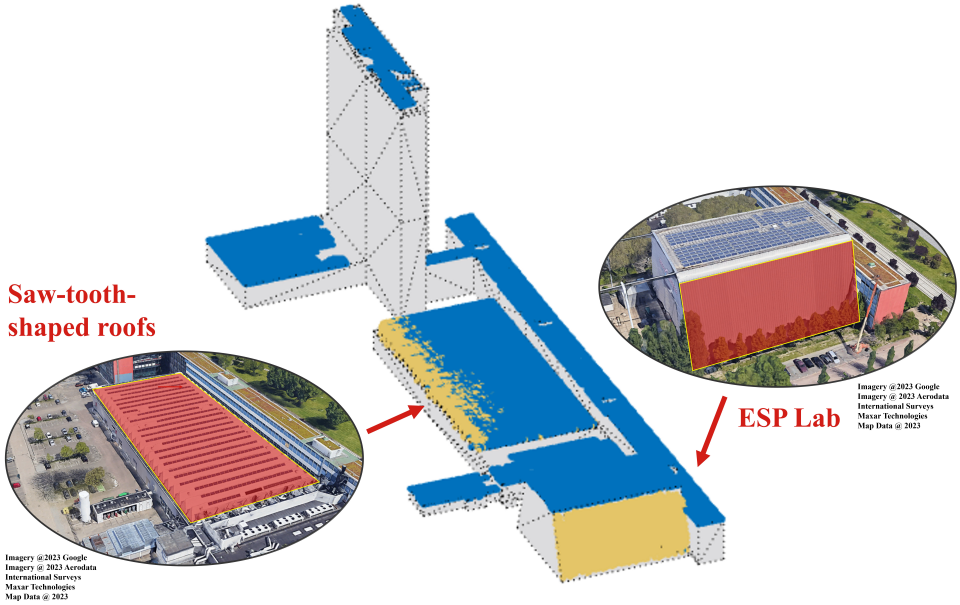

Figure 3.16: The binary visibility map for the building of EEMCS faculty, where the visible roof cells are in yellow and the invisible roof cells are in blue.

Figure 3.17 shows the normalized visual amplitude (nVA) result for the building of EEMCS faculty. It is calculated by dividing the VA by the maximum solid angle of a planar surface (3.94 sr). As the VA is solely calculated for the visible roof cells, the non-zero VA results are primarily distributed across the saw-tooth-shaped roofs and the southern roof of the ESP lab. The color scale indicates higher nVA values using lighter colors, illustrating that the west edge of the saw-tooth-shaped roofs exhibits a compatible visual impact on the public domain, predominately falling within the low to medium visibility range. Variations in this section are not significant due to the similarity in both their distance and the viewing angle relative to the public domain, meaning that the subtended solid angles are closely aligned. By contrast, the southern roof of the ESP lab demonstrates high visibility due to its shorter distance between the roof and the public domain. Additionally, a descending trend in visibility is observed from the bottom to the top edge of the roof. This can be mainly attributed to the distance and the viewing angle, which dictate the solid angle of the roof surface cell subtending to the observers. Consider-

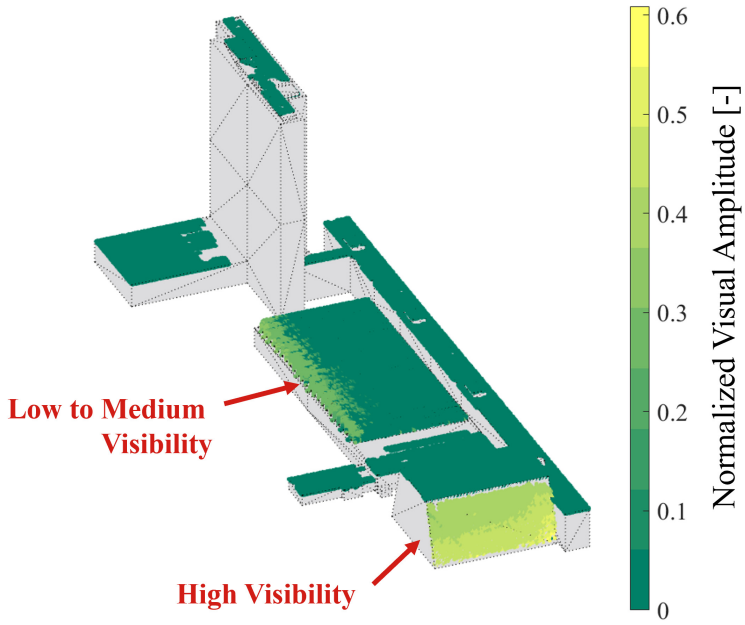

Figure 3.17: Normalized VA map for the building of EEMCS faculty. The lighter the color, the higher the visibility of the roof cell.

ing the average eye height (1.7 m) of the observers, the bottom of the roof has a shorter distance as well as a smaller viewing angle relative to the observer points, resulting in a higher nVA.

3.3.3. Roof module placement and AC yield map

The roof PV module placement result is shown in Figure 3.18a, and the corresponding AC yield map for all the fitted PV modules is displayed in Figure 3.18b. PV modules installed on slanted roofs adopt the tilt and orientation properties of the roof, while those placed on flat roofs are configured to align with the longest edge and set to have a zero-degree tilt in compliance with local regulations as introduced in Section 3.2.3. Besides, this process uses the non-filtered DSM to account for potential shading effects caused by the surrounding urban environment, such as the trees in front of the roof of the ESP lab. For economic feasibility, modules with a simulated specific yield of less than 650 kWh/kW$_p$ are excluded.

3.3.4. Roof PV visibility map

To categorize the visibility of the fitted PV modules, the VA of each module is calculated and the result is presented in Figure 3.19. Instead of using numerical categorization, the visibility of the PV modules is divided into low, medium and high visibility groups, using the standard classification introduced in Figure 3.9. It is evident from the figure that all the PV modules on flat roofs have low visibility, signifying that most of the individuals

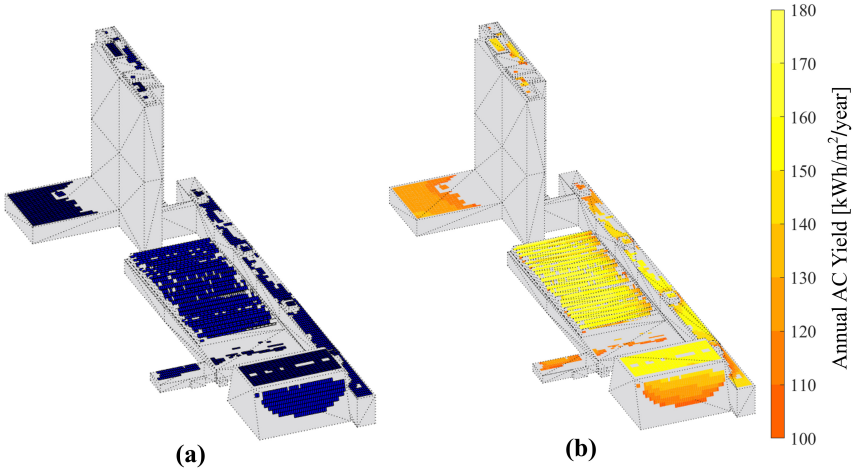

Figure 3.18: a) PV module fitting results where the modules that failed in passing the economic threshold are excluded; b) The AC yield map of all fitted PV modules.

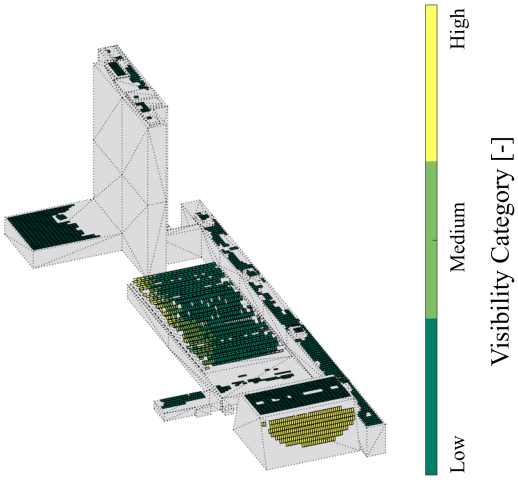

Figure 3.19: Visibility categories of all fitted PV modules, where three categories are identified, namely low, medium and high visibility.

moving in the public domain cannot perceive them. PV modules installed on the southern roof of the ESP lab exhibit high visibility, indicating that they are typically perceivable by everyone except those with visual impairments. As for the PV modules mounted on the saw-tooth-shaped roofs, their visibility ranges from high to low visibility, depending on their placement location. Generally, PV modules situated close to the west edge have higher visibility, which reduces gradually as they approach the east edge, eventually becoming completely invisible. Compared to the visibility results of roof surface cells in the same location, PV modules feature a larger area so that the solid angle subtending to the observers is more substantial, leading to an increased VA, namely a higher visibility.

To gain more insights into multi-criteria decision-making for urban roof PV planning, the annual AC yield of the PV modules from each visibility category is calculated, with the results shown in Table 3.1. The same workflow has been applied to the rest of the monumental buildings on the TU Delft campus (see Figure 3.20), and the results are listed in Table 3.2. It turned out that approximately 2.7 GWh annual AC yield can be expected from the PV modules that are imperceivable from the public domain, which accounts for 77% of the total potential on such monumental buildings. All the results are visualized and published as a web scene, with its screenshot shown in Figure 3.21.

Table 3.1: Annual AC yield results of the PV modules from different visibility categories for the building of EEMCS faculty.

Visibility [-]	Annual AC Yield [MWh/year]
Low	676.6
Medium	52.3
High	86.9

According to the local regulation in the city of Delft, a PV system can be installed on monumental buildings without permits as long as the installed PV systems are barely visible or invisible from the public domain [101]. This simulation framework serves as a guideline for the decision-makers to identify these low-hanging fruits and helps streamline the initiation and execution processes of PV projects. Meanwhile, the regulation also emphasizes that installing PV systems on flat roof surfaces is preferred over placing them on tilted ones. Identifying the flat roof surfaces is one of the intermediate results from this simulation framework, thereby assisting in further expanding the selection of preferred installation sites. Even for the roof surfaces with some degree of visibility, this workflow can still provide valuable information on their location and PV potential, setting the stage for any potential subsequent on-site visibility assessments.

3.3.5. Computation speed

The computation speed of each step of the workflow applied to all the monumental buildings on the TU Delft campus is shown in Table 3.3. In most cases, the majority of time is spent in determining the optimal assessment range and observer spacing, primarily due to the time-consuming nature of LOS assessment. For buildings B4, B7, B9, and B12, the visibility assessment steps take virtually no time, as these buildings only have flat roofs and do not require LOS analysis. On average, the workflow takes 0.12 s/m^2, with the maximum and minimum values being 0.27 and 0.04 s/m^2, respectively.

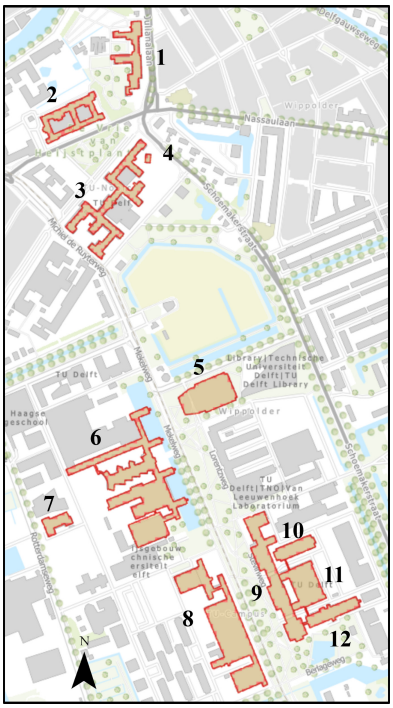

Figure 3.20: The footprints of monumental buildings on TUD campus [111].

Table 3.2: Annual AC yield results of the PV modules from different visibility categories for all the monumental buildings on the TU Delft campus. The building number is in agreement with the numbering in Figure 3.20.

Building [-]	Low Visibility [MWh/year]	Medium Visibility [MWh/year]	High Visibility [MWh/year]
B1	55.0	52.7	38.2
B2	57.5	23.3	57.3
B3	152.5	89.5	156.9
B4	15.7	0.0	0.0
B5	99.7	49.4	20.7
B6	788.7	78.2	11.1
B7	48.6	0.0	0.0
B8	676.6	52.3	86.9
B9	343.1	0.0	0.0
B10	74.4	72.7	0.0
B11	105.0	5.4	0.0
B12	262.2	0.0	0.0
Total	2679.0	423.5	371.1

Table 3.3: The computational time of each step of the workflow for all the monumental buildings on TUD campus.

Building [-]	Area [m^2]	Roof Detection [s]	Panel Fitting [s]	Yield Calculation [s]	Assessment Range [s]	Observer Spacing [s]	Module Visibility [s]	Total [s]	Average [s/m^2]
B1	2217	35	53	27	64	48	17	244	0.11
B2	2083	49	68	38	131	59	14	359	0.17
B3	4718	59	136	65	305	596	96	1257	0.27
B4	156	5	4	5	1	0	0	15	0.10
B5	2644	101	66	27	135	56	12	397	0.15
B6	11406	87	184	207	411	630	75	1594	0.14
B7	902	8	12	13	1	0	0	34	0.04
B8	11748	81	194	202	238	802	40	1557	0.13
B9	4688	62	120	69	1	0	0	252	0.05
B10	1944	3	21	32	54	49	6	165	0.08
B11	2059	11	58	41	155	50	3	318	0.15
B12	2354	12	82	41	1	0	0	136	0.06

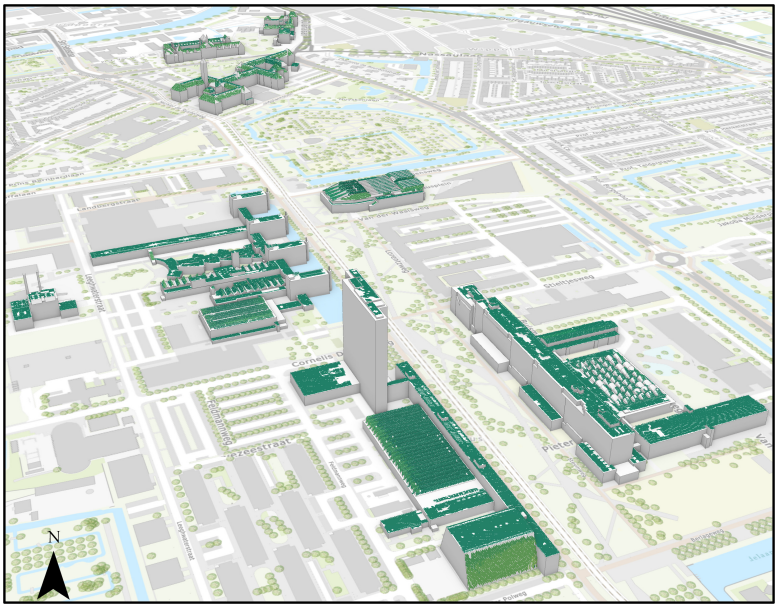

Figure 3.21: Screen shot of the web scene which includes the visibility assessment results for all the monumental buildings on TUD campus (Link: `https://tudelft.maps.arcgis.com/home/webscene/viewer.html?webscene=20d3763353b4470eb027ac1a30dd279c`).

This metric is obtained by dividing the time required for the entire workflow by the overall roof surface area processed. The difference in the computation time mainly lies in the level of complexity of the building layout, as those with a greater variety of roof types tend to include more observer points in the urban context, necessitating more LOS assessments.

3.3.6. Accuracy evaluation

The entire workflow has employed techniques that are broadly recognized for their accuracy, and the best practices have been followed when applying these methods. However, it is important to highlight that validating the specific implementation of these methods, especially on visibility outcomes, presents inherent challenges due to the subjective nature of visibility. The perception result can vary widely depending on the conditions of the observers; for instance, an individual who has been informed about the potential existence of PV modules on the monuments might perceive more PV modules than an uninformed observer. Therefore, the rigorous validation would have to implement the expert-based model or conducting questionnaires, where photos of the PV system from various observer points are taken and graded to establish a visibility scale. Such an approach, unfortunately, is not considered within the scope of this project. Instead, the simulation results from this work are serving as a guideline for decision-makers in identifying the low-hanging fruits. For roof surfaces with possible visibility concerns, this workflow still provides valuable location and PV potential information, which can be in-

strumental if a more detailed on-site visibility assessment is required.

3.4. Conclusions

In this chapter, a GIS-based large-scale visibility assessment tool is presented to assist in assessing the roof visibility for PV planning, where the monumental buildings on the TU Delft campus are taken as the case study. This tool operates in a raster-based representation of the environment with a cell size of 0.5 by 0.5 m^2, generated from freely available LiDAR data. Other inputs include cadastral data and road networks representing the public domain. The outputs contain multiple maps, including the roof binary visibility map (indicating if the roof cells are visible or invisible to the public domain), roof VA map (quantifying the visual amplitude of the roof cells relative to the public domain), PV module AC yield map (showing the potential layout of the rooftop PV system and their annual energy production), and PV module visibility map (categorizing the visibility of PV modules to the public domain into low, medium and high visibility groups).

The computational demand is mitigated by employing several optimization techniques, including parallel computing, which allows for the concurrent processing of multiple tasks across all processing units. Besides, a hemisphere filter is used to eliminate the observers that are lying behind the roof surface, drastically reducing time spent on unnecessary LOS assessment. The targets for LOS analysis are selected adaptively between roof cells and observer points, depending on which one has fewer points. Moreover, additional sensitivity analysis is included for every individual roof surface, where the analysis terminates once the optimal assessment range and observer spacing are found. As for PV module yield evaluation, an economic threshold of 650 kWh/kW_p is adopted, which excludes the PV modules whose yield is lower than this limit. The simulation results are published in the ArcGIS web scene and can be accessed with a personal Google account.

Given the raster resolution, the entire workflow takes, on average, 0.12 s/m^2, with a standard deviation of 0.06 s/m^2. Based on the AC yield evaluation results on twelve monumental buildings on the TU Delft campus, approximately 2.68 GWh/year of electricity can be harvested from imperceptible PV modules, while an additional 0.42 GWh/year of capacity is attributed to PV modules with medium visibility, and 0.37 GWh/year of capacity is associated with PV modules with high visibility. The contributed modeling workflow aids in the multi-criteria decision-making process for urban roof PV planning.

4

Climate impact of urban PV deployment

This chapter is based on the following publication:

Y. Zhou, S. Marathera, M. Zeman, O. Isabella, and H. Ziar, *Assessing the dual radiative consequences of urban PV integration: albedo change and radiative forcing dynamics*, Applied Energy **401**, 126544 (2025). (DOI: https://doi.org/10.1016/j.apenergy.2025.126544)

4.1. Introduction

The Earth continuously receives solar energy and radiates energy back to space. The balance between these energy flows is called radiative forcing (RF). Positive RF indicates that the Earth absorbs more energy than it radiates back to space, leading to the warming effect, while negative RF suggests the opposite. Globally, there are three primary factors influencing the RF and each of them is effective over different timescales: i) variation in solar irradiation, such as the 11-year sunspot cycle; ii) volcanic activities that inject particles and gases into the atmosphere, temporarily reducing incoming solar radiation and typically influencing RF over a few years; and iii) human activities, including fossil fuel combustion and land surface modification, which are currently recognized as the dominant drivers of global warming [112]. In the context of PV deployment, the integration of PV panels substitutes or covers the original urban surfaces with highly absorptive PV panels, leading to a reduction in urban albedo [113]. The reduced albedo enhances the positive RF and increases the energy absorbed by the Earth [26, 27]. Conversely, the deployment of PV panels displaces the use of fossil fuels, lowering the CO_2 concentration in the atmosphere and contributing to negative RF.

On a local scale, this changed urban albedo significantly contributes to the formation of urban heat islands (UHI), increasing the urban air temperature. This elevation in temperature not only boosts building cooling energy demand but also degrades the thermal comfort of urban dwellers, adversely affecting their health and potentially reducing

life expectancy [114]. In an early study modeling the impact of extensive PV deployment on urban air temperature within the Los Angeles Basin, Taha reported a cooling effect of 0.2 °C after retrofitting the roofs with PV panels of 30% of conversion efficiency [25]. In this analysis, the concept of effective albedo is used to quantify the albedo of PV panels, which essentially is the sum of reflectance and energy conversion efficiency of PV panels. This simplification is initially plausible as it accounts for the conversion of part of incident solar energy into electricity, which does not directly contribute to local urban heating. However, this assumption may lead to inaccurate results since the conversion efficiency of PV panels at operating conditions is often lower than the one outlined under the standard test conditions (STC) [115, 116]. Masson et al. simulated a scenario of PV deployment in the Paris metropolitan area, in which they discovered that PV panels reduce the UHI effect by 0.2 °C during the day and 0.3 °C at night [117]. Similarly, Salamanca et al. found a decreased near-surface air temperature following the implementations of PVs in the cities of Phoenix and Tucson [118]. However, both studies adopted the assumption that the temperature of the rear surface of PV panels is equal to the ambient air temperature. This assumption could be unreliable considering the small heat capacity of PV panels, meaning that the temperatures of the front and rear surfaces of PV panels should be closely aligned [119]. Cortes et al. performed a numerical simulation and reported a cooling effect of BIPV on urban air temperature, but the validity of these findings is debatable because the study used the questionable assumption that the albedo of PV cells is identical to that of the building envelope [120].

Contrasting conclusions have been reached by other studies suggesting that PV deployment may contribute to local warming. For instance, placing a large-scale PV array in the Mojave Desert of California can increase the local temperature by 0.4 °C when using the concept of PV effective albedo [121]. Complementary on-site measurements between the PV plant and adjacent wildlands observed that the temperatures above the PV plant are consistently warmer than wildlands by 3 - 4 °C [122]. Extending to the scenario of a densely populated city, Garshasbi et al. simulated the impact of PV deployment on air temperatures in Sydney during the summer months. The simulation indicated that expanding the coverage of urban roofs with PV panels from 25% to 100% could raise ambient air temperatures by 0.6 - 2.3 °C, and this temperature increase was translated to a cooling load penalty of around 1.7 to 6.8 kWh/m^2 [123]. Similarly, a consistent effect was also reported at the local district scale of Sydney, where deploying solar panels raises the summer daytime air temperature by 1.5 °C while reducing the nighttime temperature by 2.7 °C [124]. This inconsistency in the local environmental effect of PV deployment can be mainly attributed to the reliance on simplified assumptions in the models to address the complex urban energy balance. These simplifications often include the use of a constant PV conversion efficiency, an underestimation of the convective heat exchange with the environment at the rear side of PV panels, and inaccurate albedo assignments for the surrounding landscape. By refining these assumptions and incorporating the overlooked mechanisms of heat exchange between PV panels and the environment, it is expected that the implementation of PV panels in urban settings can lead to local warming during the day and potentially a cooling effect at night [125].

On a global scale, albedo plays a crucial role in our planet's climate dynamics. It is reported that the installation of solar farms can reduce the annual mean shortwave albedo

by 0.007 to 0.025, depending on the background surface replaced by PV panels [126]. Although the temperature increase due to the unit square meters of albedo change is relatively minor, the extensive installation of highly absorptive PV panels would still lead to measurable global climate warming [127, 128]. The fact that PV panels convert part of the incident solar energy into electricity redistributes the solar radiation received by the Earth, which alters the atmospheric circulation and influences regional and global climates. The majority of this generated electricity is consumed in urban areas and eventually is converted to heat, increasing the regional and global temperatures [129]. Nemet's research further quantified the positive RF resulting from albedo change due to PV deployment and compared it with the negative RF from the displacement of fossil fuels. It was determined that the RF avoided by replacing fossil fuels with PV is approximately 30 times greater than the effect induced by albedo modification [130]. These pioneering works have provided valuable insights into the role of PV in climate change mitigation, particularly by evaluating the positive RF caused by albedo reduction. However, many of these studies either neglect the negative RF resulting from fossil fuel displacement or estimate it using simplified assumptions or generalized PV yield calculation equations, especially at the urban scale, which may lead to inaccurate results. Additionally, the use of satellite data with coarse resolution, such as those from the Moderate Resolution Imaging Spectroradiometer (MODIS), poses significant challenges to assess the albedo modification before and after urban PV installation due to its spatial resolution, which is typically 500 meters. While this resolution is generally suitable for large-scale solar farms — where the surface albedo can be reasonably approximated by replacing the pixel's original value with that of PV panels — it is insufficient for urban environments. Urban PV systems are small, distributed across complex built environments, and often take up only a small fraction of each pixel. Therefore, pixel-level albedo replacement can be challenging to capture the spatial variance of PV, leading to inaccurate estimates of albedo change.

Therefore, The objective of this work is to fill the research gap by introducing a high-resolution approach to quantify both positive and negative RF effects of distributed urban rooftop PV systems. Compared to earlier studies using satellite data or simplified equations, this work introduces two novel simulation frameworks that leverage Light Detecting And Ranging (LiDAR) data. The first framework is an albedo simulation tool that simulates surface albedo changes before and after PV deployment. The second framework involves a large-scale rooftop PV simulation model designed to calculate PV electricity generation. The Netherlands, specifically the city of Delft, is selected for this study due to the authors' comprehensive access to the high-resolution datasets required for the analysis. Both frameworks are built to accurately calculate the radiative impacts of roof PV integration. The outcomes from these two frameworks are further translated into positive and negative RFs to calculate the Equilibrium Time (ET) — the duration required for the negative RF from PV electricity generation to completely offset the positive RF from albedo reduction.

4.2. Methodology

This section elaborates on the methods implemented in this study, which consist of three main steps: 1) albedo simulation, 2) PV electricity computation, and 3) RF calculation.

An overview of the steps employed in this analysis is illustrated in the flowchart as shown in Figure 4.1. Additionally, the simulated albedo results are cross-validated with MODIS albedo products, and the collection of MODIS data is also elaborated. Table 4.1 provides a summary of the software used in this study, including their respective tasks and the average runtime. The configuration of the computer used in this project has two AMD EPYC 7543 (32-core) processors running at a base frequency of 2.8 GHz and 128 GB of DDR4 RAM.

Table 4.1: Software used in this study, including their respective tasks and average runtime. The reflectance of SUNPOWER PSR-X21-350 IBC c-Si solar cell is used as the reflectance for PV material.

Software	Version	Task	Avg. runtime [min]
ArcGIS Pro	3.1.0	DSM generation	1.0 per tile
MATLAB	R2023a	GSA albedo simulation	77.6 per grid point
		Rooftop PV simulation	198.7
		RF calculation	0.2
		MODIS albedo processing	23.2

4.2.1. Geometric Spectral Albedo (GSA) model

The framework for albedo simulation was established based on the Geometric Spectral Albedo (GSA) model, which is a mathematical model incorporating the parameters influencing albedo such as geometry, material, and light source [131]. This model essentially decouples the upward radiation reflected from the surface into the contributions from shaded and unshaded differential sections, as illustrated in Figure 4.2. In this representation, a hypothetical albedometer S is denoted. The shaded sections receive exclusively diffuse horizontal irradiance (DHI), while the unshaded sections are exposed to both DHI and direct normal irradiance (DNI). The distribution of the shading pattern is further influenced by the surface roughness, which causes self-shadowing in the unshaded area, thereby converting some sections from being unshaded to shaded. Additionally, surface roughness can also obstruct the path of reflected radiation, preventing it from traveling from one section to the albedometer and thus not contributing to the albedo. Consequently, reflected light from the surface contributes to the albedo only if it is visible to the albedometer, and the extent of this contribution is determined by the illumination condition, surface material reflectivity, and the view factor of the differential section relative to the albedometer.

The general equation for temporal albedo α_t calculation implemented in this study is as follows:

$$\alpha_t = \sum_{i=1}^{N} R_i \left(C_i F_{S\to A_{i1}} + \frac{1}{H+1} \left(C_i' F_{S\to A_{i1}} + F_{S\to A_{i2}} \right) \right) \tag{4.1}$$

In this equation, t defines the temporal resolution and is considered hourly in this work. The albedo value is influenced by the shading pattern and five key variables: the reflectivity R_i of differential sections; the view factor F_i, which describes the proportion of radiation leaving the differential section i and reaching the albedometer S; the chance

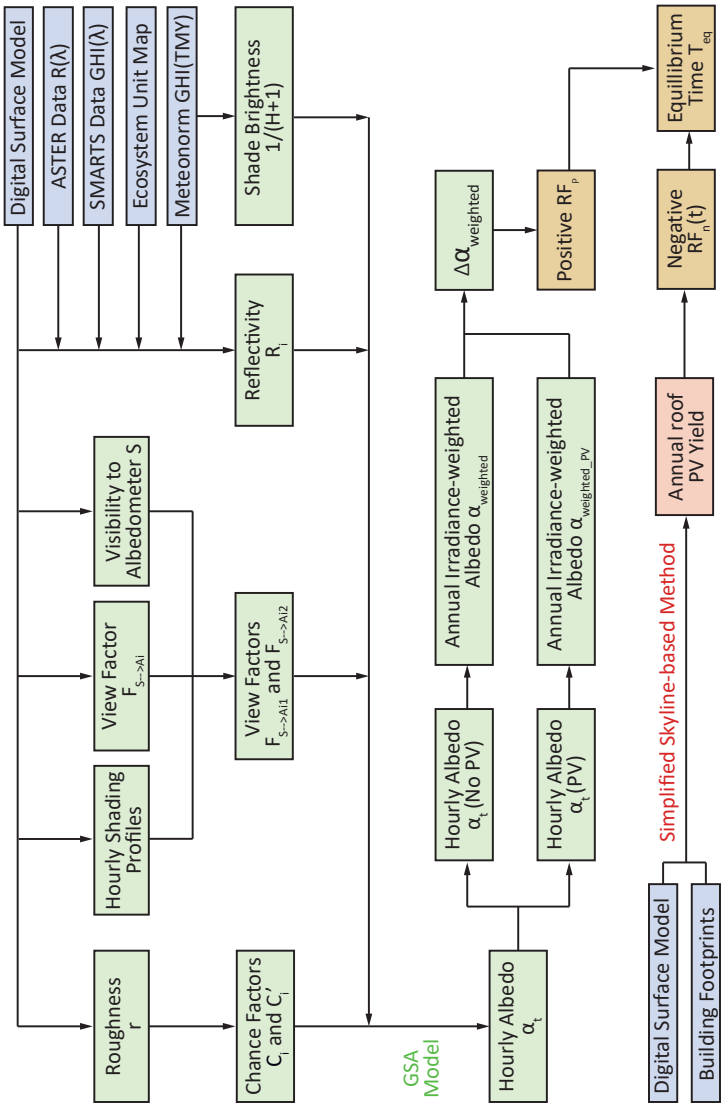

Figure 4.1: Flowchart showing the steps adopted in this study to i) simulate the albedo before and after rooftop PV integration (green blocks); ii) to compute the annual rooftop PV yield (red block); iii) to analyze the RFs induced by the rooftop integrated PV; and iv) to calculate the equilibrium time at which the negative RF exceeds the positive RF (yellow blocks). The blue blocks represent the input data. ASTER, SMARTS, and TMY refer to Advanced Spaceborne Thermal Emission Reflection Radiometer, Simple Model of the Atmospheric Radiative Transfer of Sunshine, and Typical Meteorological Year, respectively.

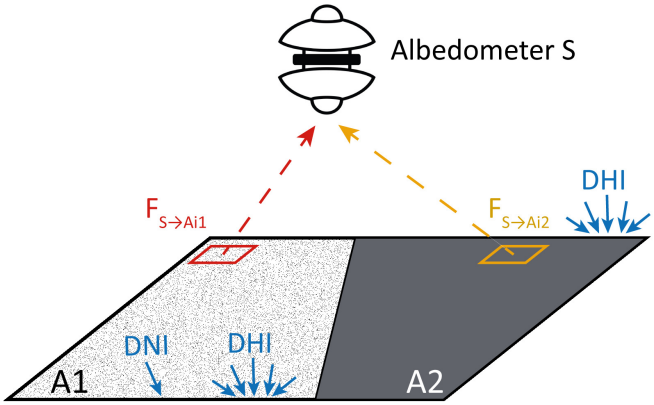

Figure 4.2: Visual illustration of GSA model with a rough surface being partially shaded. The unshaded and shaded sections are denoted as A1 and A2, respectively. Section A1 is exposed to both DNI and DHI, while section A2 only receives DHI. The view factor of each differential section relative to the hypothetical albedometer is indicated by F. Surface roughness causes self-shadowing within section A1 and obstructs the travel of reflected radiation from the surface to the albedometer.

factor C_i, which indicates the probability that a differential section is illuminated and visible to the albedometer due to self-shadowing; the chance factor C_i', which represents the probability that a differential section is shaded yet visible to the albedometer due to self-shadowing; and the variable H that is influenced by the sky condition and the Sun's position. These variables are determined by three primary factors: the material types, the terrain morphology, and the meteorological conditions.

Reflectivity of materials

R_i represents the reflectivity of differential section i, which is governed by its material property and incident solar spectrum. It is calculated using the directional hemispherical reflectance $R(\lambda)$ of the material of section i obtained from the Advanced Spaceborne Thermal Emission Reflection Radiometer (ASTER) library, and the hourly clear sky spectral irradiance $G(\lambda)$ generated from the Simple Model of the Atmospheric Radiative Transfer of Sunshine (SMARTS) software [133, 134]:

$$R_i = \frac{\int R(\lambda)G(\lambda)\,d\lambda}{\int G(\lambda)\,d\lambda} \tag{4.2}$$

SMARTS computes the solar spectrum considering the change in the Earth's atmosphere. The wavelength range for the integration is from 400 to 4000 nm, covering the typical short-wave radiation range. The yearly spectral irradiance, denoted as $G(\lambda)$, was generated on an hourly basis for the city of Delft. This dataset characterizes the varying solar spectrum profile due to changes in the atmosphere through which the light travels. Consequently, the reflectivity of materials R_i changes with the incident solar spectrum. While the clear sky spectra provide a theoretical maximum under ideal conditions, the

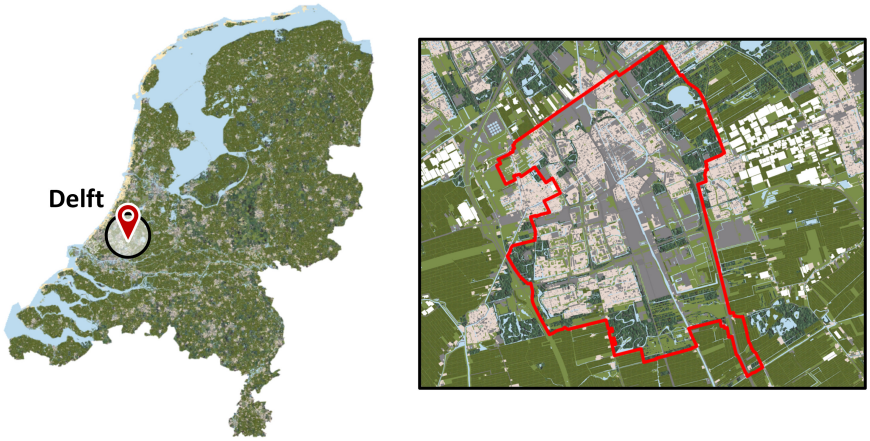

Figure 4.3: The processed Ecosystem Unit Map of the Netherlands (left) compiled for the year 2013, focusing on the city of Delft with the border highlighted in red (right) [132]. Each terrain type is represented by a uniquely colored polygon, encompassing a variety of materials, including water, greenhouse, grassland, residential area, and others. It is important to note that the colors of the polygons are solely for identification purposes and do not correspond to the actual properties of the materials. The albedo simulation is performed over the area highlighted on the right-hand side.

employment of the Typical Meteorological Year (TMY) data offers a more realistic solar radiation scenario [135]. Both datasets were temporally aligned, and the hourly spectral profile was adjusted according to the ratio of their respective Global Horizontal Irradiance (GHI) values:

$$G_{adj}(\lambda) = \frac{GHI_{TMY}}{GHI_{SMARTS}} G(\lambda) \tag{4.3}$$

where GHI_{TMY} is the hourly GHI at Delft from TMY, and GHI_{SMARTS} is the hourly GHI derived by integrating the SMARTS solar spectrum over the specified wavelength range. $G_{adj}(\lambda)$ is the adjusted spectral data used for reflectivity computation.

The material of sections within the studied terrain area was determined on the Ecosystem Unit Map of the Netherlands compiled for the reference year of 2013 [132]. This map captures the different land uses across the country and offers detailed information on the nationwide ecosystem for both natural and man-made areas with precise divisions. Figure 4.3 displays this map with a focus on Delft, in which each material type is represented by a uniquely colored polygon for identification. Initially, the map divided the ecosystem into thirty-one key units. Further analysis narrowed down these divisions into ten material classes for the application of this study, which are listed in Table 4.2. Each material class is represented by a distinct reflectance profile $R(\lambda)$, which corresponds to either one single material or a fusion of multiple materials. For instance, the road is assigned with the reflectance of pervious concrete, of which over 80% of the roads in the Netherlands consist [136]. The reflectance profile of coniferous forest predominately reflects pine trees, whereas deciduous forest equally combines the reflectance values of beech and oak trees [137]. The mixed forest is essentially an equal combination of the

coniferous forest and deciduous forest. The reflectance for greenhouses features both the aluminum frame and diffuse glass, where the latter was specifically measured with the PerkinElmer LAMBDA 1050 spectrophotometer for this study [138]. The PV technology selected for this study is interdigitated back contact (IBC) solar cell (SUNPOWER SPR-X21-350 IBC c-Si solar cell), and its spectral reflectance is measured with the same spectrophotometer. This technology is selected because IBC cells have no front-side metal contacts, which eliminates power losses due to metallization shading and aligns best with our scenario where PV is assumed to be fully integrated in building roofs. It is worth noting that this PV technology is adopted for both albedo and rooftop PV simulations. Additionally, the seasonal variation in vegetation was considered, which was reflected by using the ASTER reflectance data of the same material sample measured across different seasons. For example, the reflectance of deciduous forests is the equal combination of beech and oak leaves measured in the corresponding seasons. In winter, the reflectance of oak bark was employed to represent the forest's post-defrost reflectance.

Table 4.2: Materials adopted in the GSA model for albedo simulation. The reflectance of SUNPOWER PSR-X21-350 IBC c-Si solar cell is used as the reflectance for PV material.

Material Class	Material Reflectance	Seasonal Variation
Water	Water	N
Sand	Sand	N
Grass/Meadow	Bromus Grass	N
Road	Pervious Concrete	N
Coniferous Forest	Pine Tree	Y
Deciduous Forest	Beech Tree	Y
	Oak Tree	
	Oak Bark	
Mixed Forest	Pine Tree	Y
	Beech Tree	
	Oak Tree	
	Oak Bark	
Residential Building	Tiles	N
Greenhouse	Diffuse Glass	N
	Aluminum Frame	
Industrial Building	Asphalt Shingle	N

Shading pattern and geometric variables

The shading pattern and the geometric variables, including the view factor F_i and chance factors C_i and C_i', are derived from LiDAR. LiDAR is a remote sensing technique that is widely used to capture high-resolution topographical information of the Earth's surface. The data is collected by flying a plane equipped with a LiDAR sensor over the target area while sending laser pulses toward the ground. The time required for the reflected signals to return to the sensor provides information about the variation in terrain elevation. In

the Netherlands, the LiDAR data is available in several versions and organized into tiles, with each tile covering an area of 6,250 by 5,000 square meters. The most recent batch of LiDAR data (AHN5) is currently being collected and released. To ensure consistency with the year the Ecosystem map was created, the AHN3 LiDAR dataset is employed, which includes the data collected for Delft in 2014 [61]. Working with raw LiDAR data can be time-consuming due to its large number of data points. To simplify its application, the data is processed using the built-in geoprocessing tool in ArcGIS to generate a DSM. This model is composed of raster data with uniformly sized pixels, where each pixel represents the highest elevation of the data points found within it. In this work, the resolution of the pixel is 1 m, indicating that each pixel corresponds to an area of 1 m^2. Figure 4.4a displays the DSM of a single LiDAR tile, where the height range is indicated by the color bar transitioning from dark blue (lower elevations) to dark red (higher elevations). In Figure 4.4b, the Ecosystem Unit Map is merged with the DSM, providing each pixel with detailed information that includes both geographic coordinates and material class.

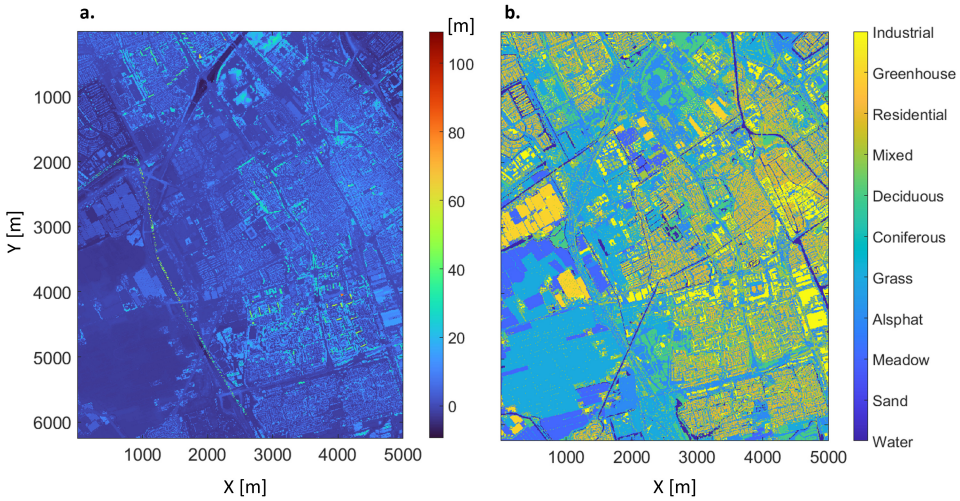

Figure 4.4: a) DSM of one LiDAR tile with an area of 6,250 by 5,000 square meters. The height values are indicated by the color bar; b) The same DSM is incorporated with the Ecosystem Unit Map, where each pixel contains both the height and material information.

The DSM is initially employed to generate the hourly shading pattern for albedo calculation. Typically, this shading pattern is derived by performing a LOS assessment for each DSM point at various sun positions, but this method can be computationally heavy and time-consuming due to the large amount of data points to process. To enhance the computational efficiency, an alternative computational geometry operation is used, which involves first transforming the axes of the point cloud to the UQP coordinate system so that the original Z-axis aligns with the Sun's position [54]:

$$\begin{cases} u = x\cos(\psi) - y\sin(\psi) \\ v = x\sin(\psi) + y\cos(\psi) \\ p = v\cos(\theta) + z\sin(\theta) \\ q = -v\sin(\theta) + z\cos(\theta) \end{cases} \tag{4.4}$$

In these equations, the x, y, and z are the coordinates of the DSM points, while ψ and θ are the hourly azimuth and altitude of the sun, respectively. In the UQP coordinate system, the P-axis is aligned parallel to the collimated sun rays, and the UQ plane is segmented into a regular grid with grid sizes of δ_u and δ_q along U and Q axes, respectively:

$$\begin{cases} i_u = \text{round}(\dfrac{u}{\delta_u}) \\ i_q = \text{round}(\dfrac{q}{\delta_q}) \end{cases} \tag{4.5}$$

Given the resolution of the DSM, a grid size of one meter is adopted. Originally, each DSM pixel contains one single height value that represents the highest LiDAR data within the cell. However, the axes transformation rearranges the distribution of DSM points so that multiple points occupy a single grid cell in the UQP coordinate system. Within each cell, the points that are located in the uppermost segment are identified as illuminated. When the Sun's altitude is low, Equation 4.4 demonstrates that the transformation becomes significant, leading to a substantial increase in the distance between the points within the UQP coordinate system. Therefore, after further considering the relatively low point density of the DSM used in this work, the depth of the uppermost segment, d_t, is determined by:

$$d_t = \frac{\text{grid size}}{sin(\theta)} \tag{4.6}$$

This threshold ensures the accurate clustering of points into the uppermost segment when the Sun's altitude is low. A detailed visual illustration of this transformation process is provided in the work of A.V. Vo et al. [54]. Figure 4.5 displays the hourly shading pattern of one building in Delft using the geometry operation method, with the direction of due North marked on the DSM. The shading results are presented in a binary format, where the illuminated pixels $A1$ are shown in white, while the shaded pixels $A2$ are shown in black. As the day progresses, the number of shaded pixels decreases in response to the rising altitude of the sun. Meanwhile, the orientation of the shading pattern shifts from facing west to east, aligning with the Sun's trajectory from east to west, which clearly demonstrates the evolvement of the shading pattern due to the Sun's movement.

The view factor F_i is calculated through the adapted direct integration method, assuming that the ground is parallel to the hypothetical albedometer S, the area of albedometer S is infinitesimally small, and the area of ground differential section is unit square meter [139]:

$$F_i = \sum_{i=1}^{N} \frac{\cos\theta_i^2}{\pi d_i^2} \tag{4.7}$$

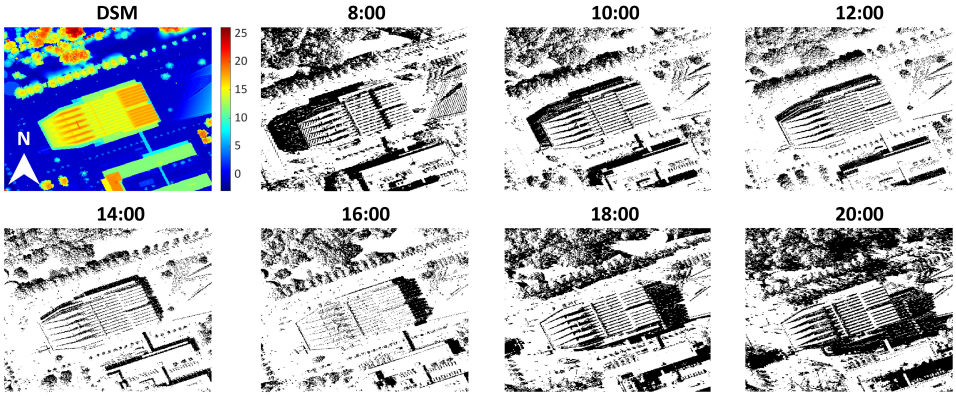

Figure 4.5: Hourly shading pattern of one building on the campus of TUD on the 31st of May, where the direction of due North is marked on the DSM. The shading pattern evolution demonstrates how the shading pattern changes as the day progresses by using the geometry operation method.

where d_i is the linear distance between the albedometer S and the center of ground section i, while θ_i is the angle between this line and the surface normal of ground section i. Here, the hypothetical albedometer S is positioned at the center of the DSM tile, elevated 500 meters above the tile's average height. This positioning ensures that the view factors from the entire tile converge at the albedometer [140]. The chance factors C_i and C_i' model the self-shadowing of the surface caused by its roughness. These two probabilities are dependent on the roughness r, which is calculated as the root mean square (RMS) slope of the profile [141]:

$$\sqrt{\frac{(\Delta q_x^2 + \Delta q_y^2)}{2}} \tag{4.8}$$

where

$$\Delta q_x = \sqrt{\frac{1}{N-1}\sum_{i=1}^{N}\left|\delta_{xi} - \bar{\delta_x}\right|} \tag{4.9a}$$

$$\Delta q_y = \sqrt{\frac{1}{N-1}\sum_{j=1}^{N}\left|\delta_{yj} - \bar{\delta_y}\right|} \tag{4.9b}$$

The variables δ_{xi} and δ_{yj} are the slopes along x and y directions, respectively, while $\bar{\delta_x}$ and $\bar{\delta_y}$ represent the mean values of these slopes. The chance factors are specifically applied to the illuminated region $A1$, identifying which sections are self-shadowed or illuminated while remaining visible to the albedometer S. As elaborated in Equation 4.1, the view factor of these self-shadowed sections $C_i' F_{S \to A_{i1}}$ is incorporated into the shaded region to complete the albedo computation.

Shade brightness H and irradiance-weighted albedo

The variable H is determined by the meteorological data:

$$H = \frac{DNI_M}{DHI_M} cos\theta_M \tag{4.10}$$

where θ_M is the angle between the incident irradiance and the normal direction of the differential section. The term $1/(H+1)$ in equation 4.1 is defined as the shade brightness, which indicates that the albedo increases under overcast sky conditions and at lower solar zenith angles. These predictions are in agreement with the previously published experimental results [142]. Furthermore, the hourly albedo results are weighted based on the irradiance GHI, and the annual average albedo at the location of interest is obtained:

$$\alpha_{weighted} = \frac{\sum_{t=1}^{8760} \alpha_t GHI_{TMY}(t)}{\sum_{t=1}^{8760} GHI_{TMY}(t)} \tag{4.11}$$

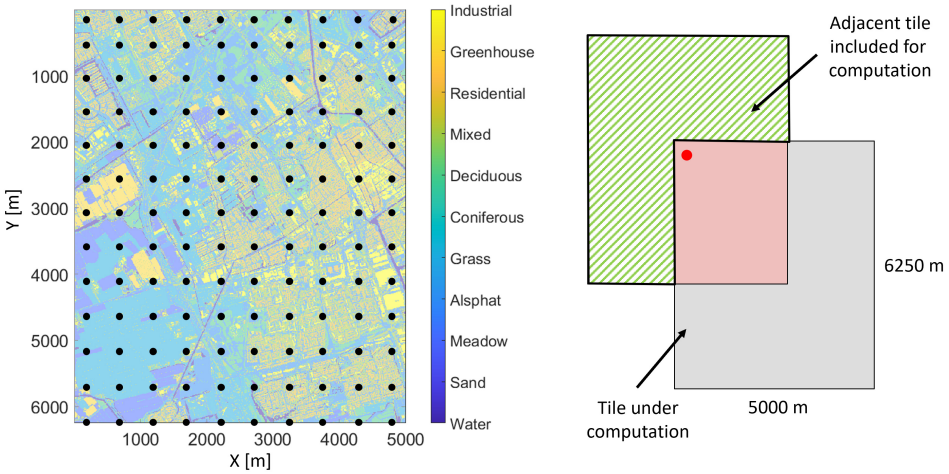

Figure 4.6: The albedo simulation is performed on a 10 by 13 grid, with each grid point spaced 500 meters apart in both the x and y directions. To ensure that the view factor converges to one, the DSM from the adjacent tile is used, as illustrated on the right.

Incorporating GHI into albedo calculation provides a more accurate representation of albedo's impact on the energy balance. This is because the albedo on a sunny day with great GHI contributes significantly more to the Earth's energy balance than the albedo on an overcast day when the GHI is substantially lower. The albedo simulation is conducted on the four tiles covering the DSM of city of Delft, each segmented into a 10 by 13 grid with grid points spaced 500 meters apart along both the x and y directions, as shown on the left in Figure 4.6. This resolution is chosen to be the same as the one provided in the MODIS products for cross-validation. To ensure that the view factor converges to one given the height of the hypothetical albedometer S, the DSM from adjacent tiles is incorporated into the albedo computation. This is illustrated on the right in Figure 4.6,

where the top left grid point of the tile under simulation integrates missing DSM data from the neighboring tile highlighted in green strips.

4.2.2. Rooftop PV yield calculation

The framework for rooftop PV calculation was developed based on the simplified skyline-based method [59]. This method estimates the annual energy yield of the rooftop PV installation by correlating the energy production to the SVF and the SCF through a polynomial equation:

$$E_Y = \sum_{k=1}^{3} d_k(1 - \mathrm{SCF}^k) + (d_4 + d_5\alpha_{gnd})\mathrm{SVF} \tag{4.12}$$

The SVF represents the fraction of the sky that is visible from a certain point, and the SCF at a location is defined as the ratio between the total annual duration that the sun is obscured by the PV panel and the skyline to the total sunshine duration at the same location with a clear horizon. The coefficients d_1 to d_5 are obtained from linear and cubic fittings for different combinations of PV tilt and orientation, and α_{gnd} is the ground albedo.

To implement this method, building footprints are first used to identify buildings and extract DSM points for roof surfaces [96]. The extracted roof points are then clustered, and a plane-fitting algorithm is employed on the clustered roof points to determine their orientation and tilt angles [143]. This roof property information is crucial for selecting the appropriate coefficients for energy yield calculation. After that, the skyline profile for each building point is generated by scanning the surrounding environment with a radius of 100 meters, and the generated skyline profile serves as the input to compute the SVF and SCF [71]. This process is repeated for all the detected roof points, with Equation 4.12 applied to calculate the annual PV electricity production. Here, a PV panel based on IBC c-Si solar cells (SUNPOWER SPR-X21-350) is selected as the PV technology for roof-integrated PV electricity simulation, and two PV integration scenarios are investigated: 1) a scenario where all roof surfaces are assumed to be integrated with PV; 2) a scenario in which only those roof surfaces meeting a specific yield threshold of 650 kWh/kW$_p$ are integrated with PV [39].

4.2.3. Radiative forcing calculation

The RF calculation is divided into two parts: the positive RF due to albedo decrease and the negative RF resulting from the CO_2 concentration reduction in the atmosphere due to the replacement of fossil fuels with PV. The calculations are performed using the albedo simulation results from this work and the inputs published in the paper by Wohlfahrt et al. [144].

The positive RF due to the decrease in albedo is calculated as:

$$RF_p = \frac{\sum_{m=1}^{12} K_m \Delta\alpha_m}{12} \frac{A_{PV}}{A_E} \tag{4.13}$$

Here, K$_m$ [W/m^2] represents the radiative kernel for monthly climatological albedo changes over a decade (2007 to 2016), which estimates the change of top-of-the-atmosphere

(TOA) RF resulted from unit change in albedo [145, 146]. In this work, the coordinates of the DSM pixels covering the Delft area are used to retrieve the corresponding radiative kernel values. $\Delta\alpha_m$ is the albedo change resulting from integrating PV on building roofs, A_{PV} [km^2] is the area of the map pixel influenced by rooftop integrated PV, and A_E [km^2] is the surface area of the Earth. K_m is retrieved for each grid point based on its converted latitude and longitude coordinates, and the positive RF is calculated with its corresponding albedo change. The total positive RF is determined by summing up the RFs of all the grid points.

The negative RF from replacing the fossil fuel with PV is calculated on a monthly basis by converting the generated PV electricity to the equivalent CO_2 reduction :

$$RF_n(t) = k_{CO_2} \int_{t'=0}^{t'=t} I_{carbon} E_{CO_2}(t') \mathrm{IRF}_{CO_2}(t-t')\, dt' \tag{4.14}$$

where k_{CO_2} [1.76×10^{-15} W/m^2/kg] is the radiative forcing induced by increasing unit kilogram of CO_2 at a given CO_2 background concentration [147], I_{carbon} [kgCO_2/kWh] is the electricity carbon intensity where the average (2010 - 2017) value for the Netherlands is used in this work [148], E_{CO_2} [kWh/year] is the annual roof PV electricity generation, IRF_{CO_2} is the impulse-response function modeling the exponentially decaying CO_2 concentration over time after a pulse emission of CO_2 into the atmosphere [149], and t and t' represent the actual and integration time steps, respectively. Based on Equations 4.13 and 4.14, the equilibrium time ET is calculated at which the negative $RF_n(ET)$ exceeds the positive RF_p.

4.2.4. MODIS albedo products

The MODIS MCD43A3.h18v03.061 Terra + Aqua BRDF albedo products are downloaded with a spatial resolution of 500 meters [150]. Such data comprise daily albedo records and are requested for a time period of 10 years (2012 - 2021). Pixels that contain Delft are identified based on their geographical coordinates, ranging from pixel (636,1913) to pixel (655,1928) along longitude and latitude, respectively. After that, the daily white-sky albedo α_{ws} (Albedo_WSA_shortwave) and black-sky albedo α_{bs} (Albedo_BSA_shortwave) are retrieved for the shortwave band for each identified pixel, and further averaged across the chosen decade. The actual daily blue-sky albedo (α_{bs}) is calculated as:

$$\alpha_{bs} = \alpha_{ws} f_{dif} + \alpha_{bs}(1 - f_{dif}) \tag{4.15}$$

Here, f_{dif} is the annual average of the hourly fraction of global horizontal irradiance relative to the extraterrestrial irradiance.

4.3. Restuls and discussion

4.3.1. Albedo results from the GSA model

To analyze the hourly variation in albedo values, the albedo $\alpha_{t,6,5}$ (at grid point located in the 6$^{\text{th}}$ row and the 5$^{\text{th}}$ column with respect to the top-left corner) is examined. Figure 4.7 shows its hourly albedo results and the corresponding GSA variables on both sunny (July 28$^{\text{th}}$) and overcast (July 29$^{\text{th}}$) days. The plots are arranged from top to bottom, where the

x-axis indicates the time of the day and the y-axis presents the hourly albedo α, reflectivity R, shade brightness $1/(H+1)$, view factor of the illuminated and visible sections $F_{S\rightarrow A1}$, and the view factor of the shaded and visible sections $F_{S\rightarrow A2}$, respectively.

On sunny days with clear skies, albedo is higher at sunrise and sunset hours, while it remains lower for the rest of the day. This diurnal variation in albedo is largely due to the change in the Sun's altitude [151]. At sunrise and sunset, when the sun is low on the horizon, the sunlight is more likely to be reflected directly back into the atmosphere without interacting with lower objects. As the sun rises, more sunlight is intercepted by the objects, effectively trapping more radiation within the urban context and consequently lowering the albedo. This behavior is also reflected in the shade brightness, which is higher at sunrise and sunset due to lower DNI. As the day approaches noon, shades are usually darker because of the larger DNI resulting from the higher Sun's altitude. Meanwhile, the change in the Sun's position also affects the distribution of view factors contributed by the shaded and illuminated sections. Higher Sun's altitude leads to more illuminated sections, as illustrated in Figure 4.5, which increases the view factor of illuminated and visible sections $F_{S\rightarrow A1}$ and reduces the view factor of shaded and visible sections $F_{S\rightarrow A2}$. On overcast days, albedo remains high and fairly constant for the entire day. Shade brightness is nearly one, indicating minimal or negligible DNI throughout the day. As a result, the view factor for illuminated and visible sections $F_{S\rightarrow A1}$ reduces to zero, whereas the view factor for shaded and visible sections $F_{S\rightarrow A2}$ becomes predominant. These daily albedo variation patterns are in line with the albedo measurements in clear and overcast days reported in the literature [131]. Additionally, it can be observed that the reflectivity R is constantly higher than the albedo α for both sunny and overcast days. This means that the reflectivity R sets the upper limit of the albedo, and both the shade brightness $1/(H+1)$ and the view factors $F_{S\rightarrow A1,A2}$ determine the variation of the albedo.

In Figure 4.7, the daily and monthly variations in albedo are also presented, with values weighted according to Equation 4.11 based on hourly GHI. The daily albedo shows significant fluctuations throughout the year, primarily due to the frequent varying meteorological conditions, as they determine the shade brightness that affects the albedo variation. The monthly albedo exhibits a more regular trend where the weighted albedo stays between 0.12 to 0.15. Typically, the albedo is higher in winter months while lower in summer months, depending on the locations [152]. The integration of GHI into albedo calculation compensates for the monthly variation of GHI, resulting in a more constant albedo value throughout the year. The annual GHI-weighted albedo for this specific grid point $\alpha_{weighted,6,5}$ is calculated to be 0.1352.

The same process was extended to the rest of the grid points, and the annual GHI-weighted albedos derived from the GSA model are shown in Figure 4.8a. It can be observed that the albedo values for this area vary from 0.09 to 0.23, with lower values found in urban areas and higher values in surrounding rural areas. This variation can be mainly attributed to the differences in material reflectivity and terrain roughness under identical meteorological conditions. As depicted in Figure 4.8c, urban areas typically have lower reflectivity due to the use of absorptive construction materials, which directly contribute to a lower albedo. Meanwhile, as illustrated in Figure 4.8d, the urban environments exhibit higher terrain roughness due to densely built constructions and artificial

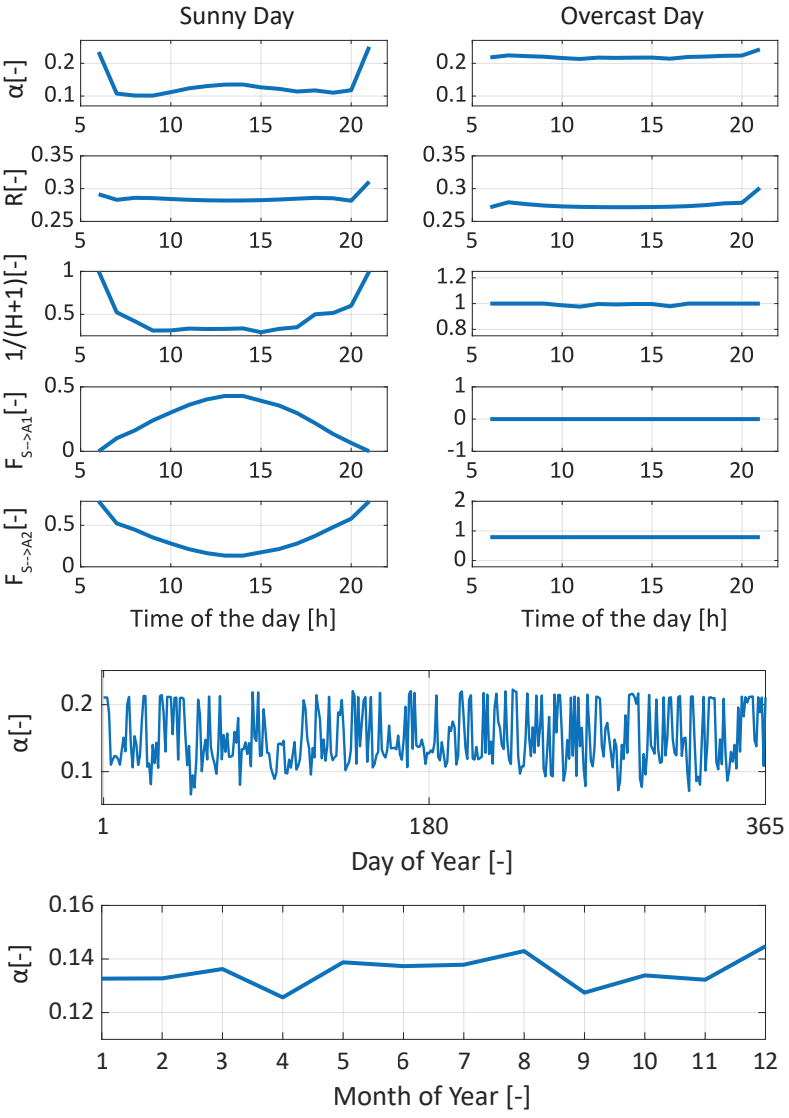

Figure 4.7: The hourly albedo $\alpha_{6,5}$ on both sunny and overcast days, and its corresponding GSA variables including reflectivity R, shade brightness $1/(H+1)$, view factor of the illuminated and visible sections $F_{S\rightarrow A1}$, and the view factor of the shaded and visible sections $F_{S\rightarrow A2}$. The reflectivity R sets the upper limit of the albedo, and both the shade brightness $1/(H+1)$ and the view factors $F_{S\rightarrow A1,A2}$ determine the variation of the albedo. The daily albedo varies significantly due to the daily fluctuation of meteorological conditions, while the monthly albedo is more consistent throughout the year.

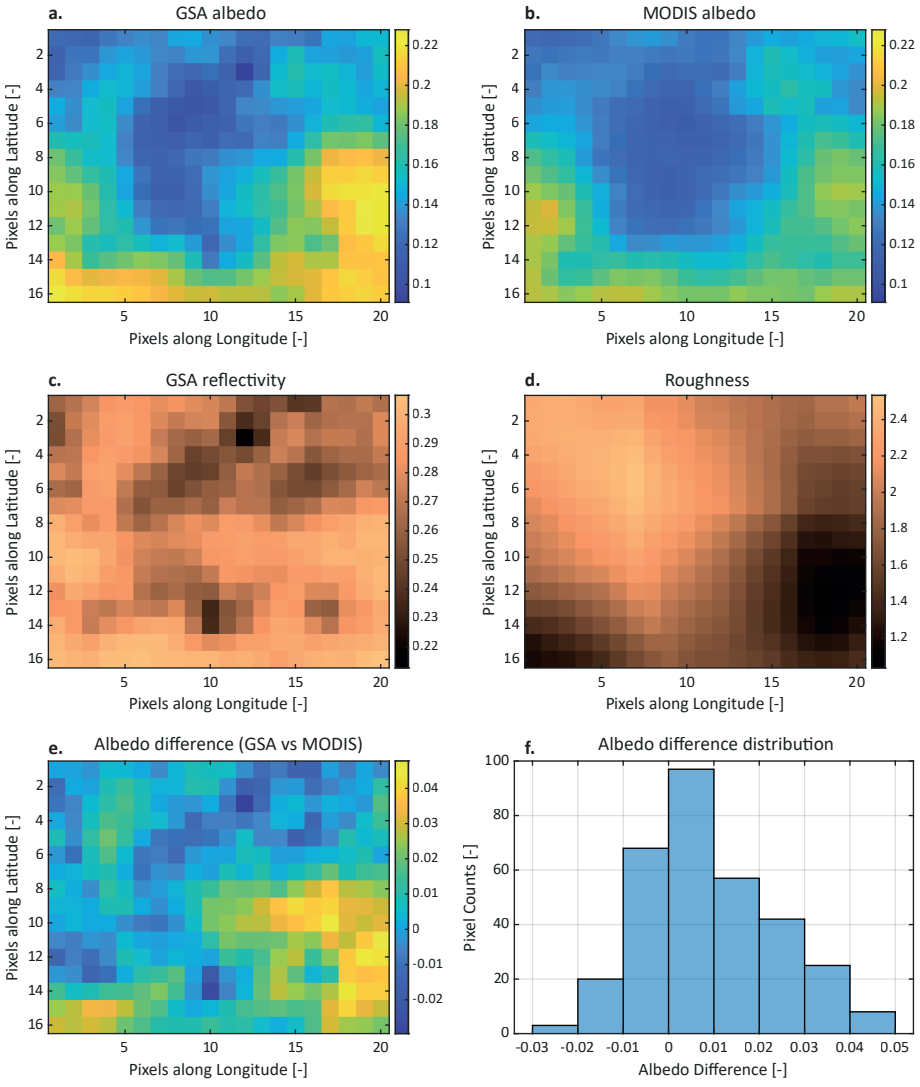

Figure 4.8: The albedo map of the rectangular area covering Delft, including a) The GHI-weighted annual average albedo from the GSA model; b) The blue-sky albedo from MODIS averaged over year 2012 to 2021; c) The annual average reflectivity from the GSA model; d) The roughness from the GSA model; e) The albedo difference between the GSA model and MODIS products; f) The distribution of the albedo differences.

structures, whereas rural areas show significantly lower roughness. This increased terrain roughness in urban areas effectively traps more radiation, reducing the amount that is reflected back into space and consequently lowering the albedo. To evaluate the sensitivity of the GSA albedo to key surface parameters, a local sensitivity analysis is performed by systematically perturbing all surface material reflectivity, PV reflectivity, and terrain roughness by ±20%. The results, presented in Figure 4.9, reveal that increases in all material reflectivity lead to a notable increase in albedo, with a linear response slope of 0.135. Perturbation in PV reflectivity poses only a minor effect (slope = 0.004), mainly because of the small fraction of the roof area replaced by PV material. Conversely, increasing terrain roughness leads to a decrease in albedo, with a negative slope of -0.047. These findings highlight the importance of both material properties and surface complexity in determining albedo, as well as the role of dense urban morphology in trapping solar radiation and reducing reflected energy. Considering the strong linear correlation between surface material reflectivity and albedo results, the uncertainty introduced by non-representative material selection or assignment is likely the major source of error in the GSA albedo model.

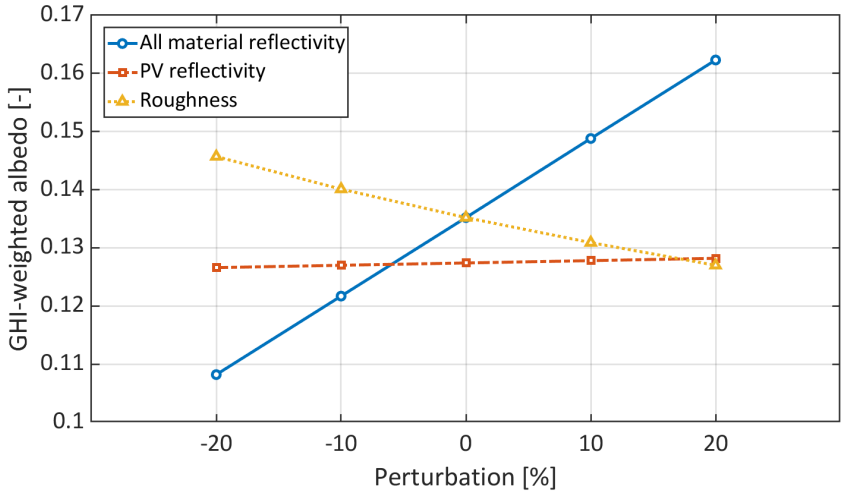

Figure 4.9: Sensitivity analysis of the GSA albedo model on $\alpha_{weighted,6,5}$ with respect to material reflectivity, PV reflectivity, and surface roughness perturbations.

Figure 4.8b shows the MODIS albedo results over the same area, which are obtained by averaging daily albedo values over a decade (2012 – 2021). While the MODIS albedo map presents a similar distribution pattern to the one derived from the GSA model, with lower albedo values in urban areas and higher in surrounding rural areas, there are some differences: first, the urban area characterized by lower albedo appears smaller in the GSA albedo map; second, the albedo values in the surrounding rural areas are higher in the GSA albedo map. Considering the sources of uncertainty from the GSA albedo model, these discrepancies can be mainly attributed to the incompleteness of the material reflectivities employed in the simulations. As depicted in Figure 4.8e, the differ-

ences in albedo are concentrated largely in rural regions and parts of the urban area, which closely matches the reflectivity map. This suggests that variations between GSA and MODIS albedo maps are mainly driven by the choice of material reflectivities. Here, ten representative material classes are implemented for the albedo simulation. However, in reality, the materials are highly diverse and can vary depending on the location, regulations, and specific requirements. Completing the material database and refining material assignments in the DSM could enhance the accuracy of simulated albedo results. Additionally, the method used to generate the hourly shading profile can also affect albedo outcomes. While the employed geometry operation is time efficient, it offers lower accuracy compared to the LOS method considering the resolution of the DSM. This may result in inaccuracies in the shading profile, where some pixels that should be shaded are incorrectly classified as illuminated, and vice versa. Meanwhile, the simulated albedo values represent the case with the albedometer positioned at 500 meters above the ground. Converting these values to TOA albedo requires an additional correction for atmospheric attenuation, which typically reduces the albedo values.

Considering the sources of uncertainty in the MODIS albedo product, the albedo difference can be introduced from several factors: the quality of measurement data, the assumptions and limitations of the bidirectional reflectance distribution function (BRDF) model used to derive albedo, and the biased measurement data due to complex geometry and anisotropic surfaces in the urban environment. First, MODIS sensors collect directional reflectance of surfaces from different viewing angles. The successful observation, however, is subject to cloud-free conditions. If multiple observations over the 16-day window are cloud-contaminated, the BRDF model cannot be reliably fitted, resulting in invalid or low-quality albedo values. Filtering out these invalid albedo values can lead to a less representative yearly average albedo. Second, the BRDF model implemented to compute MODIS albedo is a semi-empirical model originally developed for homogeneous and temporally stable surfaces. Therefore, it is more suitable for vegetated surfaces whose conditions do not change significantly during satellite observation, and it is less suited for complex urban environments or for dynamic surfaces featuring vegetation growth cycles [153, 154]. Third, urban areas are characterized by high spatial heterogeneity and fast-varying geometry. Within a single MODIS pixel, rooftops, roads, vegetation, or any type of urban artifacts may all contribute to the observed signal. This means that different materials can dominate the reflectance signal at different times when the pixel is observed from changing viewing angles within the 16-day window. This angular inconsistency in reflectance sampling can introduce deviations in the derived albedo [155].

Figure 4.8f presents a histogram plot that clustered the albedo differences into eight bins. According to this analysis, 71.56% of the pixels in the GSA albedo map have higher albedo values compared to the MODIS albedo map. More specifically, 51.56% of the pixels differ by ±0.01, 75.62% of the pixels differ by ±0.02, and 89.69% of the pixels differ by ±0.03. The overall average albedo of the entire area is found to be 0.1584 for the GSA model and 0.1493 for MODIS products, leading to an absolute difference of 6.12%.

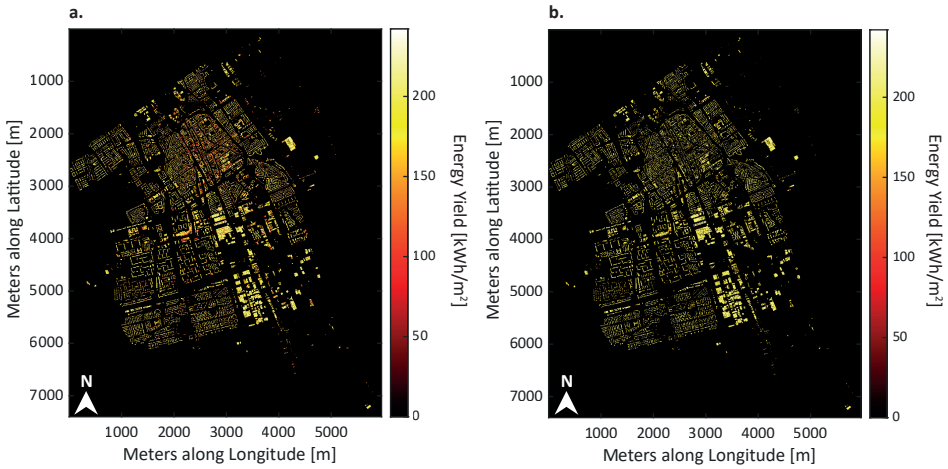

Figure 4.10: Annual PV energy yield maps for 1) all roof surfaces are integrated with PV; 2) only the roof surfaces meeting the specific yield threshold of 650 kWh/kW$_p$ are integrated with PV.

4.3.2. Annual roof PV energy from simplified skyline-based method

Figure 4.10a shows the annual PV energy yield map for the first scenario, in which all roof surfaces are assumed to be integrated with PV. The x- and y-axes represent the absolute distances of the area along longitude and latitude in meters, respectively, with due North indicated in the bottom left corner of the figure. The energy yield per square meter is depicted by a color scale, transitioning from black (low yield) to white (high yield). It can be observed that in the densely constructed urban area, the PV potential is relatively lower due to the elevated skyline. The north-facing roof surfaces also provide lower PV potential due to the suboptimal orientation. Figure 4.10b presents the results for the second scenario, where only the roof surfaces meeting the specific yield threshold of 650 kWh/kW$_p$ are integrated with PV. This leads to fewer roof pixels on the solar map, primarily those within urban areas or with unfavorable orientations, as they often fail the required specific yield threshold. As a result, the total PV integrated roof area is decreased from 2.8289 km^2 to 2.2425 km^2. The total annual roof-integrated PV yield for Delft is further calculated to be 485.72 GWh/year and 434.82 GWh/year for the first and second scenarios, respectively.

4.3.3. Positive and negative radiative forcings

The positive RF is calculated from the decrease in albedo after the integration of PV on building roof surfaces. Figure 4.11a shows the albedo map of the same rectangular area covering the entire city of Delft after all the roof surfaces are replaced with PV. Compared to Figure 4.8a, this map presents a noticeable reduction in albedo within the urban area. Figure 4.11b displays the location and extent of the albedo decrease, with a color bar transitioning from black (indicating a large decrease) to white (indicating a small decrease). The maximum absolute albedo reduction due to roof PV integration is found to be -0.0306. From Equation 4.13, the positive RF after integrating PV into all detected

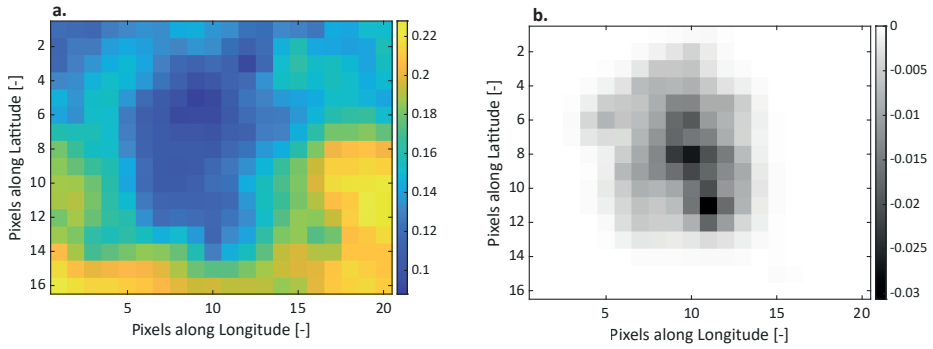

Figure 4.11: a) The albedo map of the rectangular area including Delft after replacing all the roof surfaces with PV; b) The absolute albedo difference on the map before and after PV integration on all the roof surfaces in Delft.

roof surfaces in Delft is calculated to be 3.53×10^{-8} W/m^2. Assuming a grid carbon emission intensity of 437 g CO_2-eq/kWh, the negative RF is calculated from Equation 4.14, and the equilibrium time is determined to be 39.2 days [148]. The same process is repeated for scenario two, and the positive RF and the equilibrium time are found to be 3.40×10^{-8} W/m^2 and 42.0 days, respectively. For both scenarios, the negative RF from PV-generated electricity offsets the positive RF from albedo reduction in around forty days. This rapid offset can be mainly attributed to the fact that the urban environment already has a low albedo, which minimizes the impact of the further albedo reductions on positive RF caused by PV integration. Conversely, integrating PV in areas with high initial albedo would result in a more substantial decrease in albedo, thereby extending the time required to offset the associated positive RF. Meanwhile, PV has a relatively high energy density (171.1 kWh/m^2 for scenario one and 193.9 kWh/m^2 for scenario two), leading to a larger negative RF per unit area of PV integration. Even when PVs are integrated on roofs with unfavorable orientations, their high energy density is sufficient to offset the positive RF induced by albedo changes at a relatively fast pace, which leads to a slightly extended equilibrium time in scenario two.

The current simulation framework considers exclusively the positive RF associated with albedo reduction due to urban roof PV integration, which is the primary scope of this study. However, it is important to recognize that the full life cycle of PV modules, including solar cell production, module manufacturing, transportation, operation, disposal, and recycling also contribute to CO_2 emissions. For c-Si PV modules, the typical carbon emission intensity ranges from 13 to 30 g CO_2-eq/kWh, which is significantly smaller than that of fossil fuel-based electricity (437 g CO_2-eq/kWh for the Netherlands in 2017) [148, 156]. Under the current carbon-intensive energy infrastructure, the equilibrium time remains short as demonstrated, indicating that albedo-related positive RF has a minor role. However, as the energy infrastructure decarbonizes through the penetration of renewable energies, the grid's carbon emission intensity progressively decreases. In a future scenario where electricity supply is predominantly based on renewable energy and the grid's carbon emission intensity decreases to the level associated

with current c-Si PV modules, the equilibrium time for a fully integrated roof PV scenario in Delft extends to 1548.5 days and 623.1 days under the 13 g and 30 g CO_2-eq/kWh cases, respectively. As the global energy structure becomes more sustainable and PV's carbon emission intensity continues to decline with technology advancements, the relative impact of albedo-induced positive RF on global warming will become more pronounced. This highlights the importance of incorporating the albedo effects of PV deployment into future LCA to provide a more realistic evaluation of the global warming mitigation potential of PV technology.

Once the PV system is in operation, it continues to contribute to negative RF throughout its lifetime as long as the energy system is not fully decarbonized. Table 4.3 presents the cumulative negative RF from roof PV integration in Delft over 5, 10, 15, 20, 25, and 30 years. The results assume a constant annual PV electricity yield and a fixed grid carbon emission intensity. As expected, the cumulative negative RF increases over time, while the increment between every 5-year interval gradually decreases. By the end of the PV system's typical lifetime (between 25 to 30 years), the cumulative negative RF reaches 6.74 and 7.85 $\times 10^{-6}$ W/m^2 for scenario one and 6.03 and 7.03 $\times 10^{-6}$ W/m^2 for scenario two. These numbers are approximately 170 to 230 times larger than the initial positive RF caused by albedo reduction. However, it is worth noting that PV electricity production declines over time in practice due to module degradation, and the carbon emission intensity of the grid is expected to decrease as energy systems decarbonize. Therefore, these values may be overestimated.

Table 4.3: The cumulative negative RF from roof PV integration in Delft over 5, 10, 15, 20, 25, and 30 years.

Cumulative years	Scenario 1 ($\times 10^{-6}$ W/m^2)	Scenario 2 ($\times 10^{-6}$ W/m^2)
5	1.70	1.52
10	3.10	2.77
15	4.40	3.94
20	5.61	5.02
25	6.74	6.03
30	7.85	7.03

Globally, albedo typically increases with latitude, being higher at higher latitudes and vice versa [157]. PV generation profile, in contrast, is the opposite, where PV yield peaks at lower latitudes and decreases towards higher latitudes. Therefore, integrating PV at higher latitudes would result in a longer timespan to offset the positive RF due to relatively larger albedo reduction and smaller PV generation. Regionally across Europe, surface albedo varies due to differences in land cover and seasonal conditions. In northern Europe, albedo tends to be higher, especially in winter with widespread snow cover. Moving southward into central Europe, the surface albedo generally decreases as the landscape transitions to a mix of forests, grassland, and urban areas. The Netherlands falls within this lower-to-middle surface albedo range due to its mixed urbanized and agricultural landscapes. In southern Europe, surface albedo increases again due to a more open landscape and less dense vegetation [158]. This spatial distribution indicates that under original surface albedo conditions, central Europe contributes more to pos-

itive RF. Meanwhile, PV deployment in northern and southern Europe leads to larger increases in positive RF because of higher initial albedo values. However, further considering the cloud cover may influence this effect [159]. In regions with frequent cloudy or overcast weather, such as the Netherlands and northern Europe, the positive RF due to albedo change is partially mitigated, as less incoming solar radiation reaches the surface. In contrast, southern Europe typically experiences more clear and sunny weather, leading to stronger positive RF from albedo reduction, but this effect can be offset more quickly by the higher PV yield.

With ongoing advancements in the PV industry, PV cells are designed to be more absorptive, featuring lower reflectivity, yet delivering higher efficiency attributed to the mature manufacturing processes and innovative cell architectures. This reduction in reflectivity leads to a decrease in albedo, thereby increasing the positive RF when PVs are integrated into areas with initially higher albedo. On the other hand, the enhanced efficiency of PV cells converts more solar energy into electricity, which reduces the timespan that is required to offset the positive RF. Therefore, there is a trade-off between reducing reflectivity and increasing efficiency in the RF effects of PV cells. Considering that the reflectivity of PV cells is already very low, the benefits from increased efficiency would outweigh those from reduced reflectivity, meaning that installing high-efficiency PV cells in urban areas is more advantageous to the energy balance of the Earth during the transition to a fully renewable-energy-powered future. However, from a long-term perspective, once fossil fuels are completely phased out, the reduced albedo from PV installation will still increase the positive RF, regardless of the efficiency of PV cells. This occurs because the electricity generated by PV cells is ultimately converted to heat that is released into the environment. A potential solution is the development of colored PV cells designed to mimic the color and appearance of the background materials or of the infrared filters that reflect the unwanted irradiance back into the space [28]. The former approach preserves original albedo values while generating green electricity. In a strategic scenario, reflectivity could be optimized based on the city-scale PV yield simulations to maximize albedo and still meet the local energy demands. In this way, the overall albedo of urban environments would be increased, minimizing the positive RF and still securing a sustainable supply of green electricity.

4.4. Conclusions

In this chapter, a comprehensive methodology was developed to quantify both the positive and negative radiative forcing (RF) effects of distributed urban rooftop PV deployment using a high-resolution approach. Earlier studies often rely on coarse-resolution satellite data, which cannot capture the spatial variance of distributed urban PV systems, or on simplified PV assumptions that may lead to inaccurate estimations of PV yield and albedo change. To address these limitations and to fill this research gap, this study introduced two novel simulation frameworks that leverage LiDAR data and geo-reference material maps. The first framework, based on geometric spectral albedo (GSA) model, simulates surface albedo change before and after PV deployment. The second framework, utilizing skyline-based PV model, performs large-scale rooftop PV simulation for annual yield calculation. Both frameworks were established to accurately calculate the radiative impacts of urban roof PV integration. The outputs were then translated into

positive and negative RFs to calculate the equilibrium time — the period required for the negative RF from PV electricity generation to fully offset the positive RF from albedo reduction.

The workflow was applied across a rectangular area covering the entire city of Delft. The hourly albedo result showed distinct patterns: on sunny days with clear skies, albedo peaks at sunrise and sunset hours but remains lower for the rest of the day. On overcast days, albedo stays relatively high and constant for the entire day. The annual GHI-weighted albedo was calculated and mapped to the selected area, presenting lower albedo values in urban areas and higher values in surrounding rural areas. This distribution can be attributed to the use of low-reflectivity materials commonly found in urban settings, which directly reduce surface albedo, as well as the greater roughness within urban environments, which traps more radiation and limits the amount of energy reflected back to space. The simulation results were validated with MODIS albedo products, showing a general agreement in albedo distribution patterns despite differences in absolute albedo values. Overall, around 90% of the map pixels from the GSA model lied in a deviation range of ±0.03 from the MODIS products. The average albedo simulated for the entire area was 0.1584 for the GSA model and 0.1493 for the MODIS product, leading to an absolute difference of 6.12%. This discrepancy could be attributed to several sources of uncertainty. From the GSA albedo model perspective, the main contributors were the limited assumptions in the classification of surface materials and the simplified geometric operations used to derive the shading profile. On the other hand, uncertainties in the MODIS albedo product came primarily from measurement data quality, the BRDF model that is less suited for spatially heterogeneous and temporally dynamic urban surfaces, and the complex urban geometry that responds varying surface reflections during the multi-day satellite observation period.

The annual PV energy yield was investigated under two scenarios: 1) all roof surfaces are integrated with PV; 2) only the roof surfaces meeting the specific yield threshold of 650 kWh/kW$_p$ are integrated with PV. In the first scenario, the total annual PV yield amounts amounted to 485.72 GWh/year, covering a roof area of 2.8289 km^2. In the second scenario, where only high-yielding roofs were integrated with PV, the yield was slightly lower at 434.82 GWh/year, with a covered roof area reduced to 2.2425 km^2. For both scenarios, the positive RFs due to rooftop PV integration are determined at 3.53×10^{-8} W/m^2 and 3.40×10^{-8} W/m^2, respectively. Together with the negative RF derived from the PV yield, the equilibrium time (ET) was found to be 39.2 and 42.0 days, assuming a grid carbon emission intensity of 437 g CO_2-eq/kWh. This ET is considered as remarkably short for mainly two reasons: first, this duration represents only less than 0.5% of typical PV module lifetime (25 to 30 years). This means that for over 99.5% of its operational lifespan, PV technology is contributing to the negative RF as long as it continues to displace fossil-fuel-generated electricity; second, compared to other renewable energies such as hydropower, this duration is significantly shorter. For example, a recent study found out that 43% of investigated hydropower plants achieve equilibrium within 4 years (around 5% of their estimated lifetime of 80 years), while 19% exceed 40 years, and 12% never reach equilibrium within their operational lifetime [144].

The cumulative negative RF from roof PV integration in Delft by the end of PV system's typical lifetime (between 25 to 30 years) was found to be 6.74 and 7.85 × 10^{-6}

W/m^2 for scenario one and 6.03 and 7.03 $\times$ 10^{-6} W/m^2 for scenario two, assuming a fixed carbon emission intensity and annual PV yield. These numbers are approximately 170 to 230 times larger than the initial positive RF caused by albedo reduction. This finding indicates that the reduction in greenhouse gas emissions facilitated by PV integration significantly outweighs the positive RF caused by the reduced albedo under current carbon-intensive energy infrastructure. However, as energy infrastructure continues to decarbonize with the increasing penetration of renewable sources, the carbon emission intensity of the grid declines accordingly. In a future scenario where electricity generation is predominantly based on renewables – and the grid's carbon intensity approaches that of current c-Si PV modules – the equilibrium time for a fully integrated rooftop PV system in Delft extends significantly, reaching 1548.5 days and 623.1 days under the 13 g and 30 g CO_2-eq/kWh scenarios, respectively. As the energy system becomes more sustainable and PV manufacturing emissions continue to decrease through technological advancements, the relative contribution of albedo-induced positive radiative forcing to net climate impact will become increasingly significant. This highlights the necessity to account for albedo effects in future life cycle assessments (LCA) of PV technologies to more accurately evaluate their global warming mitigation potential.

This study can be extended to other regions of the world as long as the digital elevation data and material class data are available. Therefore, this work aids in the high-resolution assessments of global albedo and its variation, and offers insights into the Earth's energy balance by examining both the positive and negative RFs caused by PV integration. These findings contribute to achieve a more realistic figure of climate change mitigation potential through PV technologies.

5

Multi-functional PV demonstrator

This chapter is based on the following publication:

Y. Zhou, A. Ibrahim, M. Muttillo, H. Ziar, O. Isabella, and P. Manganiello, *Investigation on simultaneous energy harvesting and visible light communication using commercial c-Si PV cells: Bandwidth characterization under colored LEDs*, Energy **311**, 133387 (2024). (DOI: https://doi.org/10.1016/j.energy.2024.133387)

5.1. Introduction

Internet of Things (IoT) connected devices have been seamlessly embedded into our daily lives, facilitated by the rapid development of diverse wireless communication technologies. The connectivity of these devices is dominated by means of wireless fidelity (WiFi), Bluetooth, and cellular networks which predominately communicate information through low radio frequency (RFreq) spectrum. A recent forecast suggests that the number of IoT-connected devices will double the current count, approaching thirty billion in 2030 [160]. Coupled with the rising user density due to population expansion and urbanization, a shortage in the available RFreq spectrum for communication is anticipated. Besides the escalating RFreq communication traffic, the demand for high-speed data transmission is another driving force that motivates researchers to explore higher frequencies for wireless communication. The wider bandwidth inherent in the higher frequency range significantly boosts the transmission data rate. This enhancement is essential for applications like space-to-ground links where a massive amount of data needs to be transmitted within a brief contact window [161]. From the perspective of urban environments, the advancements in autonomous vehicles and smart homes also necessitate high-speed communication to manage the immense data flows among IoT-connected devices in the future smart cities [162].

Although higher frequencies provide a promising avenue for wireless communication, their implementation comes with technical challenges. Electromagnetic waves, by

nature, experience energy density reduction as they propagate due to medium-induced attenuation. This effect is more prominent at higher frequencies, resulting in an increased path loss. Using higher frequencies is also more susceptible to obstacles including buildings and foliage in the urban environment, leading to shadow zones where signals are significantly weakened or completely absent [163]. To overcome these challenges, one approach suggests implementing LOS paths where the information is beamformed and directed along an unobstructed route between the receiver and transmitter to mitigate attenuation and blockage [164]. Another more widely acknowledged approach involves segmenting the communication into smaller cells so that stronger and more reliable signals are ensured within those confined regions [165]. However, developing such micro-communication units relies on the availability of widespread infrastructures. This requirement has prompted researchers to investigate the potential of visible light communication (VLC) systems that could be integrated with existing lighting infrastructure dominated by LEDs, that is, leveraging their extensive deployment. The additional communication channels introduced by the visible light spectrum not only complement the current wireless communication systems, effectively mitigating RFreq congestion, but also expand the bandwidth, thereby offering high-speed data transmission [166].

Typically, a VLC system consists of a light source (LED or LASER) as the transmitter and photodiodes (PDs) as the receiver [167]. During data transmission, the transmitter intensity is modulated at a high frequency, which in turn modulates the output current of PDs as the light strikes them. This varying current is subsequently translated into voltage signals with a trans-impedance amplifier and decoded to extract the information. The modulation frequency employed is usually much higher than the flicker fusion threshold, meaning that the primary lighting function of the LED infrastructure remains unaffected after integrating with the VLC systems, as the rapid flickering is imperceptible to human eyes [168]. In addition to its wider bandwidth and rapid deployment capabilities, VLC offers a few more advantages over traditional RFreq communication: firstly, visible light is unlicensed, making it freely available for broad development [169]; secondly, visible light cannot penetrate walls. While this limits signal coverage, integrating VLC into the LED infrastructure creates confined communication zones, enhancing security by reducing the risks of eavesdropping [170]; lastly, LEDs are energy-efficient, and their long lifespan contributes to a reduced maintenance cost [171]. As a specific application of VLC technology, Light Fidelity (LiFi) facilitates high-speed data transmission by complementing WiFi. The recent introduction of the IEEE 802.11bb standard helps accelerate its adoption, which sets the stage for enhanced interoperability in the wireless communication society [172].

Nevertheless, the extensive implementation of such technology still needs to resolve certain issues, and one of the bottlenecks is found at the receiver end. Despite its fast response time, high sensitivity, and wide bandwidth for optical signals, the frequency response of PDs deteriorates drastically when they are exposed to ambient light higher than 200 W/m^2 [173, 174]. This limits its communication performance in well-illuminated indoor environments and restrains its application under outdoor conditions. At the same time, PDs must be reverse-biased to function as light detectors, which necessitates a continuous external power supply.

As an effective solution, PV cells are gaining recognition for self-powered VLC receivers under high ambient light conditions. They are primarily engineered for outdoor operation, and the harvested energy can be utilized to power the entire communication system [175]. One of the first attempts of using commercial silicon PV cells for both communication and energy production was carried out by Kim et al. Their experiment successfully demonstrated VLC operation under strong sunlight irradiance of 800 W/m^2 [176]. Malik et al. developed a mini self-powered VLC system, which offers a bandwidth of 50 kHz and a maximum error-free data rate of 8 kb/s [177]. In a related study, Wang et al. investigated the feasibility of using a mini PV panel (24 × 18 cm^2) as the detector in an optical wireless communication (OWC) system. They tested both on-off keying (OOK) and orthogonal frequency division multiplexing (OFDM) modulated signals, achieving data transmission rates of 1 Mb/s and 11.84 Mb/s, respectively, while generating 2 mW of electricity [168, 178]. By employing a self-reverse-biased circuit to the PV panel, Shin et al. achieved an improved data rate of 17.05 Mb/s [179]. The potential of the underwater OWC system was demonstrated by Kong et al. where they successfully transmitted information from a laser diode through a 7-meter water tank to a solar panel at a rate of 22.56 Mb/s [180]. In 2019, Das et al. built the world's first OWC system using off-the-shelf lasers and silicon mini PV panel (3 × 2.5 cm^2), which harvested 5 W power while communicating at a data rate of 8 Mb/s [181]. The impact of sunlight on PVs as OWC receivers was further explored with a sunlight emulator, and a trade-off between energy harvesting and communication performance was reported. This means that while the PV output increases with solar irradiation, the data rate exhibits a contrary trend, decreasing as the solar irradiation intensifies [182].

Other research investigated using different PV technologies in VLC systems, where thin film amorphous silicon was demonstrated to support weak light detection (down to 10 mW/m^2), achieving a data rate of 1.2 Mb/s [183]. Organic PV (OPV) is a relatively new field in VLC, but it is gaining interest due to its ease of fabrication and tunable properties [184]. The very first investigation in using OPV as a photo-detector was carried out by Arredondo et al., where they demonstrated a bandwidth of 790 kHz based on P3HT:PCBM [185]. Another work done by Vega-Colado et al. realized a full-organic VLC system using off-the-shelf components and achieved a bandwidth of 200 kHz at 2 V of reverse bias [186]. Salamandra et al. developed the inverted P3HT:PCBM organic structure and achieved a bandwidth of 1.02 MHz at -1 V bias [187]. Although various approaches are being explored to improve the bandwidth, reverse biasing the OPV means the device is not generating power. One of the first studies of combining communication and energy harvesting using OPV was conducted by Zhang et al., and they revealed that using an OPV cell (0.2 × 0.4 cm^2) as the receiver enabled a data rate of 34.2 Mb/s and concurrently produced a power of 0.43 mW [188]. This outcome has been overtaken by a recent work where a remarkable data rate of 363 Mb/s was reached, with a 10.9 mW power output in a multi-input multi-output (MIMO) setup consisting of four OPV solar cells (0.25 × 0.4 cm^2) [189]. Mica et al. used a triple-cation perovskite PV cell as the photodetector and achieved a 56 Mb/s data rate under white LED [190]. One of the best communication performances was reported by employing gallium arsenide (GaAs) PV cells, where a maximum of 1 Gb/s data rate was attained when the PV cell was operating under short-circuit condition [191, 192].

While most of the research focuses on enhancing the data transmission speed, the fundamental relationship between the light source and different PV cell architectures is not systematically explored in the context of VLC. Therefore, the aim of this study is to fill this research gap by systematically exploring the communication performance of commercial PV cells with diverse architectures when they are utilized as VLC receivers. Additionally, three representative LED colors within the visible light spectrum are investigated in terms of their impact on the communication performance of commercial PV cells. The objective is to determine if a particular LED color demonstrates superior performance, which could inform future color filter design for PV cells to improve communication. In this work, the frequency response under various light intensities is characterized for each LED color and further conducted at different PV cell operating voltages to understand the dynamics between energy harvesting and data communication. c-Si PV cells are the primary focus due to their dominating position in the PV industry. These include architectures such as 5-inch aluminum back surface field (Al-BSF(5")), 6-inch Al-BSF (Al-BSF(6")), busbar-free Al-BSF (Al-BSF(BF)), passivated emitter and rear contact (PERC), interdigitated back contact (IBC), silicon heterojunction (SHJ), and tunnel oxide passivated contact (TOPCon), covering from the oldest to the newest c-Si PV technologies. It is worth mentioning that all the commercial PV cells are maintained in their original dimension for this study. Certainly, cell size plays a role in determining the capacitance and resistance of PV cells, where a larger cell size generally leads to higher capacitance and lower resistance [193]. But these parameters are also highly dependent on other factors, including the bulk doping concentration, emitter resistance, and the design of fingers and busbars [194]. This detailed architectural information of commercial solar cells is not readily available and cannot be easily extracted from measurements. Additionally, standardizing the cell size would require cutting all the commercial solar cells down to the same size, potentially introducing unexpected edge effects and leading to performance deviations [195]. To maintain the integrity of our study, we retained the original dimensions of all PV cells. This approach allows us to evaluate the energy harvesting and communication performance of off-the-shelf PV cells within the context of VLC without introducing unwanted performance degradation due to cell cutting. Keeping the cells in their original size also ensures that our results are directly applicable to consumer-grade products, providing valuable insights for both researchers and industry professionals.

5.2. Experimental setup

The PV cells are first laminated (hereafter referred to as PV laminates), and the lamination structure comprises a stratified assembly including, from top to bottom, a PV glass layer, an ethylene vinyl acetate (EVA) encapsulant layer, the PV cell, another EVA layer, and a white back sheet or a PV glass layer. These PV laminates are examined under three representative LED colors across the visible light spectrum, spanning from red to green and blue, with a maximum rated power of 100 W. The spectral distributions of the LEDs are measured with a spectrometer (SR-1901PT) and are presented in Figure 5.1, with their peak wavelength indicated in the legend [196]. The photos of the laminated commercial PV cells are shown in Figure 5.2, and their architectural information is detailed in Table 5.1. The characteristics of PV laminates under standard test conditions (air mass

1.5 spectrum, 1000 W/m^2 of irradiance, and cell temperature of 25 °C) are listed in Table 5.2. For each LED color, the PV laminates are tested at three irradiance levels: 100, 300, and 500 W/m^2. As the output current of solar cells is proportional to the incident light intensity, increasing the LED intensity will generate more current that flows through the system and brings up the temperature. The attached heat sink has a limited capacity to dissipate only a certain amount of heat. This limits the maximum LED intensity used in the measurement to prevent the components from overheating damage. Therefore, the maximum irradiance intensity is determined based on the heat dissipation capacity of the system's heat sink.

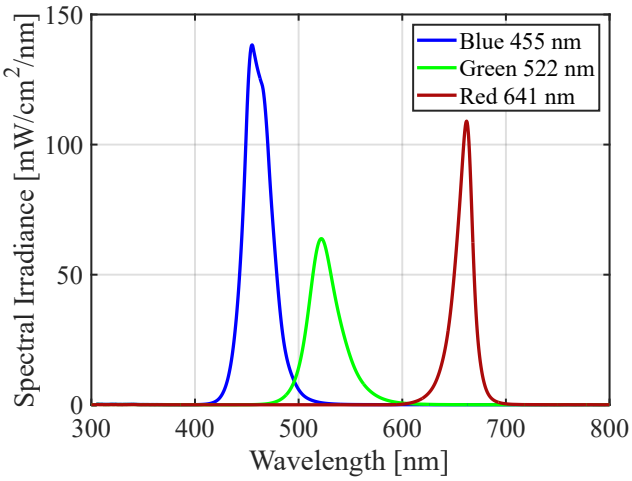

Figure 5.1: The measured spectra of blue, green, and red LEDs used in this study. The peak wavelengths are indicated in the legend, and show slight shifts from the values the manufacturer specifies (Blue: 463 nm; Green: 523 nm; Red: 655 nm).

Table 5.1: Architectural information of the c-Si PV laminates, with abbreviations: BB for busbar, SW for smart wire, and BC for back contact. The bulk doping concentration of tested commercial c-Si solar cells was determined by using C-V measurement [197].

PV Laminate [-]	Cell Size [-]	Area [cm^2]	Doping Concentration [atoms/cm^3]	Front-side Metal [-]	Back-side Metal [-]
Al-BSF(5")	Full-size	153.0	4.2×10^{14}	2BB	2BB
Al-BSF(6")	Full-size	244.3	1.1×10^{16}	3BB	3BB
Al-BSF(BF)	Full-size	244.3	1.0×10^{16}	19SW	4BB
IBC	Full-size	153.0	4.5×10^{14}	-	BC
PERC	Half-cut	126.0	2.6×10^{16}	9BB	9BB
SHJ	Full-size	244.3	5.6×10^{15}	22SW	22SW
TOPCon	Half-cut	126.0	4.5×10^{15}	9BB	9BB

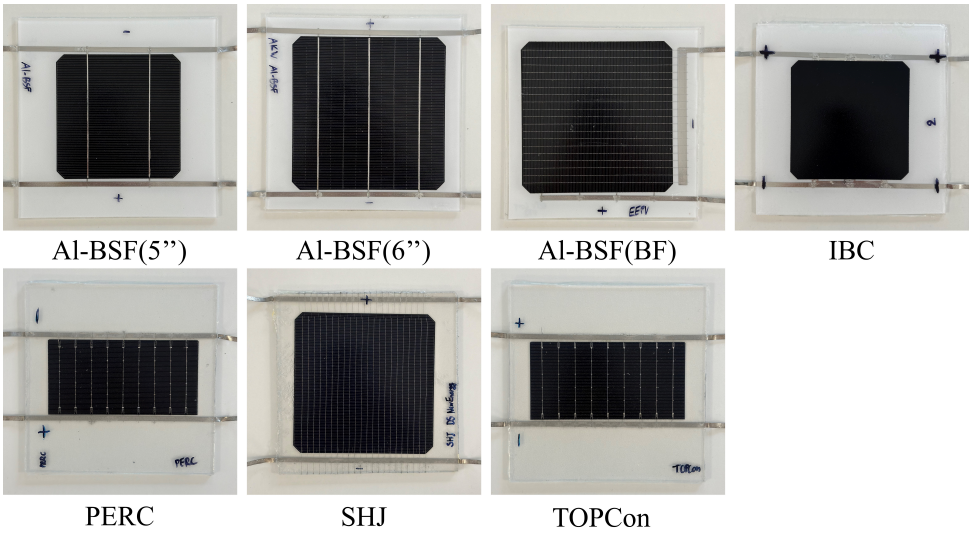

Figure 5.2: Photos of the commercial PV laminates used in this study.

Table 5.2: Key parameters of the c-Si PV laminates under standard test conditions (STC) obtained using a LOANA solar cell analysis system [198].

PV Laminate [-]	V_{oc} [V]	I_{sc} [A]	V_{mpp} [V]	I_{mpp} [A]	P_{mpp} [W]	η [%]
Al-BSF(5")	0.64	5.96	0.51	5.51	2.79	18.22
Al-BSF(6")	0.64	9.44	0.52	8.91	4.65	19.02
Al-BSF(BF)	0.64	9.44	0.51	8.86	4.48	18.33
IBC	0.68	6.46	0.56	5.98	3.39	22.14
PERC	0.69	4.94	0.59	4.71	2.76	21.93
SHJ	0.74	8.92	0.64	8.50	5.40	22.12
TOPCon	0.69	4.91	0.59	4.65	2.74	21.73

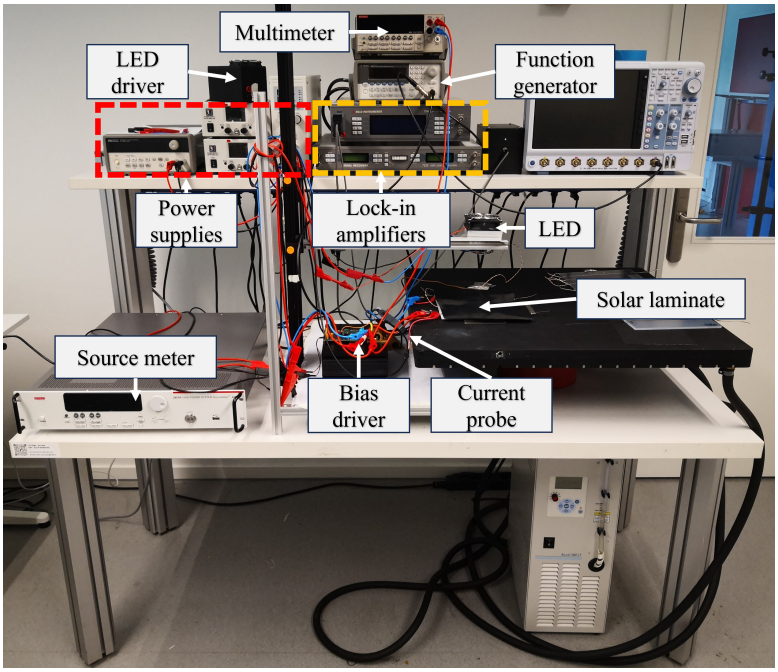

Figure 5.3: Experimental setup for I-V curve characterization and bandwidth measurement.

Figure 5.3 presents the experimental setup for the measurements. The measurement process can be divided into two primary stages. For each LED color and intensity setting, the I-V behavior of PV laminates is first characterized to identify their open-circuit voltage and maximum power point. Following this initial characterization, the PV laminates are biased at various operating voltages to perform the small-signal bandwidth measurement. The selection of operating voltage ranges and increments is guided by the outcomes of the I-V characterization. The measurement details of these two stages are elaborated in the subsequent two subsections.

5.2.1. I-V curve measurement of PV laminates

The I-V curves of PV laminates are measured in a 4-wire configuration with Keithley KickStart software and source meter (Keithley 2651A). A simplified diagram of this setup is depicted in Figure 5.4a. The light source consists of a matrix of LEDs. During the measurement, it is fitted with a collimator lens and placed 10 cm above the PV laminates to ensure a comprehensive and homogeneous illumination. By adjusting the output power of the LED, the targeted irradiance level is achieved, as indicated by the short-circuit current of PV laminates. This is due to the linear correlation between the incident light intensity and the short-circuit current produced by the PV laminates. The temperature of PV laminates is monitored with a Pico logger connected to a thermocouple attached to the rear side of the PV laminates. Once the temperature stabilizes, the I-V sweep is performed. The resultant I-V curve is plotted in Figure 5.4b in blue, which represents

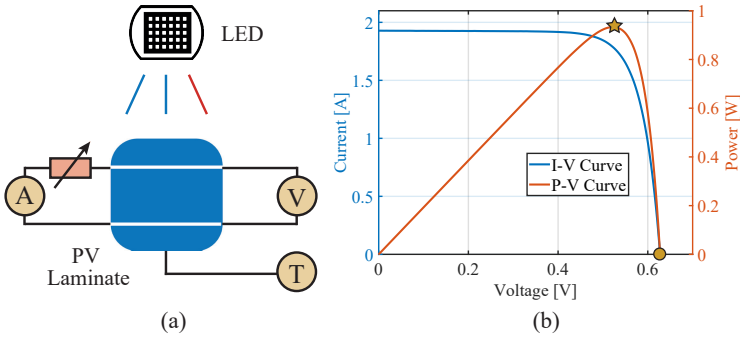

Figure 5.4: a) Diagram of the I-V characterization setup where the PV laminate is measured with a 4-wire configuration under different LED colors and intensities. The temperature of the PV laminate is monitored with a thermocouple attached to the back of the laminate, and all I-V sweeps are conducted after the temperature is stabilized; b) I-V and P-V characteristics of the IBC PV laminate under blue LED at 300 W/m^2 and 30 °C. Both the maximum power point and the open-circuit voltage are highlighted in the plot.

the case for IBC PV laminate under blue LED at 300 W/m^2 and 30 °C. As the voltage increases, it can be observed that the current decreases. The voltage at which the output current of PV laminate is zero is known as the open-circuit voltage (V_{oc}). Additionally, the power output of PV laminate as a function of the operating voltage is also depicted by the red curve in Figure 5.4b, where the power output first increases with the voltage to a peak, then it declines to zero. This peak represents the maximum power point (MPP), and it is the optimal operating point when PV laminate is used as an energy harvester. Measuring the I-V curve is an important step because it not only characterizes the electrical properties of PV laminate but the obtained V_{oc} and MPP are also essential to determine the operating voltage range for the subsequent small-signal frequency sweep. It is worth mentioning that the temperature effect is not considered in the analysis due to the absence of temperature control components in the setup. An increased temperature alters the I-V curve, leading to higher short-circuit current and lower open-circuit voltage, eventually reducing the solar cell's power output [75].

5.2.2. Bandwidth measurement of PV laminates

Figure 5.5 shows the diagram of the bandwidth characterization setup for the VLC system using c-Si PV laminates as the receiver. The transmitter circuit consists of a function generator (Agilent 33250A), a custom-made LED driver, and LEDs with a collimator lens. The receiver circuit comprises PV laminates, a self-made bias driver, a multimeter (Keithley 2000), and two lock-in amplifiers (EG&G 7260 and EG&G 7225). Both circuits are connected to a single laptop, which controls and processes the signals using in-house developed measurement software. It should be noted that all these setup components have relatively high bandwidth, thus, their contribution to the bandwidth measurement of PV laminates is negligible.

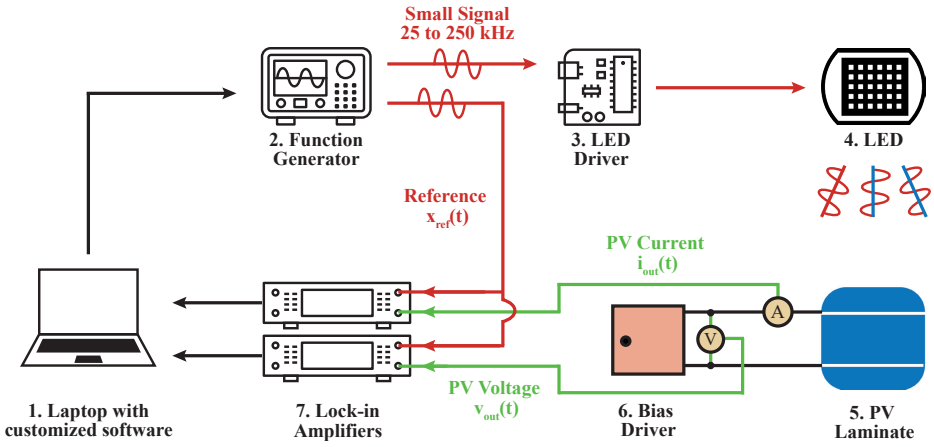

Figure 5.5: Bandwidth characterization setup for the VLC system when c-Si PV laminates are used as the receiver. The bias circuit is developed to set the operating voltage of PV laminates and it imposes a resistive load R_f in the AC circuit system.

5

The transmitter circuit

The transmitter circuit essentially controls the operation of the LED light source. The laptop sends the control signals, encompassing both DC and AC components, to the function generator. The function generator then relays the requisite composite waveform to the LED driver, which modulates the LED to operate in the desired manner. In this setup, the LED operates in a constant current (CC) mode, which is a preferred approach for driving high-power LEDs to prevent thermal runaway risks. By maintaining a constant current, the CC mode also helps ensure a stable light output and reduce chromaticity shift [199]. As mentioned in Section 5.2.1, the DC component is set according to the short-circuit current of PV laminates that changes linearly with the incident irradiance level. Superimposed on this DC baseline is a small sinusoidal AC signal with a peak-to-peak amplitude (V_{pp}) of 5 mV, resulting in a light intensity change of around 1 W/m^2. The frequency variation ranges from 25 to 250 kHz, where the maximum frequency of this range is determined by the input frequency limit of the lock-in amplifier. It is worth mentioning that in the current setup, LEDs serve a dual role as both a light source and a transmitter. In practical scenarios, the solar cells are exposed to ambient light for electricity generation. Particularly in outdoor applications, the PV modules are subject to the solar spectrum, which can introduce unexpected noises during data transmission. In future iterations of the setup, a solar simulator can be incorporated to provide the PV laminates with consistent exposure to a solar spectrum, while LEDs are exclusively used for data transmission.

The receiver circuit

The receiver circuit essentially extracts the frequency response signal from the PV laminate outputs. This dynamic behavior of PV laminates is modeled with a small-signal AC equivalent circuit, as shown in Figure 5.6, with a current source representing the dy-

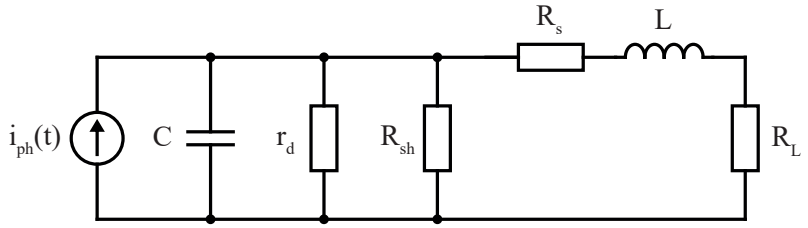

Figure 5.6: The small-signal AC equivalent circuit of a PV laminate connected to a load resistance under illumination [200].

namic photo-generated current i_{ph} at a certain time instance. The diode component in the DC equivalent circuit of solar cells is translated into a combination of capacitor and dynamic resistor, allowing for a detailed analysis of the dynamic behavior of solar cells under small-signal AC conditions. Besides the series resistance R_s and shunt resistance R_{sh} of the PV laminates, an additional voltage-dependent internal dynamic resistance r_d is included. The capacitance effect of the PV laminate is modeled with a capacitor C, and the inductor L represents the inductance due to the PV cell's metalization and its interconnection with the load resistance R_L.

During the frequency sweep, the bias driver first sets the operating voltage of the PV laminates to simulate various levels of power output. The range for adjusting the operating points is determined from the previous step of I-V measurement, and both the operating voltage and illumination level are fixed at each frequency sweep, meaning that the bandwidth is characterized after the PV laminate has reached charge distribution equilibrium [201, 202]. At each operating voltage, the frequency sweep is performed where the modulated LED illuminates the PV laminate. In response to the varying light intensity, the PV laminate shifts its I-V characteristics accordingly. These shifts are relatively subtle, as the amplitude of the AC signal is very small compared to the DC baseline. Such tiny variations in the PV output are buried in the system noises, therefore, lock-in amplifiers are employed to extract this small-signal AC information. In this setup, both the AC PV voltage and current outputs are measured. The AC PV voltage is directly read with a voltage probe connected to one of the lock-in amplifiers, while the AC PV current is first converted using a current probe (YOKOGAWA DLM5038) before being fed into the other lock-in amplifier. For both lock-in amplifiers, the peak-to-peak signal at low frequency (25 Hz) is adopted as the reference signal (X_{ref}), and the signal gain at various modulation frequencies f is calculated by the following equation:

$$Gain(f) = 20log_{10}\frac{X_{out}(f)}{X_{ref}} \tag{5.1}$$

where $X_{out}(f)$ is the peak-to-peak voltage or current signal at each frequency under a specific operating point. Since PV laminates act as low-pass filters for the received small light signals, the frequency at -3 db gain (also known as the cut-off frequency f_c) with respect to the global peak is the bandwidth [197]. This measurement enables the determination of bandwidth for all the PV laminates, which are biased at different operating

points and subject to various LED colors and intensities.

5.3. Methodology

To evaluate the bandwidth accurately, it is important to process and compensate the measurement data. This adjustment addresses two primary sources of deviation in the results: the ballast resistance found in the bias driver and the inductance in the system that causes resonance.

5.3.1. Offset the ballast resistance in bias driver

The bias driver acts as a resistive load to configure the operating point of the PV laminate as introduced in Section 5.2.2. However, this bias driver does not perform as an ideal variable resistor due to the presence of a fixed one-ohm ballast resistance R_f in series. While this ballast resistance is essential to stabilize the PV output signal, enabling a successful measurement, it also deviates the measured bandwidth from the true values. For a clearer understanding, the bandwidth f_c of an RC low-pass filter tailored for this specific scenario is shown in the equations below:

$$f_c = \frac{1}{2\pi RC} \tag{5.2}$$

where

$$R = (r_d \parallel R_{sh}) \parallel (R_s + R_L + R_f) \tag{5.3}$$

When the PV laminate operates at high voltages, the load resistance R_L dominates the bias driver resistance, meaning that the impact of R_f on the measured bandwidth is negligible. In contrast, at low operating voltages, R_f is comparable with R_L. Thus, its impact on the measured bandwidth becomes significant, which leads to a reduced bandwidth according to Equation 5.2. To offset the effect of the additional ballast resistance, the measured bandwidth needs to be compensated by considering the resistance R' that excludes the contribution of R_f. The corrected bandwidth, denoted as f_c', is calculated by the following equation:

$$f_c' = \frac{1}{2\pi R'C} \tag{5.4}$$

Assuming the capacitance C remains unchanged, this expression can be refined by substituting Equation 5.2 and becomes:

$$f_c' = \frac{R}{R'} f_c \tag{5.5}$$

where

$$R' = (r_d \parallel R_{sh}) \parallel (R_s + R_L) \tag{5.6}$$

R_s is the series resistance of PV laminates extracted by fitting the measured I-V curve with the double-diode model of PV cells [203]. R_L is the imposed load resistance depending on the operating point. $(r_d \parallel R_{sh})$ can be obtained from the external dynamic resistance R_D [204]:

$$R_L = V_{op} / I_{op} \tag{5.7}$$

$$R_D = \Delta V / \Delta I = (r_d \parallel R_{sh}) + R_s \tag{5.8}$$

where V_{op} and I_{op} are the voltage and current of the PV laminate at the operating point. $\Delta V / \Delta I$ is the inverse of the slope of the measured I-V curve at the given operating point.

5.3.2. Include the inductance-induced resonance

The bandwidth obtained by removing the ballast resistance does not account for the effect of inductance. This inductance mainly comes from the metallization and interconnections of PV laminates, with the former playing a dominant role. Its presence can make the system oscillate, and the frequency at which this oscillation happens is the resonant frequency, which can be calculated by the following equation:

$$f_r = \frac{1}{2\pi\sqrt{LC}} \tag{5.9}$$

Given that the bandwidth is the first frequency at which the gain drops below -3 dB, it is important to identify whether this reduction is attributed to the resonant frequency or the cut-off frequency that occurs first. Failing to identify the actual scenario could lead to an overestimation of the system bandwidth, especially at low PV operating voltages where the influence of inductance is significant. Under such conditions, the system bandwidth could be dictated by the resonant frequency, which typically falls below the corresponding RC circuit cut-off frequency. To adjust for this and determine the bandwidth accurately, the correction after considering the inductance-induced resonance is mainly performed by comparing the bandwidths derived from Equation 5.4 for the cut-off frequency and Equation 5.9 for the resonant frequency, where the lower of these two values is selected as the true bandwidth of the PV laminate. This condition can be exclusively expressed in terms of the damping ratio:

$$\zeta < \frac{1}{2} \tag{5.10}$$

Upon determining the inductance, the damping ratio is examined for each frequency sweep measurement result, and the bandwidth is corrected for the instances that satisfy the condition. Here, the inductance is considered as independent of the operating voltages, as the change caused by which is negligible [197]. For more information regarding the determination of the damping ratio condition and the inductance, please refer to 5.6, an appendix section of this chapter.

5.4. Results and discussion

In this section, the bandwidths of PV laminates under different measurement conditions are presented, focusing on the interplay between two key parameters of the PV laminates: the operating voltage, indicative of the energy harvesting ability, and the bandwidth, which reflects the communication performance. The bandwidth can be measured for both PV current and PV voltage. Here, the voltage bandwidth is primarily explored due to two considerations: first, the voltage bandwidth mirrors the behavior

of the current bandwidth, and they show close bandwidth results across the measurements; second, using voltage modulation is aligned with practical application, whereas using current modulation necessitates an additional conversion step from current to voltage [205].

5.4.1. Bandwidth vs PV operating voltages

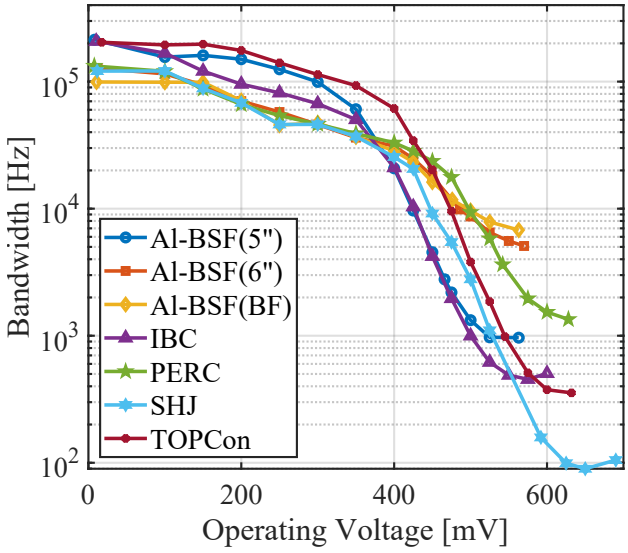

Figure 5.7: Voltage bandwidths of PV laminates with respect to the operating voltages under blue LED at 100 W/m^2.

Figure 5.7 shows the voltage bandwidths of PV laminates with respect to various operating voltages (from short-circuit to open-circuit) under blue LED at 100 W/m^2. As the operating voltage increases, a consistent decrease in the bandwidth is observed across all PV laminates, and two distinct variation regions are identified. In the low operating voltage range (< 350 mV), the bandwidth declines gently with increasing operating voltages, while it ramps down exponentially in the high operating voltage range. Such behavior is observed under all measurement conditions, and it can be primarily attributed to the change in the internal capacitance of PV laminates. Figure 5.8 illustrates the change of PV capacitance in response to the operating voltage increase. It is evident that in the low operating voltage range, the PV capacitance exhibits minimal change, indicating a dominant influence of depletion capacitance. As the operating voltage continues to increase, the diffusion capacitance becomes the primary driver and determines the exponential increase of the overall capacitance of PV laminates [197, 201]. This result indicates that the higher PV output power is achieved at the expense of communication bandwidth. Therefore, a trade-off exists between energy harvesting and communication when PV cells are used as VLC receivers.

Figure 5.9 shows a comparative summary of the voltage bandwidths of the individual

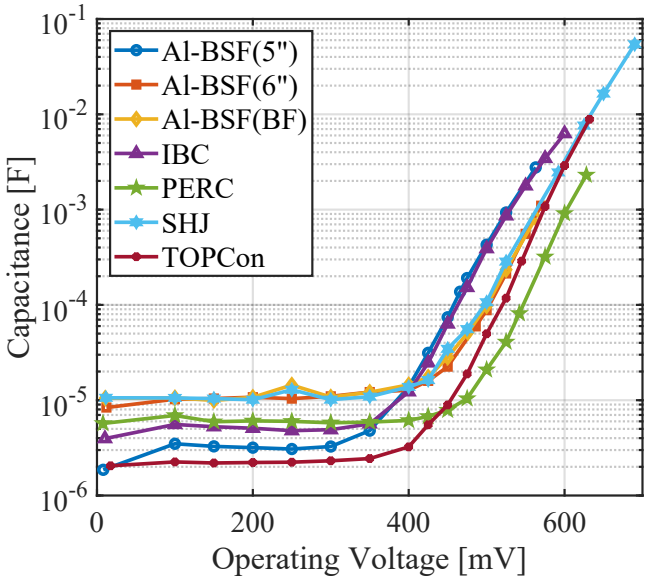

Figure 5.8: Capacitance of PV laminates with respect to the operating voltages under blue LED at 100 W/m^2.

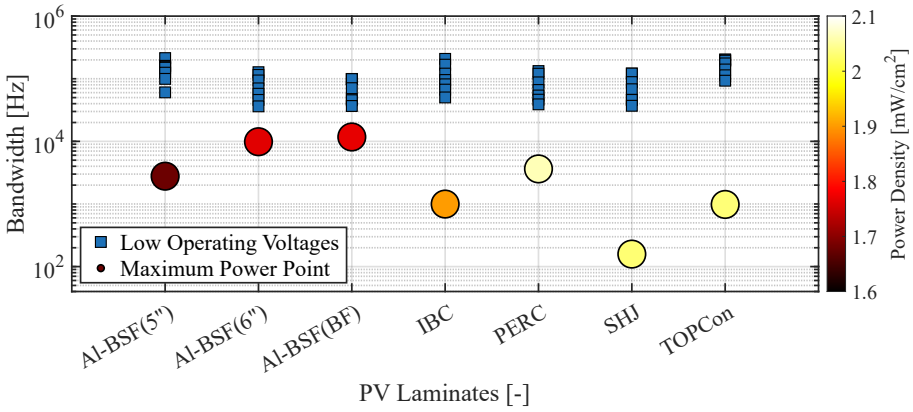

Figure 5.9: Voltage bandwidths of PV laminates obtained at low operating voltages and maximum power points under blue LED at 100 W/m^2, represented by blue squares and colored circles, respectively. The circle color indicates the magnitude of the power density the PV laminate delivers at the maximum power point.

PV laminates. This comparison includes the bandwidths obtained at the low operating voltage range (marked by blue squares) and at the maximum power point (indicated by colored circles). Additionally, the power density that PV laminates deliver at maximum power point is represented through a color scale with a corresponding color bar. It can be observed that all PV laminates exhibit a notably higher bandwidth at low operating voltages, with their values falling within a comparable range (30 kHz to 200 kHz). Particularly, Al-BSF(5"), IBC, and TOPCon PV laminates present slightly higher overall bandwidth, meaning that they are more advantageous in communication when working at low operating voltages. In contrast, when the PV laminates are optimized for energy harvesting, the bandwidths at the maximum power point scatter across a broad spectrum. Specifically, Al-BSF(6") and Al-BSF(BF) laminates demonstrate the highest bandwidths (9.8 kHz and 11.7 kHz, respectively) but are subject to lower power output. Conversely, with a higher power density, the SHJ PV laminate shows the least favorable communication performance, with the bandwidth limited to only 0.2 kHz. The PERC laminate outperforms others in power generation while maintaining a reasonable communication bandwidth. Meanwhile, it can also be concluded that the bandwidth variation range of both Al-BSF(6") and Al-BSF(BF) laminates is narrower than that of others in response to the operating voltage increase. This suggests that they can achieve higher output power with less compromise in communication performance. The underlying cause of this behavior can be attributed to the differences in cell architecture and material properties, such as wafer dopant concentration, which dictate the dynamic response of PV laminates [197].

5.4.2. Bandwidth vs irradiance levels

Figure 5.10 shows the voltage bandwidth of PERC laminate as a function of the operating voltages under blue LED at 100, 300, and 500 W/m^2. A distinct operating voltage window with a notable bandwidth difference can be identified where the PERC laminate exhibits higher bandwidths under higher irradiance levels. Beyond this specified window, the bandwidths present a marginal difference. This pattern appears to be minimally influenced by the capacitance, as depicted in Figure 5.11a, where the laminate capacitance shows only a slightly higher response under higher irradiance levels. The primary determining factor can be attributed to the larger resistance R' of the laminate under low light conditions [206]. As demonstrated in Figure 5.11b, the resistance under low irradiance levels remains constantly higher across the entire operating voltage range, and its impact on the bandwidth is more pronounced at low operating voltages where depletion capacitance dominates over diffusion capacitance. Meanwhile, the increased resistance under low-light conditions leads to an overdamped system, resulting in a bandwidth decline at lower operating voltages. For instance, the bandwidth of PERC laminate begins to decrease at 150 mV under 100 W/m^2, in contrast to 300 mV under 300 W/m^2. Therefore, it can be concluded that the irradiance level has minimal impact on the communication performance when the solar laminate is working at the maximum power point for optimized energy harvesting, but a higher irradiance level is preferred when the solar laminate is operating at voltages below the MPP yet distant from the short-circuit condition due to better communication performance. Figure 5.12 presents the voltage bandwidth of the remaining PV laminates changing with the operating voltages under

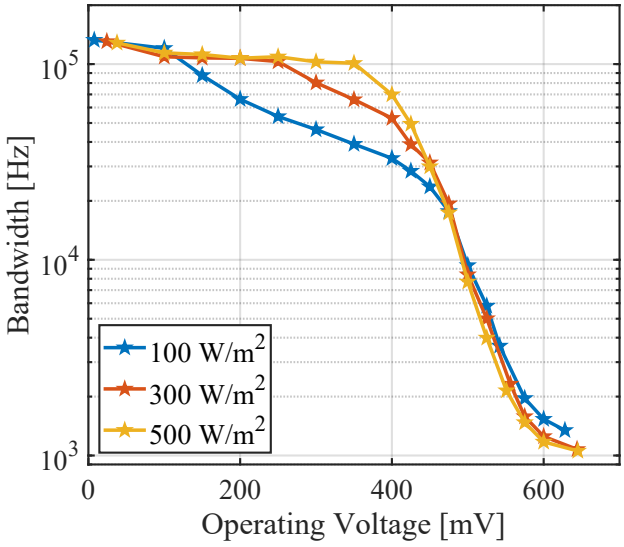

Figure 5.10: Voltage bandwidths of PERC laminate with respect to the operating voltages, measured under blue LED at 100, 300, and 500 W/m^2.

different irradiance levels, and a similar trend is observed. It is worth noting that Al-BSF(6"), Al-BSF(BF), and SHJ PV laminates are only measured up to 300 W/m^2 due to the heat dissipation capacity of the bias driver. Similar conclusions can be drawn for other LED colors under the same measurement conditions, suggesting that the impact of light intensity on the communication performance of solar laminates under test is independent of the LED colors.

5.4.3. Bandwidth vs LED colors

In fact, the effect of LED color on the communication performance of PV laminates is found to be minimal, as depicted in Figure 5.13 where the voltage bandwidth of PERC laminate presents a consistent response across the entire operating voltage range under blue, green, and red LEDs configured at 100 and 300 W/m^2. Although the blue LED marginally outperforms the red LED in the low operating voltage range under 100 W/m^2 illumination, the variance is relatively minor. At the maximum power point, the bandwidths are nearly the same with negligible difference. Moreover, as the irradiance level increases, the difference in bandwidth becomes even more insignificant. This trend is consistently observed for all the other PV laminates, as shown in Figure 5.14. Therefore, from the receiver's perspective, the color of the light source appears to have a limited impact on the communication performance. This uniformity can be advantageous to the integration of wavelength division multiplexing (WDM) with LEDs, ensuring that none of the channels will become a bottleneck. The consistent bandwidth performance across the RGB colors also simplifies the color filter design when multiple PV cells are used for signal separation and demodulation [207]. However, when considering the efficiency of

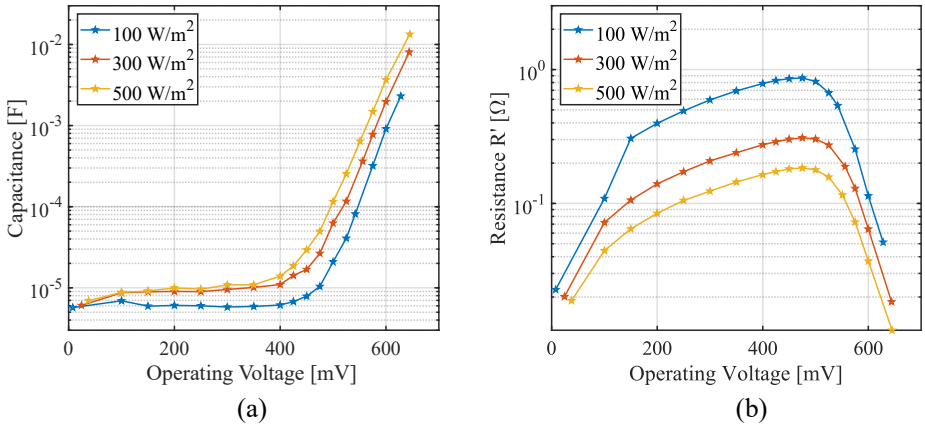

Figure 5.11: a) The capacitance of PERC laminate changing with the operating voltage under blue LED at 100, 300, and 500 W/m^2; b) The resistance R' of PERC laminate changing with the operating voltage under blue LED at 100, 300, and 500 W/m^2.

LEDs, using blue LEDs is found to be more advantageous due to their higher energy efficiency [208]. In other words, blue LEDs in a PV-based VLC system would consume less energy than red LEDs to achieve comparable levels of communication performance and energy harvesting. Red LED, by contrast, is preferred in the system where relatively long-distance communication is required due to less atmospheric attenuation while traveling [209].

5.4.4. Bandwidth vs architecture of commercial c-Si PV cells

The architectural impact of PV cells on bandwidth can be investigated through the bulk doping concentration and the metallization design. These properties are crucial in determining the capacitance and resistance of tested PV cells, particularly given that their available information is limited. Figure 5.15 shows the voltage bandwidth of PV laminates at both the short-circuit condition and the maximum power point under blue LED at 300 W/m^2. The PV laminates along the X axis are reorganized to incorporate the magnitude of doping concentration, where from left to right, it increases from the lowest (Al-BSF(5")) to the highest (PERC). Under the short-circuit condition (indicated by blue circles), higher doping concentrations tend to result in lower bandwidths. This effect is primarily attributed to the increased depletion capacitance associated with heavier doping profiles. Notably, two outliers are observed, where PV laminates IBC and Al-BSF(BF) exhibit significantly higher or lower bandwidths compared to adjacent cases. This behavior can result from the difference in series resistance as shown in Figure 5.16. With nearly identical doping concentrations, the series resistance of IBC laminate is half that of the Al-BSF(5") laminate owing to its optimized metallization layout, which leads to a higher bandwidth. Although the series resistance of TOPCon is even lower than that of IBC laminate, its doping concentration is one order of magnitude higher than that of the latter, resulting in a higher depletion capacitance and thereby bringing down the band-

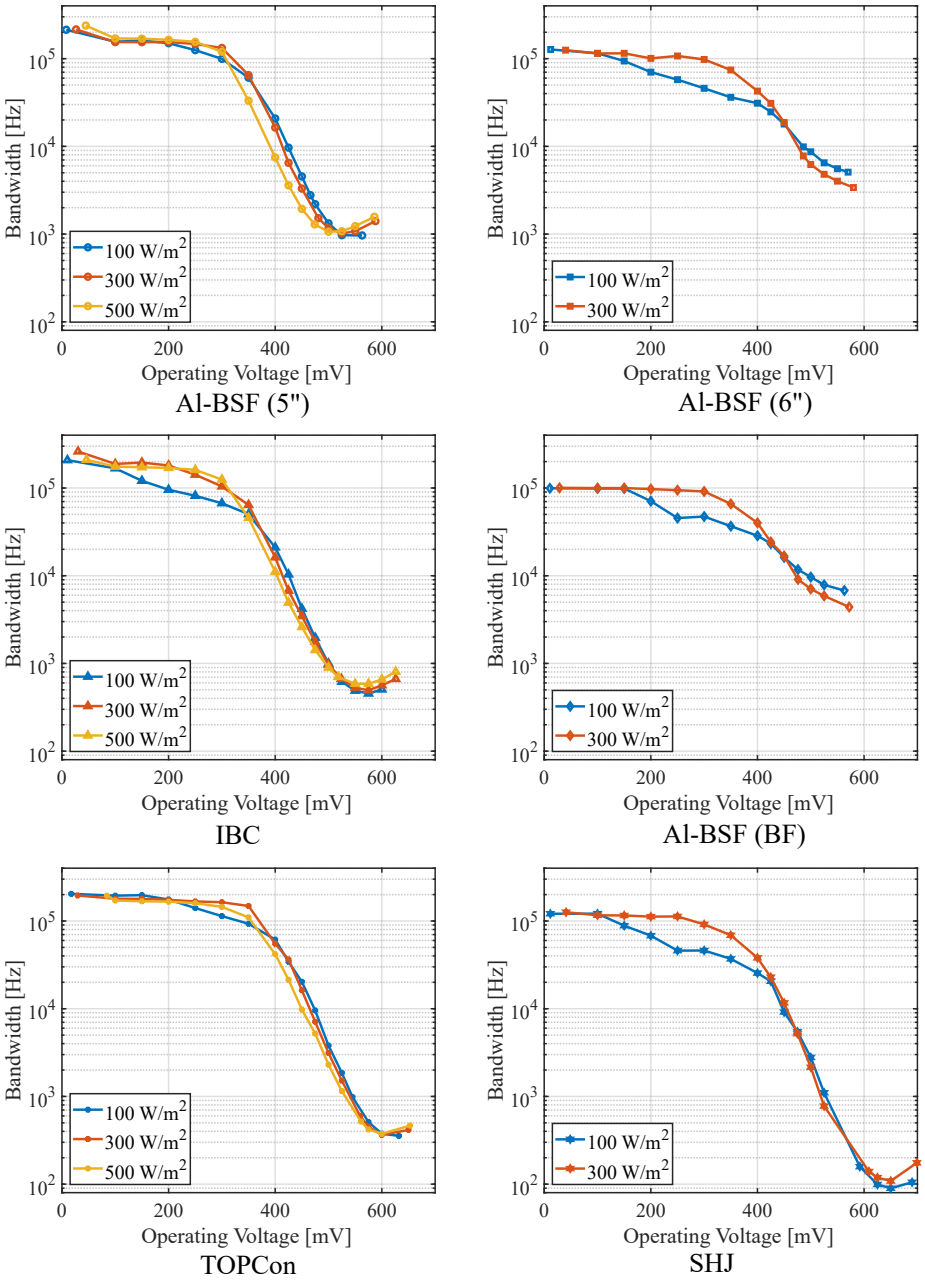

Figure 5.12: Voltage bandwidth of the remaining PV laminates as a function of operating voltage under blue LED at 100, 300, and 500 W/m^2.

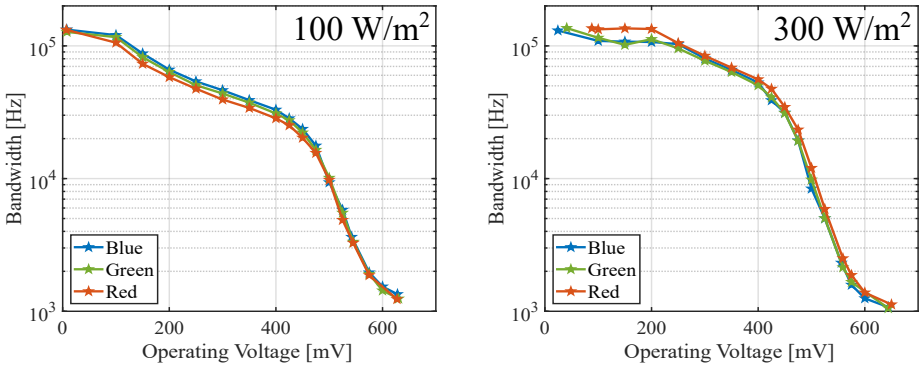

Figure 5.13: Voltage bandwidth of PERC PV laminate under blue, green, and red LEDs at 100 and 300 W/m^2.

width. This mechanism also applies to SHJ, Al-BSF(BF), and Al-BSF(6") PV laminates. Therefore, for VLC applications under short-circuit conditions, it is preferred to use PV laminates with lower doping concentration and lower series resistance achieved from an optimal metallization design.

The bandwidths at the MPP of each PV laminate (indicated by red hexagrams) do not show a clear trend as the doping concentration increases. This variability happens because the PV laminates are biased at their own MPP voltage, which differs from cell to cell. These varying voltages can significantly alter the diffusion capacitance and overall resistance, leading to irregular bandwidth results observed in Figure 5.15. To provide a more insightful comparison among PV laminates, Figure 5.17 plots the bandwidths of PV laminates with each color bar representing the bandwidths at operating voltages from 450 to 550 mV displayed from top to bottom. The bandwidths at 475 mV are connected by a black line. Unlike the results at MPP, the bandwidths of PV laminates under the same bias voltages present a more obvious pattern. Within the high operating voltage range, the bandwidth tends to be higher for the PV laminates with higher doping concentrations. This effect is mainly due to the lower diffusion capacitance of the PV laminates with higher doping concentrations. Opposite to the short-circuit conditions where higher doping concentration results in increased depletion capacitance, the diffusion capacitance under high operating voltage range is reversely associated with the doping concentration; in other words, higher doping concentration leads to lower diffusion capacitance [197]. Notably, TOPCon PV laminate shows higher bandwidth because its series resistance is much lower than that of SHJ despite having a close doping concentration. Therefore, for VLC applications around MPP, it is preferable to use PV laminates with high doping concentration and low series resistance.

Based on the above observations, optimizing the metallization design for a lower series resistance is clearly beneficial for both energy harvesting and communication. Since PV cells typically operate at MPP to maximize their energy production, increasing the doping concentration is advantageous to achieve a higher bandwidth around MPP, provided it does not adversely affect the conversion efficiency of PV cells. In theory, PV modules composed of these PV cells should maintain the same bandwidth because con-

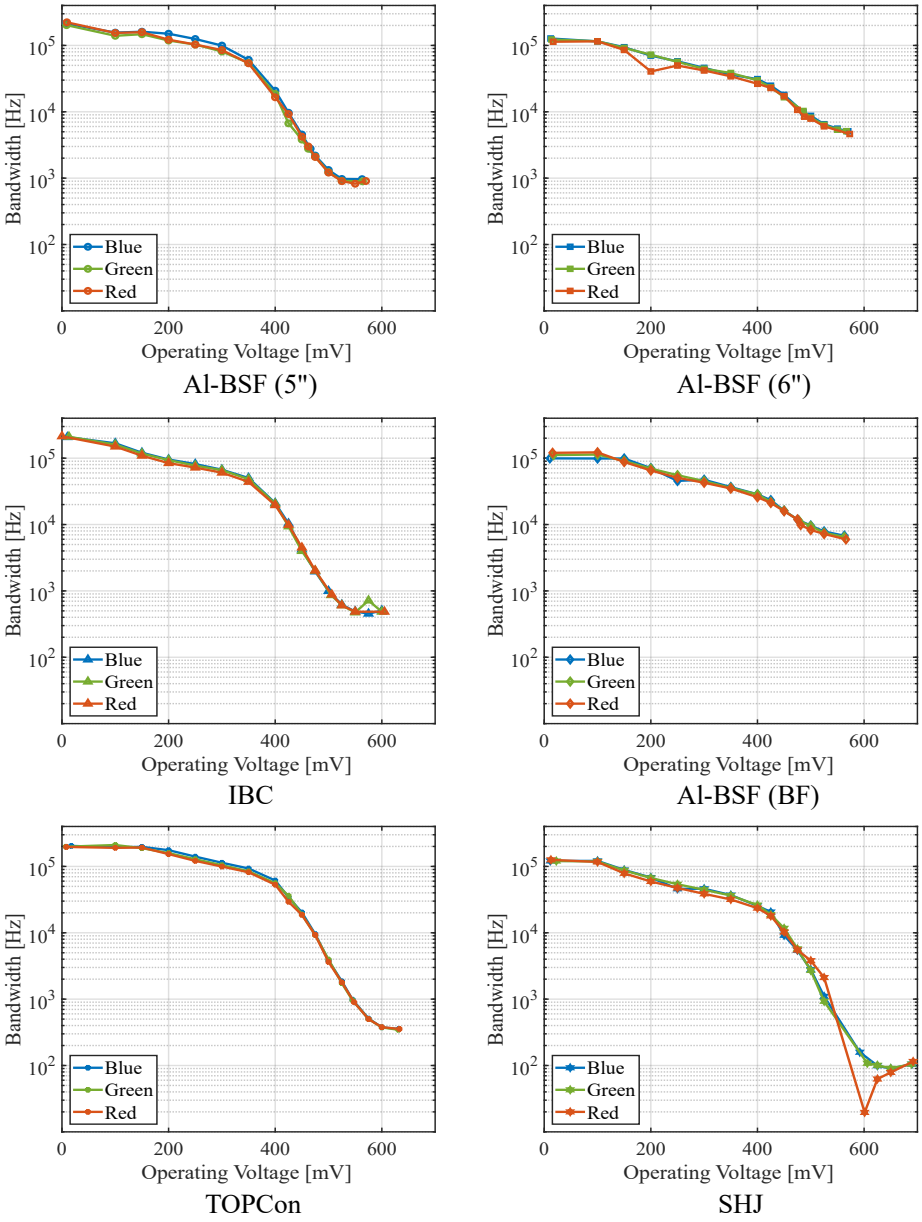

Figure 5.14: Voltage bandwidths of the remaining PV laminates as a function of the operating voltage under blue, green, and red LEDs at 100 W/m^2. The outlier in SHJ PV laminate at 600 mV could result from measurement error.

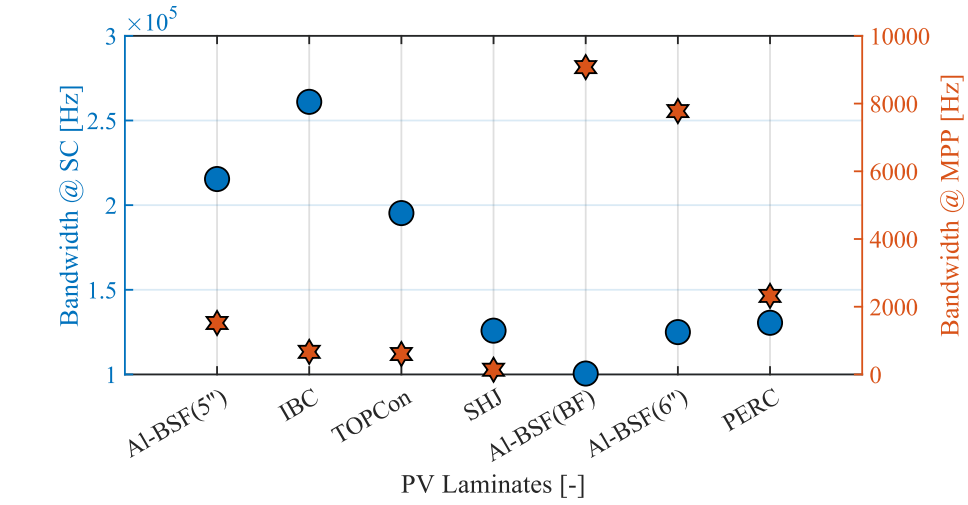

Figure 5.15: Voltage Bandwidth of PV laminates at short-circuit condition (blue circles) and maximum power point (red hexagrams) under blue LED at 300 W/m^2. The doping concentration of PV laminates increases from left to right, where Al-BSF(5") has the lowest doping concentration and PERC has the highest.

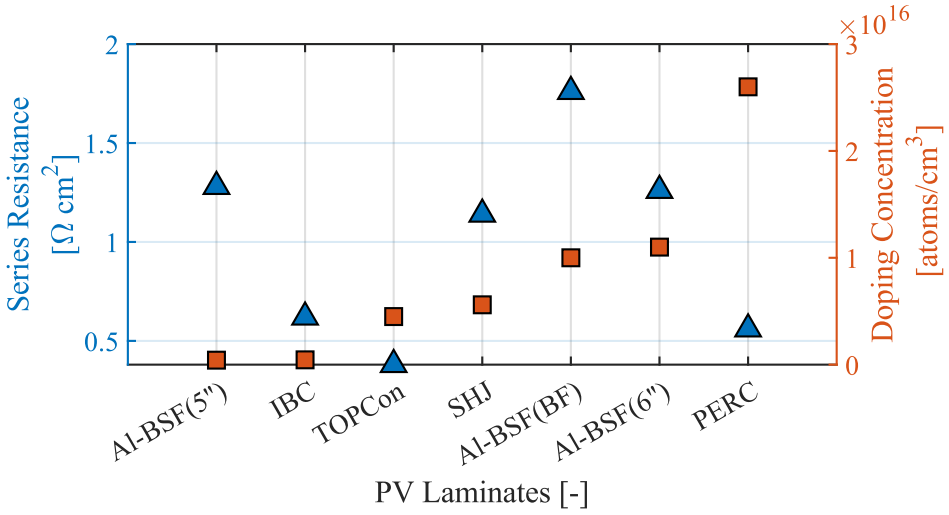

Figure 5.16: Series resistance and doping concentration of PV laminates, where the series resistance is extracted from the I-V measurement under blue LED at 300 W/m^2. The doping concentration of PV laminates increases from left to right, where Al-BSF(5") has the lowest doping concentration and PERC has the highest.

necting the cells in series proportionally reduces the overall capacitance and increases the overall resistance, which effectively cancels out their individual impact on the bandwidth. However, the additional metallization required for the cell interconnection and the junction box can introduce extra resistance to the system, which could eventually lead to a lower bandwidth at the module level.

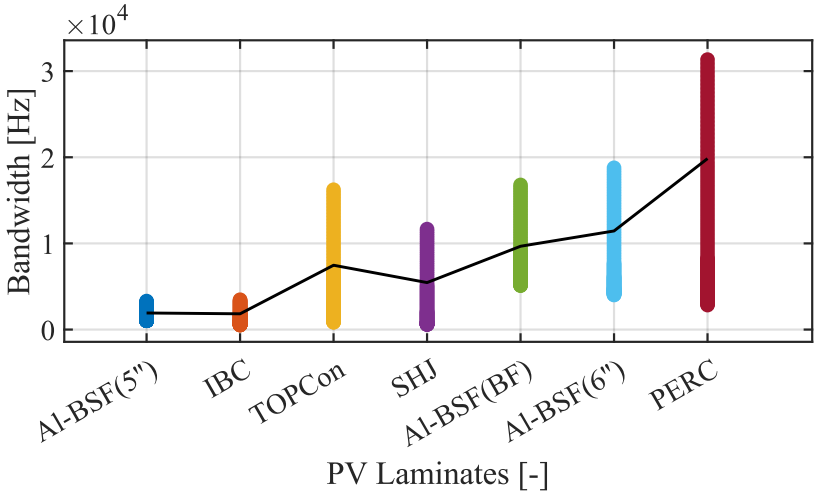

Figure 5.17: Bandwidths of PV laminates with each color bar representing the bandwidths at operating voltages from 450 to 550 mV displayed from top to bottom. The bandwidths at 475 mV are connected by a black line, and it shows an ascending trend as the doping concentration increases from left to right, where Al-BSF(5") has the lowest doping concentration and PERC has the highest.

5.4.5. Trade-off between energy harvesting and communication

To get a better insight into the trade-off between energy harvesting and communication in a PV-based VLC system, Figure 5.18 illustrates the relationship between the bandwidth of PV laminates and their power output under the given illumination conditions. This reaffirms that the improvement in communication performance often comes at the expense of reduced power output. Notably, the bandwidth response of Al-BSF(6") and Al-BSF(BF) PV laminates is more resilient to the increase in output power, implying that achieving comparable increases in the ratio of output power requires relatively smaller sacrifice in the bandwidth. In contrast, the SHJ PV laminate exhibits the least favorable bandwidth response against the output power. As compared in Figure 5.19, the SHJ PV laminate experiences a significant power decrease to achieve a bandwidth of 70 kHz, losing 40% of its maximum power output. Meanwhile, Al-BSF(5") and Al-BSF(BF) PV laminates are able to retain nearly 80% of their maximum power output when operating under similar bandwidth. This makes them the most suitable c-Si PV cell architecture in the VLC system in terms of individual trade-off between energy harvesting and communication, that is, when the system is optimized for its overall communication stability.

Given the tradeoff between energy harvesting and communication, that is, maximizing energy harvesting comes at the expense of communication performance and vice

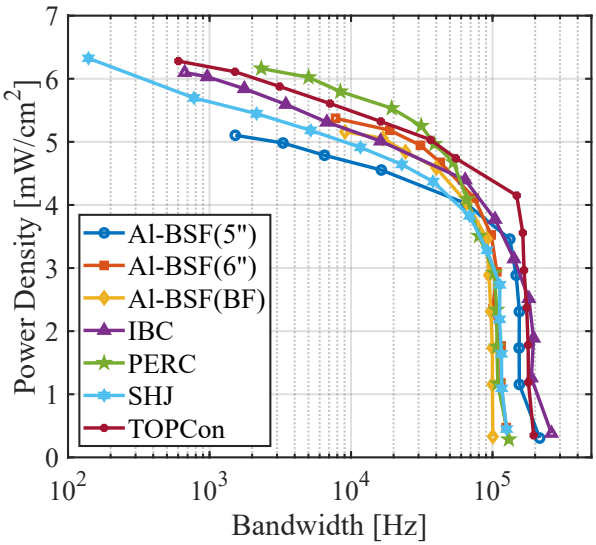

Figure 5.18: Voltage bandwidths of PV laminates versus their power output under blue LED at 300 W/m^2.

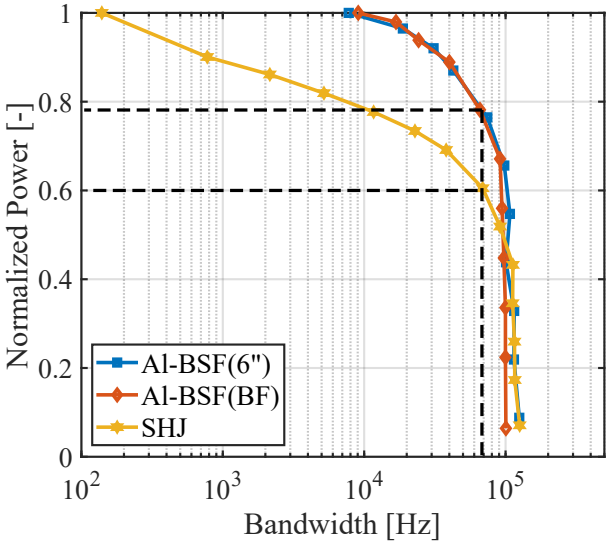

Figure 5.19: Voltage bandwidths of Al-BSF(5"), Al-BSF(BF), and SHJ PV laminates versus their normalized power output under blue LED at 300 W/m^2. To achieve the same bandwidth, SHJ loses 40% of its output power, whereas the other two laminates can still deliver 80% of their maximum power.

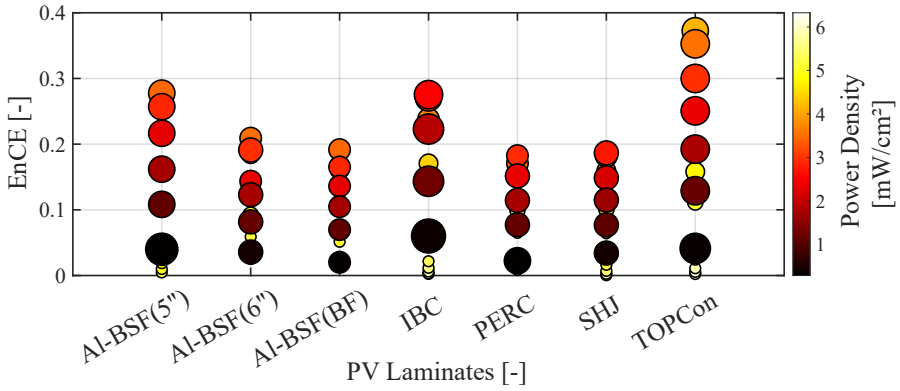

Figure 5.20: The EnCE for tested PV laminates under blue LED at 300 W/m^2. The color bar denotes the scale of power density, and the size of the circle represents the scale of normalized bandwidth.

Table 5.3: Bandwidth and power density of all PV laminates at Pareto optimality, along with their normalized power density (nPD) and normalized bandwidth (nB).

PV Laminate [-]	Bandwidth [kHz]	Power Density [mW/cm^2]	nB [-]	nPD [-]
Al-BSF(5")	132.5	3.5	0.51	0.55
Al-BSF(6")	97.9	3.5	0.38	0.56
Al-BSF(BF)	91.4	3.5	0.35	0.55
IBC	180.6	2.5	0.69	0.40
PERC	103.0	2.9	0.39	0.46
SHJ	112.7	2.7	0.43	0.43
TOPCon	148.2	4.1	0.56	0.65

versa, the Pareto optimality emerges as a compelling indicator to assess the overall performance of PV-based VLC systems [210]. This concept provides valuable insights into the solution that represents the best possible compromise between conflicting objectives, where in the context of a PV-based VLC system, this solution reveals the optimal tradeoffs. A novel parameter, Energy-Communication Efficiency (EnCE), is introduced to identify the Pareto optimality. This parameter essentially is the product of normalized power density (nPD) and normalized bandwidth (nB), each calculated against the maximum power density (6.3 mW/cm^2) and bandwidth (261 kHz) recorded among all PV laminates. Figure 5.20 shows the EnCE of the PV laminates, with their nPD denoted by the color bar and nB indicated by the size of the circles. Clearly, the tradeoff between energy harvesting and communication is evident, where lighter colors are accompanied by smaller circle sizes. Higher EnCEs are typically observed at moderate levels of nPD and nB. Among all the tested PV technologies, the TOPCon PV laminate outperforms by delivering the best EnCE, followed by the Al-BSF(5") and IBC laminates with a comparable overall performance. This finding signifies that TOPCon offers the most balanced solution between the competing objectives within a PV-based VLC system, making it the most preferred choice among all available alternatives when the system is designed for Pareto optimality. The absolute power density and bandwidth for each PV laminate at the Pareto optimality are listed in Table 5.3.

5.5. Conclusions

In this chapter, the dynamic performance of seven commercial c-Si PV laminates used as receivers in the VLC link is investigated. These laminates include various architectures: Al-BSF(5"), Al-BSF(6"), Al-BSF(BF), IBC, PERC, SHJ, and TOPCon. The measurements are conducted under three LED colors (blue, green, and red) configured at three different irradiance levels (100, 300, and 500 W/m^2). For each lighting condition, the PV laminate is biased at various operating voltages spanning from short-circuit to open-circuit. At each operating voltage, the frequency sweep is performed by superimposing a small AC signal (ranging from 25 to 250 kHz) onto the constant DC signal of the LED light source to characterize the bandwidth of each PV laminate.

The measurement results indicate that the operating voltage of PV laminates significantly impacts their bandwidth. Increasing the operating voltage leads to decreased bandwidth, and two distinct variation ranges are identified. In the low operating voltage range, where the depletion capacitance is the controlling factor, the bandwidth decreases gradually with increasing voltage. Conversely, in the high operating voltage range, the bandwidth variation is primarily dominated by the diffusion capacitance, which changes exponentially with rising voltage. Given that the operating voltage also determines the output power of the PV laminate, it becomes apparent that achieving high bandwidth and maximizing power production are conflicting objectives. Therefore, a trade-off exists between energy harvesting and data transmission when PV cells are used as VLC receivers.

The second key observation reveals that the irradiance level also influences the bandwidth of PV laminates, where the dominant mechanism is the larger resistance R' of the PV laminate under low-light conditions. This effect is more noticeable in the low operating voltage range, where the impact of depletion capacitance on the bandwidth is

relatively minor compared to the increased resistance under low-light conditions. However, at higher operating voltages, the bandwidth is predominantly determined by the diffusion capacitance, and the effect of increased resistance under low-light conditions becomes less significant. Therefore, higher irradiance levels are more beneficial for communication when the PV laminate is operating at lower voltages. In contrast, when the PV laminate is working at its maximum power point, the impact of irradiance level on the communication performance is minor. The LED color has a marginal influence on the bandwidth of PV laminates across the entire operating voltage range and irradiance levels. This consistent bandwidth performance is advantageous to the WDM integration with LEDs and simplifies the color filter design for signal separation and demodulation with multiple PV cells. Depending on the application-specific requirements, using blue LED is more energy-efficient, while red LED enables relatively longer-distance communication.

Among the various tested PV laminates, Al-BSF(5") and Al-BSF(BF) demonstrate the least bandwidth fluctuation as the output power increases to the MPP in a VLC system, while TOPCon PV laminate emerges as the best candidate when the system is designed for the Pareto optimality between energy harvesting and communication. The impact of the architecture of the commercial c-Si PV laminates can be mainly attributed to the bulk doping concentration and the metallization design. Optimizing the metallization design to reduce the resistance benefits both energy production and communication. Higher doping concentration increases the depletion capacitance, leading to a lower bandwidth when the PV laminates are biased at low operating voltages. However, at higher operating voltages, including those around MPP, the diffusion capacitance that decreases with increased doping concentration dictates, resulting in a higher bandwidth. Therefore, a higher bulk doping concentration is preferred as long as it does not adversely affect the conversion efficiency of PV cells, since they are expected to operate at MPP to maximize energy harvesting. Future studies could focus on the optimization of parameters of doping concentration and metallization design to enhance both energy harvesting and communication.

5.6. Appendix: Determination of damping ratio condition and inductance

The equation for resonant frequency calculation is given in Equation 5.9. At lower operating voltages, the capacitance of the PV laminate is primarily determined by the depletion capacitance, which is relatively small in magnitude compared to the diffusion capacitance encountered at higher operating voltages. Therefore, the inductance effect becomes more pronounced at these lower PV operating voltages, leading to an underdamped system. As the PV operating voltage increases, both the capacitance and load resistance of the PV laminate system increase, leading to a higher damping ratio given by the Equation 5.11:

$$\zeta = \frac{R'}{2}\sqrt{\frac{C}{L}} \tag{5.11}$$

Figure 5.21 exemplifies this behavior, showcasing the system with constant inductance (L = 10 nH) but subject to different resistance and capacitance. The blue curve

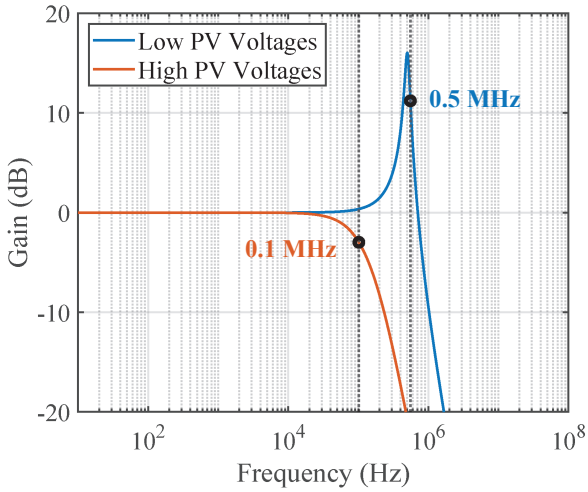

Figure 5.21: The logarithmically scaled frequency response of an equivalent RLC low-pass filter circuit, illustrating scenarios with low and high PV operating voltages. The responses are depicted by the blue curve (low PV voltage) and the red curve (high PV voltage), respectively. The increased resistance and capacitance at high PV voltages overdamped the system, and the frequency response of this system can be effectively modeled by an equivalent RC circuit.

depicts an underdamped system when the PV laminate is working at low voltages (R' = 5 mOhm, C = 1 μF), while the red curve shows the case of an overdamped system at elevated PV voltages (R' = 20 mOhm, C = 100 μF). With resistance and capacitance being the dominant components, the system transitions from underdamped ($\zeta < 1$) to overdamped ($\zeta > 1$) as the PV voltage increases, and the oscillatory response diminishes. Consequently, the frequency response closely resembles an RC low-pass filter, and the system bandwidth decreases from 0.5 MHz to 0.1 MHz. This phenomenon suggests that the RLC frequency response of the PV laminate, particularly under high operating voltages, can be effectively approximated by an equivalent RC circuit, and its bandwidth can be readily determined using Equation 5.5.

The correction after considering the inductance-induced resonance is mainly performed by comparing the bandwidths derived from equations for the cut-off frequency and for the resonant frequency, where the lower of these two values is selected as the true bandwidth of the PV laminate:

$$\frac{1}{2\pi\sqrt{LC}} < \frac{1}{2\pi R'C} \tag{5.12}$$

This condition can be further refined and becomes:

$$R' < \sqrt{\frac{L}{C}} \tag{5.13}$$

where the capacitance C is obtained from Equations 5.2 and 5.3, and the resistance R' is calculated from Equation 5.6. By incorporating Equation 5.11, the condition can be

exclusively expressed in terms of the damping ratio:

$$\zeta < \frac{1}{2} \tag{5.14}$$

To determine the inductance L, the PV laminate is first short-circuited with a wire on which the voltage drop V_{wire} is measured. The frequency sweep is then performed, and the resonant frequency f_{short} is extracted. After that, the PV laminate is disconnected from the wire and reconnected to the bias driver, which is adjusted to replicate the same voltage drop V_{wire} across the PV laminate. A second frequency sweep is then performed to extract the cut-off frequency, which is used to obtain the capacitance C_{short}. Assuming a constant capacitance and inductance across both measurements, the inductance can be derived by:

$$L = \frac{1}{4\pi^2 f_{short}^2 C_{short}} \tag{5.15}$$

6

Conclusion and outlook

6.1. Conclusions

The first part of this dissertation focused on developing a simulation framework that enabled large-scale solar photovoltaic (PV) potential assessment in the urban environment. This innovative simulation framework, presented in Chapter 2, used freely available light detection and ranging (LiDAR) data and building footprints to generate multiple geo-referenced outputs that supported urban PV planning. These outputs included:

- Highly refined and precise 3D building models based on LiDAR data.
- Annual solar irradiation maps for building envelopes, capturing spatial variations in solar exposure on roofs and facades.
- Optimized rooftop PV system layout, considering a maximum feasible module fitting scenario. Particularly for flat roofs, three mounting configurations (landscape, portrait, and dual-tilt) were examined to optimize energy utilization.
- Annual DC and AC yield of the installed rooftop PV systems, accounting for both external shading caused by the surrounding environment and mutual shadings among PV modules.
- Roof classifications based on the specific yield of installed PV systems, prioritizing PV integration on the most economically viable buildings.

When assessing DC and AC yields for facades, the open/closed ratio was derived from Google Street View images. In this approach, walls were considered as closed surfaces and were assumed to generate 100% of the computed energy yield, whereas windows were considered as open surfaces and contributed 10%. To demonstrate the applicability of this framework, a case study was conducted on all buildings of the TU Delft campus. The simulation results revealed a total PV potential of 8.1 GWh/year from rooftop and facade installations, offering valuable insights to guide campus PV integration to achieve sustainability goals.

The second part of this dissertation focused on the social and climate impacts of urban PV deployment. Specifically, Chapter 3 presented a geographic information system (GIS) based large-scale visibility assessment tool designed to quantify the roof visibility for PV planning. This tool required an additional road network input to represent the public domain and performed line-of-sight (LOS) assessments between roof surface points and hypothetical observers within that domain. Observers were represented by points along the road at a 1.7-meter height, incorporating the average eye height. The tool delivered multiple outputs, including:

- Roof binary visibility map, indicating if roof points are visible (1) or obscured (0) from the public domain.
- Roof visual amplitude (VA) map, quantifying the visual amplitude of roof cells relative to the public domain.
- PV module AC yield map, showing the potential rooftop PV system layout and corresponding annual energy production.
- PV module visibility map, categorizing PV module visibility into low, medium, and high categories.

To enhance computational efficiency, the tool incorporated optimization techniques such as parallel computing, hemisphere filtering, and adaptive LOS target selection. Additionally, each individual roof surface was optimized in terms of assessment range (radius of the area in which the visibility assessment was performed) and observer spacing (the distance between the observer points along roads). This simulation tool assisted in the multi-criteria decision-making process for urban roof PV planning.

Further, the impacts of urban PV deployment on the climate were approached by assessing its influence on the Earth's energy balance. Chapter 4 presented a novel set of numerical and analytical frameworks to quantify the radiative forcing (RF) effects associated with urban rooftop PV integration. It leveraged LiDAR data and geo-referenced material maps to accurately determine both the albedo reduction and annual PV electricity generation. Therefore, this cross-disciplinary work quantified the dual RF effects of urban PV integration:

- Enhanced positive RF from reduced albedo.
- Compensatory negative RF from the lowered CO_2 emission due to the replacement of fossil fuel with solar energy.

The workflow was executed on the entire city of Delft, and the albedo results were validated with MODIS MCD43A satellite products, where 90% of investigated coordinates lay in a deviation range of ± 0.03, indicating high reliability of the proposed methodology. The simulation results revealed that the negative RF can offset the positive RF within approximately forty days when fully integrating the rooftops in Delft with PV, assuming a grid carbon emission intensity of 437 g CO_2-eq/kWh. This demonstrates a rapid payback time considering the typical lifespan of PV modules (25 to 30 years). In a future scenario where electricity generation is predominantly based on renewables –

and the grid's carbon intensity approaches that of current c-Si PV modules – the equilibrium time for a fully integrated rooftop PV system in Delft extends significantly, reaching 1548.5 days and 623.1 days under the 13 g and 30 g CO_2-eq/kWh scenarios, respectively. As the energy system becomes more sustainable and PV manufacturing emissions continue to decrease through technological advancements, the relative contribution of albedo-induced positive radiative forcing to net climate impact will become increasingly significant. This highlights the necessity to account for albedo effects in future life cycle assessments (LCA) of PV technologies to more accurately evaluate their global warming mitigation potential.

Finally, the third part of this work focused on exploring the dual functionality of laminated crystalline silicon (c-Si) PV cells for simultaneous energy harvesting and data receiving in the visible light communication (VLC) system. Seven different c-Si architectures were studied by characterizing their bandwidth as data receivers across a voltage range from short-circuit to open-circuit under three light-emitting diode (LED) colors configured at three different irradiance levels. The key observations were:

- Increasing the voltage reduced bandwidth, first decreasing gradually and then experiencing an exponential drop. Since operating voltage also determined power output, a trade-off existed between energy harvesting and data transmission when PV cells function as VLC receiver.
- Higher plane-of-array (POA) irradiance enhanced communication when the PV laminate was operating at lower voltages but had negligible influence at the maximum power point (MPP).
- The LED color had little influence on the bandwidth of PV laminates across the operating voltage range and irradiance levels.
- The impact of PV cell architecture on bandwidth was mainly due to bulk doping concentration and metallization design. Higher doping reduced bandwidth at short circuit but increased it at higher operating voltages.

Among the tested architectures, the highest bandwidth was 215 kHz for Al-BSF(5") under short-circuit, while the lowest was 0.1 kHz for SHJ at MPP. Al-BSF cells exhibited the best communication stability from 100 kHz to 10 kHz, while SHJ showed the worst from 100 kHz to 0.1 kHz. TOPCon demonstrated the optimal balance between energy harvesting and communication for Pareto optimality. This systematic study enhanced the understanding of the fundamental interaction between light source and PV cells in the context of VLC, offering valuable insights in advancing the integration of PV cells in the urban environment for both energy harvesting and communication.

6.2. Outlook

While this work addresses the challenges of urban PV deployment from various perspectives through simulation models and experimental approaches, considerable opportunities remain for further research and investigation. This section outlines potential advancements that future researchers can explore to enhance urban PV integration.

- **Employing up-to-date input dataset with higher quality:** As mentioned in Section 2.2.2, the LiDAR data for the TU Delft campus used in the analysis was collected in 2014. Consequently, any structural or environmental changes post-2014, such as rapid vegetation growth or significant renovations on campus building roofs, are not reflected in this dataset. These exclusions can lead to discrepancies in the results, particularly if previously available surfaces have become unsuitable for PV installation due to new obstructions. The resolution of the AHN3 dataset offers about 6-10 points per square meter, with over 99.7% of the points having an accuracy within 20 cm. Such a density is insufficient to reliably detect smaller, lower-profile rooftop features, which are critical for accurate panel fitting. Fortunately, a new LiDAR dataset for the entire Netherlands (AHN5) is under ongoing collection and will be fully released soon. This updated dataset provides an improved point density of a minimum of 10 points per square meter, enabling the generation of a higher-resolution digital surface model (DSM) [211]. Although the height accuracy remains consistent with the previous version, this enhanced DSM can still offer a noticeable increase in the accuracy of the results produced by the workflow presented in Chapter 2, thanks to a more detailed representation of the urban environment. Moreover, the current algorithm assumes trees to be opaque due to the nature of the AHN3 dataset, but in reality, sunlight can penetrate through foliage, particularly in winter when trees are largely leafless, thereby potentially increasing light exposure on PV module surfaces and enhancing power output. This discrepancy between modeled and actual tree opacity needs to be addressed to improve yield predictions. This can be achieved through detailed vegetation modeling or by applying rigid scaling to tree sections in the skyline profile to refine sky view factor (SVF) calculation.

- **Curving slope modeling and automated PV yield mapping:** Curving slopes of buildings are represented by polygonal surfaces in the current models. This approximation replaces continuous curvature with multiple polygons, each defined by its own normal vector. While increasing the number of polygons can more accurately replicate curving slopes, excessively small polygons may not accommodate PV modules, resulting in no feasible panel fitting results. Meanwhile, the reconstruction of 3D building models still remains semi-automatic, and to our knowledge, several research groups are actively developing techniques for automatic 3D building model reconstruction from LiDAR data [212–214]. One of the most promising collaborations will involve the 3D BAG dataset, which provides automatically-generated building models for the entire Netherlands to the LoD 2.2 based on LiDAR and building footprints. Instead of using the off-the-shelf building models, the solar PV potential simulation can be integrated directly between the plane detection and building model reconstruction steps. This integration can bypass the noises from the reconstructed building models as presented in Chapter 2, and allow various levels of solar PV potential maps to be computed and overlaid onto the building models.

- **Improvement in the public domain representation:** In the visibility study of roof PV modules, the public domain is defined by a finite set of observer points gener-

ated from road networks, implying a one-dimensional representation. However, in reality, roads have a width dimension, and individuals standing at different positions on an identical road may lead to a different binary visibility result relative to the roof surface. Meanwhile, open spaces such as parks and squares cannot be accurately defined within the public domain because people can freely roam around such places. Therefore, exploring the possibility of using a 2D representation (such as polygons) to define the public domain and perform visibility assessments based on the grid generated from this representation is necessary. A sensitivity analysis should be performed to determine the optimal grid density of the public domain, achieving a balance between computational time and result accuracy.

- **Improvement in the human traversal model:** Observer points in the public domain are assumed to have equal weight, which may not accurately reflect real-world conditions. Streets with higher traffic, such as those near tourist attractions, are bound to have greater significance compared to the less-traveled ones. Therefore, to create a more realistic representation, it is necessary to incorporate an additional weight dimension for observer points by integrating human behavioral models and traffic data, thereby accounting for the varying importance of different locations in the public domain.

- **Improvement in the roof material information and integrability of PV:** Materials can influence the visual contrast between the PV modules and their background. The current analysis assumes an infinite visual contrast, which does not accurately reflect real-world outdoor urban environments. Integrating the material information into the large-scale LiDAR data allows for a roof-specific visual contrast identification, thereby enhancing the robustness of visibility assessment results. Meanwhile, incorporating detailed material properties improves the accuracy of albedo simulations by providing more realistic reflectivity values as input. The material classification in the Ecosystem Unit Map consists of thirty-one key units, which are further simplified into ten material classes for the application of this study. While this reduction facilitates large-scale albedo analysis, it does not fully reflect the complexity of real-world surface materials. The simplified reflectivity classification can lead to deviations in albedo simulation results. Future studies would benefit from employing more recent and higher-resolution material maps, along with a more comprehensive and representative material reflectance database to improve model accuracy and relevance. Moreover, this work does not consider the integrability of PV in building envelopes. For instance, the analysis omits considerations such as roof load capacity, potentially leading to an overestimation of roof PV potential. The performance trade-offs, such as power reduction associated with colored PV, can also be integrated into the current workflow. As the production of commercial colored PV modules matures within the PV community, these modeling frameworks can be further refined to enhance their practical applicability and accuracy.

- **Local and regional albedo monitoring:** Expanding the albedo modeling framework to capture local and regional albedo variations has broader applications.

Locally, albedo simulation helps assessing and predicting urban heat island effects caused by morphological changes, providing urban planners with insights for designing more sustainable and healthier cities. Additionally, understanding local albedo improves knowledge of surface energy balance, which directly influences soil temperature – an essential factor in agriculture and soil carbon storage. As discussed in Chapter 4, albedo is linked to global warming. Simulating albedo variation on a regional scale can help quantify each country's contribution to global warming due to morphology-induced albedo reductions. Additionally, albedo variations affect global and mesoscale climate patterns, making albedo monitoring valuable for improving meteorological analysis and weather forecasting. To enable these applications, the current albedo model shall be adapted to account for both sky view factors and ground view factors considering the influence of surrounding structures. For instance, the local albedo of an open field enclosed by buildings should include the view factors and material reflectances of building facades to deliver accurate and representative albedo simulation results.

- **Incoporate cloud dynamics and tilted PV to albedo simulation:** The dynamic behavior of moving clouds is not sufficiently accounted for in the albedo simulation framework. Overcast conditions are represented by a fully cloudy scenario, where all DSM pixels are assumed to be shaded. However, in reality, cloud coverage sometimes is partial and variable, which casts shadows on only sections of the terrain. This limitation may introduce inaccuracies, particularly during noon hours when solar irradiance is relatively high. Future efforts can be made to incorporate cloud information to refine the hourly shading profiles of each DSM pixel. This could be achieved by either employing sky images that track the movement of clouds or by incorporating a cloud coverage probability factor based on the local meteorological cloud maps. Meanwhile, PV tilt in the current simulation framework is inherited directly from the roof geometry derived from the DSM, meaning that PV panels adopt the existing roof tilt and orientation. In practice, however, PV panels are often installed at certain tilt and orientation on flat roofs to optimize energy throughput. These tilted PV panels have different sky view factors and can exhibit different radiative behaviors compared to flat-mounted PV panels. Future work can explore the influence of tilted PV panels on both albedo and net radiative forcing.

- **PV-based VLC experimental setup with individual ambient light source:** The LED light source was used for both energy harvesting and communication in this work. Future investigations into the impact of irradiance levels on communication performance in an outdoor environment could be conducted using a system with individual light sources, where one only serves as the background light for energy production, and the other is dedicated to communication.

- **VLC study with commercial PV modules:** At the module level, the impact of capacitance and resistance on the bandwidth due to the interconnection of cells should be balanced out, but the additional metallization and the junction box can introduce unwanted extra resistance, potentially degrading communication

performance. Future studies could investigate the influence of module fabrication on bandwidth to address these potential issues. Moreover, PV modules under operation are often subject to non-uniform illumination, such as partial shading, leading to cells working at different operating points. Future studies could investigate this intra-module non-uniformity on the communication bandwidth of PV modules and explore novel approaches to deal with this issue, such as innovative design of electrical circuits within the PV module.

References

[1] "Carbon Dioxide | Vital Signs - Climate Change: Vital Signs of the Planet," https://climate.nasa.gov/vital-signs/carbon-dioxide/?intent=121 (Date Accessed: 2025-02-05).

[2] "Global Temperature | Vital Signs - Climate Change: Vital Signs of the Planet," https://climate.nasa.gov/vital-signs/global-temperature/?intent=121 (Date Accessed: 2025-02-05).

[3] "Consequences of climate change - European Commission," https://climate.ec.europa.eu/climate-change/consequences-climate-change_en (Date Accessed: 2025-02-05).

[4] "The Paris Agreement | UNFCCC," https://unfccc.int/process-and-meetings/the-paris-agreement (Date Accessed: 2024-11-20).

[5] R. J. Millar, J. S. Fuglestvedt, P. Friedlingstein, J. Rogelj, M. J. Grubb, H. D. Matthews, R. B. Skeie, P. M. Forster, D. J. Frame, and M. R. Allen, "Emission budgets and pathways consistent with limiting warming to 1.5 °C," *Nature Geoscience*, vol. 10, no. 10, pp. 741–747, 2017.

[6] "Renewables 2024 - Analysis - IEA," https://www.iea.org/reports/renewables-2024 (Date Accessed: 2025-02-21).

[7] "World Energy Outlook 2024 - Analysis - IEA," https://www.iea.org/reports/world-energy-outlook-2024 (Date Accessed: 2025-02-09).

[8] "Share of electricity generation from solar energy worldwide from 2010 to 2023 [Graph]," https://www.statista.com/statistics/1302055/global-solar-energy-share-electricity-mix/ (Date Accessed: 2024-11-04).

[9] N. M. Haegel, P. Verlinden, M. Victoria, P. Altermatt, H. Atwater, T. Barnes, C. Breyer, C. Case, S. De Wolf, C. Deline, M. Dharmrin, B. Dimmler, M. Gloeckler, J. C. Goldschmidt, B. Hallam, S. Haussener, B. Holder, U. Jaeger, A. Jaeger-Waldau, I. Kaizuka, H. Kikusato, B. Kroposki, S. Kurtz, K. Matsubara, S. Nowak, K. Ogimoto, C. Peter, I. M. Peters, S. Philipps, M. Powalla, U. Rau, T. Reindl, M. Roumpani, K. Sakurai, C. Schorn, P. Schossig, R. Schlatmann, R. Sinton, A. Slaoui, B. L. Smith, P. Schneidewind, B. J. Stanbery, M. Topic, W. Tumas, J. Vasi, M. Vetter, E. Weber, A. W. Weeber, A. Weidlich, D. Weiss, and A. W. Bett, "Photovoltaics at multi-terawatt scale: Waiting is not an option," *Science*, vol. 380, no. 6640, pp. 39–42, 2023.

[10] J. Parker, "The Leeds urban heat island and its implications for energy use and thermal comfort," *Energy and Buildings*, vol. 235, p. 110636, 2021.

[11] D. V. D. Biggelaar, "Towards Decentralized Grids, EnergyBazaar: decentralized free-market energy-trade within an isolated community micro-grid," Delft University of Technology, Tech. Rep., 2018. [Online]. Available: https://repository.tudelft.nl/record/uuid:9b1f7b2f-fec8-4993-bcf7-37ab301c0d02

[12] "68% of the world population projected to live in urban areas by 2050, says UN | United Nations," https://www.un.org/uk/desa/68-world-population-projected-live-urban-areas-2050-says-un (Date Accessed: 2025-04-04).

[13] B. Cohen, "Urbanization, city growth, and the new united nations development agenda," Tech. Rep., 2015.

[14] E. Fakhraian, M. Alier, F. V. Dalmau, A. Nameni, and J. C. Guerrero, "The Urban Rooftop Photovoltaic Potential Determination," *Sustainability*, vol. 13, no. 13, p. 7447, 2021.

[15] Y. Zhou, M. Verkou, M. Zeman, H. Ziar, and O. Isabella, "A Comprehensive Workflow for High Resolution 3D Solar Photovoltaic Potential Mapping in Dense Urban Environment: A Case Study on Campus of Delft University of Technology," *Solar RRL*, vol. 6, no. 5, p. 2100478, 2021.

[16] B. Norton, P. C. Eames, T. K. Mallick, M. J. Huang, S. J. McCormack, J. D. Mondol, and Y. G. Yohanis, "Enhancing the performance of building integrated photovoltaics," *Solar Energy*, vol. 85, no. 8, pp. 1629–1664, 2011.

[17] C. Ferri, H. Ziar, T. T. Nguyen, H. van Lint, M. Zeman, and O. Isabella, "Mapping the photovoltaic potential of the roads including the effect of traffic," *Renewable Energy*, vol. 182, pp. 427–442, 2022.

[18] H. Ziar, B. Prudon, F. Y. Lin, B. Roeffen, D. Heijkoop, T. Stark, S. Teurlincx, L. de Senerpont Domis, E. G. Goma, J. G. Extebarria, I. N. Alavez, D. van Tilborg, H. van Laar, R. Santbergen, and O. Isabella, "Innovative floating bifacial photovoltaic solutions for inland water areas," *Progress in Photovoltaics: Research and Applications*, vol. 29, no. 7, pp. 725–743, 2021.

[19] P. P. J. Yang, C. S. F. Chi, Y. Wu, and S. J. Quan, "A Geodesign Method of Human-Energy-Water Interactive Systems for Urban Infrastructure Design: 10KM2 Near-Zero District Project in Shanghai," *Engineering*, vol. 4, no. 2, pp. 182–189, 2018.

[20] H. Wirth, "Recent Facts about Photovoltaics in Germany," https://www.ise.fraunhofer.de/en/publications/studies/recent-facts-about-pv-in-germany.html (Date Accessed: 2025-04-02).

[21] "Global Solar Council | Distributed Solar in Germany," https://www.globalsolarcouncil.org/our-work/empowering-people-with-solar-pv/distributed-solar-in-germany/ (Date Accessed: 2025-04-02).

[22] J. K. Kaldellis, M. Kapsali, E. Kaldelli, and E. Katsanou, "Comparing recent views of public attitude on wind energy, photovoltaic and small hydro applications," *Renewable Energy*, vol. 52, pp. 197–208, 2013.

[23] A. Zhou, R. Thomaschke, A. Wessels, S. Glunz, T. Speck, and A. Kiesel, "(Not) in my city: An explorative study on social acceptance of photovoltaic installations on buildings," *Technology in Society*, vol. 79, p. 102725, 12 2024.

[24] T. Tsoutsos, N. Frantzeskaki, and V. Gekas, "Environmental impacts from the solar energy technologies," *Energy Policy*, vol. 33, no. 3, pp. 289–296, 2005.

[25] H. Taha, "The potential for air-temperature impact from large-scale deployment of solar photovoltaic arrays in urban areas," *Solar Energy*, vol. 91, pp. 358–367, 2013.

[26] H. Akbari, S. Menon, and A. Rosenfeld, "Global cooling: Increasing world-wide urban albedos to offset CO2," *Climatic Change*, vol. 94, pp. 275–286, 2009.

[27] T. S. Elhabodi, S. Yang, J. Parker, S. Khattak, B. J. He, and S. Attia, "A review on BIPV-induced temperature effects on urban heat islands," *Urban Climate*, vol. 50, p. 101592, 2023.

[28] J. C. Ortiz Lizcano, S. Villa, Y. Zhou, G. Frantzi, K. Vattis, A. Calcabrini, G. Yang, M. Zeman, and O. Isabella, "Optimal Design of Multilayer Optical Color Filters for Building-Integrated Photovoltaic (BIPV) Applications," *Solar RRL*, no. 19, p. 2300256, 2023.

[29] J. C. O. Lizcano, I. Kaaya, H. Ziar, P. S. da Silva, Y. Zhou, M. Zeman, and O. Isabella, "Practical design of an optical filter for thermal management of photovoltaic modules," *Progress in Photovoltaics: Research and Applications*, vol. 32, no. 11, pp. 753–773, 11 2024.

[30] A. Calcabrini, M. Muttillo, R. Weegink, P. Manganiello, M. Zeman, and O. Isabella, "A fully reconfigurable series-parallel photovoltaic module for higher energy yields in urban environments," *Renewable Energy*, vol. 179, pp. 1–11, 12 2021.

[31] H. Ziar, P. Manganiello, O. Isabella, and M. Zeman, "Photovoltatronics: intelligent PV-based devices for energy and information applications," *Energy Environ. Sci*, vol. 14, p. 106, 2021.

[32] "Climate policy | Climate change | Government.nl," https://www.government.nl/topics/climate-change/climate-policy (Date Accessed: 2021-05-03).

[33] "How can we make the campus climate-neutral in 10 years? - Delta," https://delta.tudelft.nl/en/article/how-can-we-make-campus-climate-neutral-10-years (Date Accessed: 2021-01-30).

[34] "Campus development - TU Delft Campus," https://www.tudelftcampus.nl/campus-development/ (Date Accessed: 2024-11-26).

[35] "Step towards sustainable energy - Delta," https://delta.tudelft.nl/article/step-towards-sustainable-energy-clone (Date Accessed: 2025-04-08).

[36] H. Ziar, P. Manganiello, O. Isabella, and M. Zeman, "Photovoltatronics: intelligent PV-based devices for energy and information applications," *Energy & Environmental Science*, vol. 14, no. 1, pp. 106–126, 2021.

[37] S. Kucuksari, A. M. Khaleghi, M. Hamidi, Y. Zhang, F. Szidarovszky, G. Bayraksan, and Y. J. Son, "An Integrated GIS, optimization and simulation framework for optimal PV size and location in campus area environments," *Applied Energy*, vol. 113, pp. 1601–1613, 2014.

[38] K. Mainzer, S. Killinger, R. McKenna, and W. Fichtner, "Assessment of rooftop photovoltaic potentials at the urban level using publicly available geodata and image recognition techniques," *Solar Energy*, vol. 155, pp. 561–573, 2017.

[39] T. N. de Vries, J. Bronkhorst, M. Vermeer, J. C. Donker, S. A. Briels, H. Ziar, M. Zeman, and O. Isabella, "A quick-scan method to assess photovoltaic rooftop potential based on aerial imagery and LiDAR," *Solar Energy*, vol. 209, pp. 96–107, 2020.

[40] J. E. Fuentes, F. D. Moya, and O. D. Montoya, "Method for Estimating Solar Energy Potential Based on Photogrammetry from Unmanned Aerial Vehicles," *Electronics*, vol. 9, no. 12, p. 2144, 2020.

[41] M. Vermeer, "Large-scale efficient extraction of 3D roof segments from aerial stereo imagery," Tech. Rep., 2018. [Online]. Available: https://repository.tudelft.nl/record/uuid:24e59c42-b019-4fd8-a968-307eae8e4460

[42] R. Tse, C. Gold, and D. Kidner, "3D city modelling from LIDAR data," *Lecture Notes in Geoinformation and Cartography*, pp. 161–175, 2008.

[43] "What is lidar data? – Help | ArcGIS Desktop," https://desktop.arcgis.com/en/arcmap/10.3/manage-data/las-dataset/what-is-lidar-data-.htm (Date Accessed: 2024-11-26).

[44] S. Izquierdo, M. Rodrigues, and N. Fueyo, "A method for estimating the geographical distribution of the available roof surface area for large-scale photovoltaic energy-potential evaluations," *Solar Energy*, vol. 82, no. 10, pp. 929–939, 2008.

[45] L. Bergamasco and P. Asinari, "Scalable methodology for the photovoltaic solar energy potential assessment based on available roof surface area: Further improvements by ortho-image analysis and application to Turin (Italy)," *Solar Energy*, vol. 85, no. 11, pp. 2741–2756, 2011.

[46] M. C. Brito, N. Gomes, T. Santos, and J. A. Tenedório, "Photovoltaic potential in a Lisbon suburb using LiDAR data," *Solar Energy*, vol. 86, no. 1, pp. 283–288, 2012.

[47] J. B. Kodysh, O. A. Omitaomu, B. L. Bhaduri, and B. S. Neish, "Methodology for estimating solar potential on multiple building rooftops for photovoltaic systems," *Sustainable Cities and Society*, vol. 8, pp. 31–41, 2013.

[48] F. Mansouri Kouhestani, J. Byrne, D. Johnson, L. Spencer, P. Hazendonk, and B. Brown, "Evaluating solar energy technical and economic potential on rooftops in an urban setting: the city of Lethbridge, Canada," *International Journal of Energy and Environmental Engineering*, vol. 10, no. 1, pp. 13–32, 2019.

[49] M. C. Brito, P. Redweik, C. Catita, S. Freitas, and M. Santos, "3D solar potential in the urban environment: A case study in lisbon," *Energies*, vol. 12, no. 18, 2019.

[50] J. Hofierka and J. Kanuk, "Assessment of photovoltaic potential in urban areas using open-source solar radiation tools," *Renewable Energy*, vol. 34, no. 10, pp. 2206–2214, 2009.

[51] T. Santos, N. Gomes, S. Freire, M. C. Brito, L. Santos, and J. A. Tenedório, "Applications of solar mapping in the urban environment," *Applied Geography*, vol. 51, pp. 48–57, 2014.

[52] C. Catita, P. Redweik, J. Pereira, and M. C. Brito, "Extending solar potential analysis in buildings to vertical facades," *Computers and Geosciences*, vol. 66, pp. 1–12, 2014.

[53] A. Vulkan, I. Kloog, M. Dorman, and E. Erell, "Modeling the potential for PV installation in residential buildings in dense urban areas," *Energy and Buildings*, vol. 169, pp. 97–109, 2018.

[54] A. V. Vo, D. F. Laefer, A. Smolic, and S. M. Zolanvari, "Per-point processing for detailed urban solar estimation with aerial laser scanning and distributed computing," *ISPRS Journal of Photogrammetry and Remote Sensing*, vol. 155, pp. 119–135, 2019.

[55] S. M. Murshed, A. Lindsay, S. Picard, and A. Simons, "PLANTING: Computing high spatio-temporal resolutions of photovoltaic potential of 3D City models," in *Lecture Notes in Geoinformation and Cartography*. Springer Berlin Heidelberg, 2018, pp. 27–53.

[56] N. Alam, V. Coors, S. Zlatanova, and P. J. M. van Oosterom, "Resolution in photovoltaic potential computation," in *ISPRS Annals of the Photogrammetry, Remote Sensing and Spatial Information Sciences*, vol. 4, 2016, pp. 89–96.

[57] M. Amado and F. Poggi, "Solar urban planning: A parametric approach," *Energy Procedia*, vol. 48, pp. 1539–1548, 2014.

[58] T. Ramkumar, H. Gamage, E. W. Xiao, and M. Cassat, "Analysis of solar PV potential for roofs and faades in high dense residential urban scenario of Singapore," in *Journal of Physics: Conference Series*, vol. 1343, no. 1, 2019.

[59] A. Calcabrini, H. Ziar, O. Isabella, and M. Zeman, "A simplified skyline-based method for estimating the annual solar energy potential in urban environments," *Nature Energy*, vol. 4, no. 3, pp. 206–215, 2019.

[60] "The Basics of LiDAR - Light Detection and Ranging - Remote Sensing | NSF NEON | Open Data to Understand our Ecosystems," https://www.neonscience.org/resources/learning-hub/tutorials/lidar-basics (Date Accessed: 2021-05-20).

[61] "Quality description | AHN," https://www.ahn.nl/kwaliteitsbeschrijving (Date Accessed: 2021-05-20).

[62] "What is GIS? - Mapping and Geographic Information Systems (GIS) - Research Guides at University of Wisconsin-Madison," https://researchguides.library.wisc.edu/GIS (Date Accessed: 2024-12-10).

[63] "LAS Dataset To Raster (Conversion) - ArcGIS Pro | Documentation," https://pro.arcgis.com/en/pro-app/latest/tool-reference/conversion/las-dataset-to-raster.htm (Date Accessed: 2024-12-10).

[64] "Dataset: Basisregistratie Adressen en Gebouwen (BAG) - PDOK," https://www.pdok.nl/introductie/-/article/basisregistratie-adressen-en-gebouwen-ba-1 (Date Accessed: 2024-11-26).

[65] "LAS Building Multipatch (3D Analyst) - ArcGIS Pro | Documentation," https://pro.arcgis.com/en/pro-app/latest/tool-reference/3d-analyst/las-building-multipatch.htm (Date Accessed: 2021-05-21).

[66] "Decimate Modifier - Blender Manual," https://docs.blender.org/manual/en/latest/modeling/modifiers/generate/decimate.html (Date Accessed: 2021-05-21).

[67] P. Manganiello, M. Baka, H. Goverde, T. Borgers, J. Govaerts, A. van der Heide, E. Voroshazi, and F. Catthoor, "A bottom-up energy simulation framework to accurately compare PV module topologies under non-uniform and dynamic operating conditions," in *2017 IEEE 44th Photovoltaic Specialist Conference (PVSC)*. IEEE, 2017, pp. 3343–3347.

[68] "Topographic Mapping - Above Surveying," https://www.abovesurveying.com/inspection/topographic-mapping/ (Date Accessed: 2021-09-14).

[69] "3D BAG Viewer," https://3dbag.nl/en/viewer (Date Accessed: 2021-09-01).

[70] P. B. Laval, "Mathematics for Computer Graphics-Barycentric Coordinates," 2003, pp. 1–9. [Online]. Available: http://science.kennesaw.edu/~plaval/math4490/barycentric.pdf

[71] M. C. Keijzer, "A multi-surface reflected irradiance model for pyranometer corrections and PV yield calculations in complex urban geometries," Delft University of Technology, Tech. Rep., 2019. [Online]. Available: http://repository.tudelft.nl/.

[72] "What happens when an east-west solar array is not perfectly east-west?" https://www.solarpowerworldonline.com/2016/10/happens-east-west-solar-array-isnt-perfectly-east-west/ (Date Accessed: 2021-06-25).

[73] N. Alam, V. Coors, S. Zlatanova, and P. J. M. van Oosterom, "Shadow Effect on Photovoltaic Potentiality Analysis Using 3D City Models," in *The International Archives of the Photogrammetry, Remote Sensing and Spatial Information Sciences*, vol. XXXIX-B8, 2012, pp. 209–214.

[74] D. L. King, S. Gonzalez, G. M. Galbraith, and W. E. Boyson, "Performance Model for Grid-Connected Photovoltaic Inverters," Tech. Rep., 2007.

[75] A. H. M. Smets, K. Jaeger, O. Isabella, R. A. v. Swaaij, and M. Zeman, *Solar Energy: The physics and engineering of photovoltaic conversion, technologies and systems*. UIT Cambridge Limited, 2016.

[76] T. Blom and A. v. Dobbelsteen, "CO2-roadmap TU Delft," 2019.

[77] "Het potentieel van zonnestroom in de gebouwde omgeving van Nederland | PBL Planbureau voor de Leefomgeving," https://www.pbl.nl/publicaties/het-potentieel-van-zonnestroom-in-de-gebouwde-omgeving-van-nederland (Date Accessed: 2023-03-06).

[78] "Netherlands Energy Information | Enerdata," https://www.enerdata.net/estore/energy-market/netherlands/ (Date Accessed: 2025-04-08).

[79] R. Wüstenhagen, M. Wolsink, and M. J. Bürer, "Social acceptance of renewable energy innovation: An introduction to the concept," *Energy Policy*, vol. 35, no. 5, pp. 2683–2691, 2007.

[80] F. Rosa, "Building-integrated photovoltaics (BIPV) in historical buildings: Opportunities and constraints," *Energies*, vol. 13, no. 14, 2020.

[81] P. Florio, M. C. Munari Probst, A. Schüler, C. Roecker, and J. L. Scartezzini, "Assessing visibility in multi-scale urban planning: A contribution to a method enhancing social acceptability of solar energy in cities," *Solar Energy*, vol. 173, pp. 97–109, 2018.

[82] D. Oudes and S. Stremke, "Next generation solar power plants? A comparative analysis of frontrunner solar landscapes in Europe," *Renewable and Sustainable Energy Reviews*, vol. 145, p. 111101, 2021.

[83] A. d. C. Torres-Sibille, V. A. Cloquell-Ballester, V. A. Cloquell-Ballester, and M. Ã. Artacho Ramírez, "Aesthetic impact assessment of solar power plants: An objective and a subjective approach," *Renewable and Sustainable Energy Reviews*, vol. 13, no. 5, pp. 986–999, 2009.

[84] R. Chiabrando, E. Fabrizio, and G. Garnero, "On the applicability of the visual impact assessment OAISPP tool to photovoltaic plants," *Renewable and Sustainable Energy Reviews*, vol. 15, no. 1, pp. 845–850, 2011.

[85] M. Rodrigues, C. Montañés, and N. Fueyo, "A method for the assessment of the visual impact caused by the large-scale deployment of renewable-energy facilities," *Environmental Impact Assessment Review*, vol. 30, no. 4, pp. 240–246, 2010.

[86] L. A. Fernandez-Jimenez, M. Mendoza-Villena, P. Zorzano-Santamaria, E. Garcia-Garrido, P. Lara-Santillan, E. Zorzano-Alba, and A. Falces, "Site selection for new PV power plants based on their observability," *Renewable Energy*, vol. 78, pp. 7–15, 2015.

[87] J. C. Diego, S. Bonete, and P. Chías, "VIA-7 Method: A seven perceptual parameters methodology for the assessment of visual impact caused by wind and solar facilities on the landscape in cultural heritage sites," *Renewable and Sustainable Energy Reviews*, vol. 165, p. 112528, 2022.

[88] M. C. Munari Probst and C. Roecker, "Criteria and policies to master the visual impact of solar systems in urban environments: The LESO-QSV method," *Solar Energy*, vol. 184, pp. 672–687, 2019.

[89] P. Florio, G. Peronato, A. T. Perera, A. Di Blasi, K. H. Poon, and J. H. Kämpf, "Designing and assessing solar energy neighborhoods from visual impact," *Sustainable Cities and Society*, vol. 71, p. 102959, 2021.

[90] D. Lingfors, T. Johansson, J. Widén, and T. Broström, "Target-based visibility assessment on building envelopes: Applications to PV and cultural-heritage values," *Energy and Buildings*, vol. 204, p. 109483, 2019.

[91] M. Thebault, V. Clivillé, L. Berrah, and G. Desthieux, "Multicriteria roof sorting for the integration of photovoltaic systems in urban environments," *Sustainable Cities and Society*, vol. 60, p. 102259, 2020.

[92] H. Sun, C. K. Heng, S. E. R. Tay, T. Chen, and T. Reindl, "Comprehensive feasibility assessment of building integrated photovoltaics (BIPV) on building surfaces in high-density urban environments," *Solar Energy*, vol. 225, pp. 734–746, 2021.

[93] H. Sun, C. K. Heng, T. Reindl, and S. S. Y. Lau, "Visual impact assessment of coloured Building-integrated photovoltaics on retrofitted building facades using saliency mapping," *Solar Energy*, vol. 228, pp. 643–658, 2021.

[94] "Geofabrik Download Server," https://download.geofabrik.de/europe/netherlands/zuid-holland.html (Date Accessed: 2023-03-20).

[95] G. Zhang, P. J. M. van Oosterom, and E. Verbree, "Point cloud based visibility analysis: first experimental results," in *Proceedings of the Societal Geo-Innovation: Short Papers, Posters and Poster Abstracts of the 20th AGILE Conference on Geographic Information Science, Wageningen*, 2017, pp. 9–12.

[96] "Home - Basisregistratie Adressen en Gebouwen (BAG)," https://bag.basisregistraties.overheid.nl/ (Date Accessed: 2023-03-20).

[97] J. E. Azanza, "Development of a large scale rooftop PV potential assessment tool Case study: Municipality of Delft," 2019. [Online]. Available: http://repository.tudelft.nl/.

[98] I. Bogoslavskyi and C. Stachniss, "Efficient Online Segmentation for Sparse 3D Laser Scans," *PFG–Journal of Photogrammetry, Remote Sensing and Geoinformation Science*, vol. 85, no. 1, pp. 41–52, 2017.

[99] P. H. Torr and A. Zisserman, "MLESAC: A New Robust Estimator with Application to Estimating Image Geometry," *Computer Vision and Image Understanding*, vol. 78, no. 1, pp. 138–156, 2000.

[100] W. Zhang, W. Li, C. Zhang, D. M. Hanink, X. Li, and W. Wang, "Parcel-based urban land use classification in megacity using airborne LiDAR, high resolution orthoimagery, and Google Street View," *Computers, Environment and Urban Systems*, vol. 64, pp. 215–228, 2017.

[101] "UMD 2021 Uitvoeringsrichtlijnen Monumenten Delft," Tech. Rep., 2021.

[102] "Line-of-sight visibility between two points on or above terrain - MATLAB los2 - MathWorks Benelux," https://nl.mathworks.com/help/map/ref/los2.html?searchHighlight=los2&s_tid=srchtitle_los2_1 (Date Accessed: 2023-03-21).

[103] Softscape, "Walking Icon - Noun Project," https://thenounproject.com/icon/walking-4487949/ (Date Accessed: 2023-03-22).

[104] A. Van Oosterom and J. Strackee, "The Solid Angle of a Plane Triangle," *IEEE Transactions on Biomedical Engineering*, no. 2, pp. 125–126, 1983.

[105] "Four-quadrant inverse tangent - MATLAB atan2 - MathWorks Benelux," https://nl.mathworks.com/help/matlab/ref/atan2.html (Date Accessed: 2023-03-23).

[106] H. Shang and I. D. Bishop, "VISUAL THRESHOLDS FOR DETECTION, RECOGNITION AND VISUAL IMPACT IN LANDSCAPE SETTINGS," *Journal of Environmental Psychology*, vol. 20, no. 2, pp. 125–140, 2000.

[107] P. Florio, "Towards a GIS-based Multiscale Visibility Assessment Method for Solar Urban Planning," 2018. [Online]. Available: https://infoscience.epfl.ch/record/256962

[108] "Execute for-loop iterations in parallel on workers - MATLAB parfor - MathWorks Benelux," https://nl.mathworks.com/help/parallel-computing/parfor.html (Date Accessed: 2023-04-04).

[109] "Solarge SOLO," https://solarge.com/producten/solarge-solo (Date Accessed: 2021-06-22).

[110] "NIEUW: luchtfoto 2022 nu beschikbaar bij PDOK - PDOK," https://www.pdok.nl/-/nieuw-luchtfoto-2022-nu-beschikbaar-bij-pdok (Date Accessed: 2023-03-27).

[111] "ArcGIS online omgeving van Gemeente Delft," https://delft.maps.arcgis.com/home/index.html (Date Accessed: 2023-03-28).

[112] K. Von Schuckmann, M. D. Palmer, K. E. Trenberth, A. Cazenave, D. Chambers, N. Champollion, J. Hansen, S. A. Josey, N. Loeb, P. P. Mathieu, B. Meyssignac, and M. Wild, "An imperative to monitor Earth's energy imbalance," *Nature Climate Change*, vol. 6, no. 2, pp. 138–144, 2016.

[113] Y. Genchi, M. Ishisaki, Y. Ohashi, Y. Kikegawa, H. Takahashi, and A. Inaba, "Impacts of large-scale photovoltaic panel installation on the heat island effect in Tokyo," in *Fifth Conference on the Urban Climate*, 2003.

[114] H. Taha, H. Akbari, A. Rosenfeld, and J. Huang, "Residential cooling loads and the urban heat islandâĂŤthe effects of albedo," *Building and Environment*, vol. 23, pp. 271–283, 1988.

[115] D. J. Sailor, J. Anand, and R. R. King, "Photovoltaics in the built environment: A critical review," *Energy and Buildings*, vol. 253, p. 111479, 2021.

[116] Y. Zhong, H. Yu, W. Wang, and P. Yu, "Impacts of future urbanization and rooftop photovoltaics on the surface meteorology and energy balance of Lhasa, China," *Urban Climate*, vol. 51, p. 101668, 2023.

[117] V. Masson, M. Bonhomme, J. L. Salagnac, X. Briottet, and A. Lemonsu, "Solar panels reduce both global warming and urban heat island," *Frontiers in Environmental Science*, vol. 2, p. 81306, 2014.

[118] F. Salamanca, M. Georgescu, A. Mahalov, M. Moustaoui, and A. Martilli, "Citywide Impacts of Cool Roof and Rooftop Solar Photovoltaic Deployment on Near-Surface Air Temperature and Cooling Energy Demand," *Boundary-Layer Meteorology*, vol. 161, pp. 203–221, 2016.

[119] I. Lamaamar, A. Tilioua, and M. A. Hamdi Alaoui, "Thermal performance analysis of a poly c-Si PV module under semi-arid conditions," *Materials Science for Energy Technologies*, vol. 5, pp. 243–251, 2022.

[120] A. Cortes, Y. Murashita, T. Matsuo, A. Kondo, H. Shimadera, and Y. Inoue, "Numerical evaluation of the effect of photovoltaic cell installation on urban thermal environment," *Sustainable Cities and Society*, vol. 19, pp. 250–258, 2015.

[121] M. Dev and M. Surabi, "Regional climate consequences of large-scale cool roof and photovoltaic array deployment," *Environmental Research Letters*, vol. 6, p. 034001, 2011.

[122] G. A. Barron-Gafford, R. L. Minor, N. A. Allen, A. D. Cronin, A. E. Brooks, and M. A. Pavao-Zuckerman, "The Photovoltaic Heat Island Effect: Larger solar power plants increase local temperatures," *Scientific Reports*, vol. 6, pp. 1–7, 2016.

[123] S. Garshasbi, A. Khan, and M. Santamouris, "On the cooling energy penalty of urban photovoltaics: a case study in Sydney, Australia," *Energy and Buildings*, vol. 294, p. 113259, 2023.

[124] A. Khan and M. Santamouris, "On the local warming potential of urban rooftop photovoltaic solar panels in cities," *Scientific Reports*, vol. 13, pp. 1–19, 2023.

[125] A. Khan, P. Anand, S. Garshasbi, R. Khatun, S. Khorat, R. Hamdi, D. Niyogi, and M. Santamouris, "Rooftop photovoltaic solar panels warm up and cool down cities," *Nature Cities*, vol. 1, no. 11, pp. 780–790, 2024.

[126] Z. Xu, Y. Li, Y. Qin, and E. Bach, "A global assessment of the effects of solar farms on albedo, vegetation, and land surface temperature using remote sensing," *Solar Energy*, vol. 268, p. 112198, 2024.

[127] B. R. Burg, P. Ruch, S. Paredes, B. Michel, B. R. Burg, P. Ruch, S. Paredes, and B. Michel, "Placement and efficiency effects on radiative forcing of solar installations," in *AIP Conference Proceedings*, vol. 1679, 2015.

[128] H. Akbari, H. Damon Matthews, and D. Seto, "The long-term effect of increasing the albedo of urban areas," *Environmental Research Letters*, vol. 7, p. 024004, 2012.

[129] A. Hu, S. Levis, G. A. Meehl, W. Han, W. M. Washington, K. W. Oleson, B. J. Van Ruijven, M. He, and W. G. Strand, "Impact of solar panels on global climate," *Nature Climate Change*, vol. 6, pp. 290–294, 2015.

[130] G. F. Nemet, "Net radiative forcing from widespread deployment of photovoltaics," *Environmental Science and Technology*, vol. 43, pp. 2173–2178, 2009.

[131] H. Ziar, F. F. Sönmez, O. Isabella, and M. Zeman, "A comprehensive albedo model for solar energy applications: Geometric spectral albedo," *Applied Energy*, vol. 255, p. 113867, 2019.

[132] "Ecosystem Unit map | CBS," https://www.cbs.nl/en-gb/background/2017/12/ecosystem-unit-map (Date Accessed: 2024-08-14).

[133] A. M. Baldridge, S. J. Hook, C. I. Grove, and G. Rivera, "The ASTER spectral library version 2.0," *Remote Sensing of Environment*, vol. 113, pp. 711–715, 2009.

[134] "SMARTS: Simple Model of the Atmospheric Radiative Transfer of Sunshine | Grid Modernization | NREL," https://www.nrel.gov/grid/solar-resource/smarts.html (Date Accessed: 2024-08-15).

[135] "Meteonorm Version 8 - Meteonorm (en)," https://meteonorm.com/en/meteonorm-version-8 (Date Accessed: 2024-08-16).

[136] "Asphalt and road construction in the Netherlands | TNO," https://www.tno.nl/en/sustainable/infrastructure/asphalt/ (Date Accessed: 2024-08-15).

[137] M. Schelhaas and A. Clerkx, "State of the forests in the Netherlands, 2012-2013," https://research.wur.nl/en/publications/state-of-the-forests-in-the-netherlands-2012-2013 (Date Accessed: 2024-08-15).

[138] "LAMBDA 1050+ UV/Vis/NIR Spectrophotometer | PerkinElmer," https://www.perkinelmer.com/product/lambda-1050-2d-base-inst-no-sw-l6020055 (Date Accessed: 2024-08-15).

[139] M. K. Gupta, K. J. Bumtariya, H. A. Shukla, P. Patel, and Z. Khan, "Methods for Evaluation of Radiation View Factor: A Review," *Materials Today: Proceedings*, vol. 4, pp. 1236–1243, 2017.

[140] Z. Wang, C. Schaaf, A. Lattanzio, D. Carrer, I. Grant, M. Román, F. Camacho, Y. Yu, J. Sánchez-Zapero, and J. Nickeson, "Global Surface Albedo Product Validation Best Practices Protocol. Version 1.0." NASA, Tech. Rep., 2019.

[141] E. S. Gadelmawla, M. M. Koura, T. M. Maksoud, I. M. Elewa, and H. H. Soliman, "Roughness parameters," *Journal of Materials Processing Technology*, vol. 123, pp. 133–145, 2002.

[142] M. Aida, "Urban albedo as a function of the urban structure - A model experiment - Part I," *Boundary-Layer Meteorology*, vol. 23, no. 4, pp. 405–413, 1982.

[143] Y. Zhou, D. Wilmink, M. Zeman, O. Isabella, and H. Ziar, "A geographic information system-based large scale visibility assessment tool for multi-criteria photovoltaic planning on urban building roofs," *Renewable and Sustainable Energy Reviews*, vol. 188, p. 113885, 2023.

[144] G. Wohlfahrt, E. Tomelleri, and A. Hammerle, "The albedo-climate penalty of hydropower reservoirs," *Nature Energy*, vol. 6, pp. 372–377, 2021.

[145] R. M. Bright and T. L. O'Halloran, "A monthly shortwave radiative forcing kernel for surface albedo change using CERES satellite data," 2019.

[146] R. Bright and T. O'Halloran, "Developing a monthly radiative kernel for surface albedo change from satellite climatologies of Earth's shortwave radiation budget: CACK v1.0," *Geoscientific Model Development*, vol. 12, pp. 3975–3990, 2019.

[147] R. M. Bright, W. Bogren, P. Bernier, and R. Astrup, "Carbon-equivalent metrics for albedo changes in land management contexts: relevance of the time dimension," *Ecological Applications*, vol. 26, pp. 1868–1880, 2016.

[148] "CO2 Emissions from Fuel Combustion | OECD iLibrary," https://www.oecd-ilibrary.org/energy/co2-emissions-from-fuel-combustion_22199446 (Date Accessed: 2024-09-26).

[149] F. Joos, R. Roth, J. S. Fuglestvedt, G. P. Peters, I. G. Enting, W. Von Bloh, V. Brovkin, E. J. Burke, M. Eby, N. R. Edwards, T. Friedrich, T. L. Frölicher, P. R. Halloran, P. B. Holden, C. Jones, T. Kleinen, F. T. Mackenzie, K. Matsumoto, M. Meinshausen, G. K. Plattner, A. Reisinger, J. Segschneider, G. Shaffer, M. Steinacher, K. Strassmann, K. Tanaka, A. Timmermann, and A. J. Weaver, "Carbon dioxide and climate impulse response functions for the computation of greenhouse gas metrics: A multi-model analysis," *Atmospheric Chemistry and Physics*, vol. 13, pp. 2793–2825, 2013.

[150] "MODIS/Terra+Aqua BRDF/Albedo Model Parameters Daily L3 Global - 500m - LAADS DAAC," https://ladsweb.modaps.eosdis.nasa.gov/missions-and-measurements/products/MCD43A1#overview (Date Accessed: 2024-10-09).

[151] S. Wang, A. P. Trishchenko, and X. Sun, "Simulation of canopy radiation transfer and surface albedo in the EALCO model," *Climate Dynamics*, vol. 29, pp. 615–632, 2007.

[152] J. C. Blakesley, G. Koutsourakis, D. E. Parsons, N. A. Mica, S. Balasubramanyam, and M. G. Russell, "Sourcing albedo data for bifacial PV systems in complex landscapes," *Solar Energy*, vol. 266, p. 112144, 2023.

[153] J. A. Sobrino, B. Franch, R. Oltra-Carrió, E. F. Vermote, and E. Fedele, "Evaluation of the MODIS Albedo product over a heterogeneous agricultural area," *International Journal of Remote Sensing*, vol. 34, no. 15, pp. 5530–5540, 2013.

[154] O. Coddington, K. S. Schmidt, P. Pilewskie, W. J. Gore, R. W. Bergstrom, M. Román, J. Redemann, P. B. Russell, J. Liu, and C. C. Schaaf, "Aircraft measurements of Spectral surface albedo and its consistency with ground-based space-borned observations," *Journal of Geophysical Research Atmospheres*, vol. 113, no. 17, p. 17209, 9 2008.

[155] K. Yan, H. Li, W. Song, Y. Tong, D. Hao, Y. Zeng, X. Mu, G. Yan, Y. Fang, R. B. Myneni, and C. Schaaf, "Extending a Linear Kernel-Driven BRDF Model to Realistically Simulate Reflectance Anisotropy over Rugged Terrain," *IEEE Transactions on Geoscience and Remote Sensing*, vol. 60, 2022.

[156] C. Reichel, A. Müller, L. Friedrich, S. Herceg, M. Mittag, and D. H. Neuhaus, "CO2 emissions of silicon photovoltaic modules-impact of module design and production location," in *WCPEC-8, 8th World Conference on Photovoltaic Energy Conversion*, 2022.

[157] A. A. Lacis, "Albedo Feedbacks," in *Encyclopedia of Paleoclimatology and Ancient Environments*. Dordrecht: Springer Netherlands, 2009, pp. 2–4. [Online]. Available: https://doi.org/10.1007/978-1-4020-4411-3_2

[158] "Wetter und Klima - Deutscher Wetterdienst - Climate maps Europe - Surface albedo - Monthly values," https://www.dwd.de/EN/ourservices/rcccm/int/rcccm_int_sal.html?nn=790954 (Date Accessed: 2025-05-28).

[159] R. Boers, F. Bosveld, H. Klein Baltink, W. Knap, E. Van Meijgaard, and W. Wauben, "Observing and Modelling the Surface Radiative Budget and Cloud Radiative Forcing at the Cabauw Experimental Site for Atmospheric Research (CESAR), the Netherlands, 2009-17," *Journal of Climate*, vol. 32, no. 21, pp. 7209–7225, 2019.

[160] "IoT connected devices worldwide 2019-2030 | Statista," https://www.statista.com/statistics/1183457/iot-connected-devices-worldwide/ (Date Accessed: 2023-10-23).

[161] C. M. Schieler, K. M. Riesing, B. C. Bilyeu, J. S. Chang, A. S. Garg, N. C. Gilbert, A. J. Horvath, R. S. Reeve, B. S. Robinson, J. P. Wang, S. Piazzolla, W. T. Roberts, J. M. Kovalik, and B. Keer, "On-orbit demonstration of 200-Gbps laser communication downlink from the TBIRD CubeSat," in *Free-Space Laser Communications XXXV*. SPIE, 2023, p. 1241302.

[162] "Satellite Communication | TNO," https://www.tno.nl/en/sustainable/space-scientific-instrumentation/satellite-communication/laser-satellite-communication/ (Date Accessed: 2023-10-25).

[163] H. Haas, E. Sarbazi, H. Marshoud, and J. Fakidis, "Visible-light communications and light fidelity," *Optical Fiber Telecommunications VII*, pp. 443–493, 2020.

[164] L. Feng, R. Q. Hu, J. Wang, P. Xu, and Y. Qian, "Applying VLC in 5G networks: Architectures and key technologies," *IEEE Network*, vol. 30, no. 6, pp. 77–83, 2016.

[165] H. Claussen, L. T. Ho, and L. G. Samuel, "An overview of the femtocell concept," *Bell Labs Technical Journal*, vol. 13, no. 1, pp. 221–245, 2008.

[166] M. S. Islim, E. Xie, H. Haas, M. D. Dawson, S. Viola, R. X. Ferreira, N. Bamiedakis, X. He, S. Watson, R. V. Penty, A. E. Kelly, S. Videv, I. H. White, and E. Gu, "Towards 10Gb/s orthogonal frequency division multiplexing-based visible light communication using a GaN violet micro-LED," *Photonics Research*, vol. 5, no. 2, pp. A35–A43, 2017.

[167] H. Elgala, R. Mesleh, and H. Haas, "Indoor optical wireless communication: Potential and state-of-the-art," *IEEE Communications Magazine*, vol. 49, no. 9, pp. 56–62, 2011.

[168] Z. Wang, D. Tsonev, S. Videv, and H. Haas, "On the Design of a Solar-Panel Receiver for Optical Wireless Communications with Simultaneous Energy Harvesting," *IEEE Journal on Selected Areas in Communications*, vol. 33, no. 8, pp. 1612–1623, 2015.

[169] H. Haas, L. Yin, Y. Wang, and C. Chen, "What is LiFi?" *Journal of Lightwave Technology*, vol. 34, no. 6, pp. 1533–1544, 2016.

[170] A. Jovicic, J. Li, and T. Richardson, "Visible light communication: opportunities, challenges and the path to market," *IEEE Communications Magazine*, vol. 51, no. 12, pp. 26–32, 2013.

[171] J. T. Wu, C. W. Chow, Y. Liu, C. W. Hsu, and C. H. Yeh, "Performance enhancement technique of visible light communications using passive photovoltaic cell," *Optics Communications*, vol. 392, pp. 119–122, 2017.

[172] "Wi-Fi Boosts New, Ultrafast Li-Fi Standards - IEEE Spectrum," https://spectrum.ieee.org/lifi-standards (Date Accessed: 2024-02-20).

[173] M. M. Hossain, S. Ray, J. S. Cheong, L. Qiao, A. N. Baharuddin, M. M. Hella, J. P. David, and M. M. Hayat, "Low-Noise Speed-Optimized Large Area CMOS Avalanche Photodetector for Visible Light Communication," *Journal of Lightwave Technology*, vol. 35, no. 11, pp. 2315–2324, 2017.

[174] N. Lorriere, N. Betrancourt, M. Pasquinelli, G. Chabriel, J. Barrere, L. Escoubas, J. L. Wu, V. Bermudez, C. M. Ruiz, and J. J. Simon, "Photovoltaic solar cells for outdoor lifi communications," *Journal of Lightwave Technology*, vol. 38, no. 15, pp. 3822–3831, 2020.

[175] X. Chen, C. Min, and J. Guo, "Visible Light Communication System Using Silicon Photocell for Energy Gathering and Data Receiving," *International Journal of Optics*, vol. 2017, 2017.

[176] S. M. Kim and J. S. Won, "Simultaneous reception of visible light communication and optical energy using a solar cell receiver," *International Conference on ICT Convergence*, pp. 896–897, 2013.

[177] B. Malik and X. Zhang, "Solar panel receiver system implementation for visible light communication," *Proceedings of the IEEE International Conference on Electronics, Circuits, and Systems*, pp. 502–503, 2016.

[178] Z. Wang, D. Tsonev, S. Videv, and H. Haas, "Towards self-powered solar panel receiver for optical wireless communication," in *2014 IEEE International Conference on Communications (ICC)*. IEEE, 6 2014, pp. 3348–3353. [Online]. Available: http://ieeexplore.ieee.org/document/6883838/

[179] W.-H. Shin, S.-H. Yang, D.-H. Kwon, and S.-K. Han, "Self-reverse-biased solar panel optical receiver for simultaneous visible light communication and energy harvesting," *Optics express*, vol. 24, no. 22, pp. A1300–A1305, 2016.

[180] M. Kong, B. Sun, R. Sarwar, J. Shen, Y. Chen, F. Qu, J. Han, J. Chen, H. Qin, and J. Xu, "Underwater wireless optical communication using a lens-free solar panel receiver," *Optics Communications*, vol. 426, pp. 94–98, 2018.

[181] S. Das, E. Poves, J. Fakidis, A. Sparks, S. Videv, and H. Haas, "Towards Energy Neutral Wireless Communications: Photovoltaic Cells to Connect Remote Areas," *Energies*, vol. 12, no. 19, p. 3772, 2019.

[182] S. Das, A. Sparks, E. Poves, S. Videv, J. Fakidis, and H. Haas, "Effect of Sunlight on Photovoltaics as Optical Wireless Communication Receivers," *Journal of Lightwave Technology*, vol. 39, no. 19, pp. 6182–6190, 2021.

[183] M. Kong, J. Lin, C. H. Kang, C. Shen, Y. Guo, X. Sun, M. Sait, Y. Weng, H. Zhang, T. K. Ng, and B. S. Ooi, "Toward self-powered and reliable visible light communication using amorphous silicon thin-film solar cells," *Optics Express*, vol. 27, no. 24, pp. 34 542–34 551, 2019.

[184] P. P. Manousiadis, K. Yoshida, G. A. Turnbull, and I. D. Samuel, "Organic semiconductors for visible light communications," *Philosophical Transactions of the Royal Society A*, vol. 378, no. 2169, 2020.

[185] B. Arredondo, B. Romero, J. M. Sánchez Pena, A. Fernández-Pacheco, E. Alonso, R. Vergaz, and C. de Dios, "Visible Light Communication System Using an Organic Bulk Heterojunction Photodetector," *Sensors*, vol. 13, no. 9, pp. 12 266–12 276, 2013.

[186] C. Vega-Colado, B. Arredondo, J. C. Torres, E. López-Fraguas, R. Vergaz, D. Martín-Martín, G. Del Pozo, B. Romero, P. Apilo, X. Quintana, M. A. Geday, C. de Dios, and J. M. Sánchez-Pena, "An All-Organic Flexible Visible Light Communication System," *Sensors*, vol. 18, no. 9, p. 3045, 2018.

[187] L. Salamandra, L. La Notte, C. Fazolo, M. Di Natali, S. Penna, L. Mattiello, L. Cinà, R. Del Duca, and A. Reale, "A comparative study of organic photodetectors based on P3HT and PTB7 polymers for visible light communication," *Organic Electronics*, vol. 81, p. 105666, 2020.

[188] S. Zhang, D. Tsonev, S. Videv, S. Ghosh, G. A. Turnbull, I. D. W. Samuel, and H. Haas, "Organic solar cells as high-speed data detectors for visible light communication," *Optica*, vol. 2, no. 7, pp. 607–610, 2015.

[189] I. Tavakkolnia, L. K. Jagadamma, R. Bian, P. P. Manousiadis, S. Videv, G. A. Turnbull, I. D. Samuel, and H. Haas, "Organic photovoltaics for simultaneous energy harvesting and high-speed MIMO optical wireless communications," *Light, science & applications*, vol. 10, no. 1, 2021.

[190] N. A. Mica, R. Bian, P. Manousiadis, L. K. Jagadamma, I. Tavakkolnia, H. Haas, H. Haas, G. A. Turnbull, G. A. Turnbull, I. D. W. Samuel, and I. D. W. Samuel, "Triple-cation perovskite solar cells for visible light communications," *Photonics Research*, vol. 8, no. 8, pp. A16–A24, 2020.

[191] J. Fakidis, S. Videv, H. Helmers, and H. Haas, "0.5-Gb/s OFDM-Based Laser Data and Power Transfer Using a GaAs Photovoltaic Cell," *IEEE Photonics Technology Letters*, vol. 30, no. 9, pp. 841–844, 2018.

[192] J. Fakidis, H. Helmers, and H. Haas, "Simultaneous Wireless Data and Power Transfer for a 1-Gb/s GaAs VCSEL and Photovoltaic Link," *IEEE Photonics Technology Letters*, vol. 32, no. 19, pp. 1277–1280, 2020.

[193] C. Monokroussos, R. Gottschalg, A. N. Tiwari, G. Friesen, D. Chianese, and S. Mau, "The effects of solar cell capacitance on calibration accuracy when using a flash simulator," *IEEE 4th World Conference on Photovoltaic Energy Conference*, vol. 2, pp. 2231–2234, 2006.

[194] S. Braun, G. Micard, and G. Hahn, "Solar Cell Improvement by using a Multi Busbar Design as Front Electrode," *Energy Procedia*, vol. 27, pp. 227–233, 2012.

[195] N. Chen, D. Tune, F. Buchholz, R. Roescu, M. Zeman, O. Isabella, and V. D. Mihailetchi, "Stable passivation of cut edges in encapsulated n-type silicon solar cells using Nafion polymer," *Solar Energy Materials and Solar Cells*, vol. 258, p. 112401, 2023.

[196] "SR-1901PT - Spectral Evolution," https://spectralevolution.com/product/sr-1901pt/ (Date Accessed: 2024-07-11).

[197] D. A. van Nijen, M. Muttillo, R. Van Dyck, J. Poortmans, M. Zeman, O. Isabella, and P. Manganiello, "Revealing capacitive and inductive effects in modern industrial c-Si photovoltaic cells through impedance spectroscopy," *Solar Energy Materials and Solar Cells*, vol. 260, p. 112486, 2023.

[198] "LOANA solar cell analysis system," http://www.pv-tools.de/products/loana-system/loana-start.html (Date Accessed: 2024-02-27).

[199] "Thermal Effects on White LED Chromaticity | DigiKey," https://www.digikey.com/en/articles/thermal-effects-on-white-led-chromaticity (Date Accessed: 2023-11-14).

[200] M. Kong, C. H. Kang, O. Alkhazragi, X. Sun, Y. Guo, M. Sait, J. A. Holguin-Lerma, T. K. Ng, and B. S. Ooi, "Survey of energy-autonomous solar cell receivers for satellite-air-ground-ocean optical wireless communication," *Progress in Quantum Electronics*, vol. 74, p. 100300, 2020.

[201] M. Pravettoni, D. Poh, J. Prakash Singh, J. Wei Ho, and K. Nakayashiki, "The effect of capacitance on high-efficiency photovoltaic modules: A review of testing methods and related uncertainties," *Journal of Physics D: Applied Physics*, vol. 54, no. 19, 2021.

[202] A. Edler, M. Schlemmer, J. Ranzmeyer, and R. Harney, "Understanding and Overcoming the Influence of Capacitance Effects on the Measurement of High Efficiency Silicon Solar Cells," *Energy Procedia*, vol. 27, pp. 267–272, 2012.

[203] S. J. Yaqoob, A. L. Saleh, S. Motahhir, E. B. Agyekum, A. Nayyar, and B. Qureshi, "Comparative study with practical validation of photovoltaic monocrystalline module for single and double diode models," *Scientific Reports*, vol. 11, no. 1, pp. 1–14, 2021.

[204] J. Thongpron, K. Kirtikara, and C. Jivacate, "A method for the determination of dynamic resistance of photovoltaic modules under illumination," *Solar Energy Materials and Solar Cells*, vol. 90, no. 18-19, pp. 3078–3084, 11 2006.

[205] K. Sindhubala and B. Vijayalakshmi, "Receiver intend to reduce ambient light noise in visible-light communication using solar panels," *Journal of Engineering Science and Technology Review*, vol. 10, no. 1, pp. 84–90, 2017.

[206] G. E. Bunea, K. E. Wilson, Y. Meydbray, M. P. Campbell, and D. M. De Ceuster, "Low light performance of mono-crystalline silicon solar cells," in *Conference Record of*

the 2006 IEEE 4th World Conference on Photovoltaic Energy Conversion, WCPEC-4, vol. 2. IEEE Computer Society, 2006, pp. 1312–1314.

[207] T.-K. Kim, "Visible light communication using RGB LED for machine-to-machine communication," *International Journal of Mechanical Engineering and Technology*, vol. 9, no. 13, pp. 951–958, 2019.

[208] P. Kusuma, P. M. Pattison, and B. Bugbee, "From physics to fixtures to food: current and potential LED efficacy," *Horticulture Research*, vol. 7, no. 1, pp. 1–9, 2020.

[209] "Rayleigh Scattering - an overview | ScienceDirect Topics," https://www.sciencedirect.com/topics/physics-and-astronomy/rayleigh-scattering (Date Accessed: 2024-02-23).

[210] "Pareto Optimality - an overview | ScienceDirect Topics," https://www.sciencedirect.com/topics/engineering/pareto-optimality (Date Accessed: 2024-02-29).

[211] Y. Pluijmers, "Aerial Lidar en AHN," 2023. [Online]. Available: http://www.dijkmonitoring.nl/_sitefiles/file/2023workshops/AerialLidar.pdf

[212] N. Haala and M. Kada, "An update on automatic 3D building reconstruction," *ISPRS Journal of Photogrammetry and Remote Sensing*, vol. 65, no. 6, pp. 570–580, 2010. [Online]. Available: http://dx.doi.org/10.1016/j.isprsjprs.2010.09.006

[213] Y. Xiao, C. Wang, X. H. Xi, and W. M. Zhang, "A comprehensive framework of building model reconstruction from airborne LiDAR data," in *IOP Conference Series: Earth and Environmental Science*, vol. 17, no. 1, 2014.

[214] H. Ledoux, F. Biljecki, B. Dukai, K. Kumar, R. Peters, J. Stoter, and T. Commandeur, "3dfier: automatic reconstruction of 3D city models," *Journal of Open Source Software*, vol. 6, no. 57, p. 2866, 2021.

Acknowledgement

They say beginnings are always the hardest, but closing a chapter of life turns out to be just as tough. From joining the SET master's program to defending my PhD, this life chapter took a stretch of 8 years to complete (seriously, I keep thinking how many '8 years' do I even get in a lifetime), and this journey has been a rollercoaster of challenges, joys, frustrations, and achievements. But I did not ride this rollercoaster alone. Through every high and low, I have always been surrounded by beautiful souls who made this ride less lonely and the drops less daunting, for which I am deeply grateful.

First and foremost, I would like to express my gratitude to my promoters, Prof.dr. Miro Zeman and Prof.dr. Olindo Isabella, for giving me this opportunity to work on this topic. Their support throughout my PhD was invaluable, providing constructive feedback that helped me orient my research, refine my work, and grow professionally as a researcher. I am equally grateful for their support beyond work, as they were always available when I was going through tough times in my life. I would also like to express my gratitude to my co-promoter, Dr. Hesan Ziar, with whom I had the pleasure of working on a range of interesting research topics. To me, these projects were not just collaborative research efforts, but also continuous learning experiences. He always gave me the freedom to manage my own research while offering support whenever I needed. I greatly appreciated his interdisciplinary mindset and ability to draw connections across domains, which often helped me to transform what might have been a narrow technical practice into a more impactful scientific contribution. I would also like to take this opportunity to extend my gratitude to the committee members: Prof.dr. P.J.M. van Oosterom, Prof.dr. Rebecca Saive, Prof.dr. Sven Stremke, Prof.dr. Arthur Weeber, and Prof.dr. Arno Smets. Thank you for your time and insightful feedback.

Second, I would like to thank the Master students I supervised during my PhD: Dennis, Shreedatta, Ishan, and Aya. It was truly a pleasure working with you. Rather than top-down supervision, we were more working as a team on various group projects. Your contributions were fundamental, and I learned a lot from you during our collaborations. I would also like to thank the supporting staff for their essential assistance: Mark, Sharmila, Marieke, Carla, Brenda, Mitch, Nienke, and Sandra. Besides, I would like to convey my appreciation to all the technicians for their strong technical support: Martijn, Stefaan, Engin, Tim, Shuang, Bernardus, Daragh, and Mehmet.

Third, I would like to thank the rest of the beautiful people that I met in the group during my PhD: Alba, Afshin, Alex, Alestair, Andres, Annika, Arturo, Brain, Can, Carlos, Chengjian, Daniel, David, Daniele, Elif, Engin, Federica, Filip, Gianluca, Govind, Guangtao, Haoxu, Imran, Ivan, Jannis, Jasmeen, Jin, Jonathan, Juan Camilo, Katarina, Klaas, Liqi, Luana, Leo, Maarten, Malte, Manvika, Mare, Marta, Maryam, Michiel, Mirco, Mohammad, Moumita, Niels, Nithin, Patrizio, Paul, Paula, Peer (special thanks for checking the summary translation!), Reinder, Rene, Riccardo, Rik, Robin, Rudi, Sathya, Sachin, Sargol, Sebastian, Sho, Su, Sowmya, Sreejith, Thierry, Thomas, Urvashi, Vladimir, Wenx-

ian, Yi, Yida, Yifeng, Yilei, Yingwen, Youri, Yudai, Zain and Ziying. We've shared so many wonderful moments and lasting memories together – being at the lunch tables, gathering at the coffee corners after lunch, attending conferences, exploring museums, chilling on the grass at Delftse Hout, throwing party at someone's place, battling at arcade games, running around at laser tag, hanging out at festivals, having deep talks till late night... My life is so much better with you in it, and I hope I've made yours a little better too.

Additionally, I would like to thank the great artists for their remarkable music and films. Their works are like beacons in the gloomy night, helping me navigate around all those bumps in life and rediscover my inner peace. A special shoutout to 'Human Sadness' by Julian Casablancas, to 'One Crowded Hour' by Augie March, to Ryo Fukui, to Fishmans, to Jim Jarmusch... Finally, I want to thank my parents, my brother, my girlfriend Kelly, my cat Chibi, and my friends: Anna, Angqi, Alon, Adytia, Bo, Chaya, Elias, Hannah, Hanchen, Hao, Heran, Isabella, Jenneken, John, Kyle, Kong, Lawrence, Lukas, Lyu, Max, Mason, Mike, Phil, Rob, Robert, Thorben, Vasili, and Xun. With you by my side, I know I can face any challenges in life.

List of publications

Peer-reviewed publications:

1. **Y. Zhou**, M. Verkou, M. Zeman, H. Ziar, and O. Isabella, *A Comprehensive Workflow for High Resolution 3D Solar Photovoltaic (PV) Potential Mapping in Dense Urban Environment: A Case Study on Campus of Delft University of Technology*, Solar RRL **6**, 2100478 (2021). [1] [2]

2. **Y. Zhou**, D. Wilmink, M. Zeman, O. Isabella, and H. Ziar, *A geographic information system-based large scale visibility assessment tool for multi-criteria photovoltaic planning on urban building roofs*, Renewable and Sustainable Energy Reviews **188**, 113885 (2023).

3. **Y. Zhou**, A. Ibrahim, M. Muttillo, H. Ziar, O. Isabella, and P. Manganiello, *Investigation on simultaneous energy harvesting and visible light communication using commercial c-Si PV cells: Bandwidth characterization under colored LEDs*, Energy **311**, 133387 (2024).

4. **Y. Zhou**, S. Marathera, M. Zeman, O. Isabella, and H. Ziar, *Assessing the dual radiative consequences of urban PV integration: albedo change and radiative forcing dynamics*, Applied Energy **401**, 126544 (2025).

5. J. Langer, Z. Kwee, **Y. Zhou**, O. Isabella, Z. Ashqar, J. Quist, A. Praktiknjo, K. Blok, *Geospatial analysis of Indonesia's bankable utility-scale solar PV potential using elements of project finance*, Energy **283**, 128555 (2023).

6. J. C. O. Lizcano, S. Villa, **Y. Zhou**, G. Frantzi, K. Vattis, A. Calcabrini, G. Yang, M. Zeman, O. Isabella, *Optimal Design of Multilayer Optical Color Filters for Building-Integrated Photovoltaic (BIPV) Applications*, Solar RRL **7**, 2300256 (2023).

7. J. C. O. Lizcano, I. Kaaya, H. Ziar, P. S. Da Silva, **Y. Zhou**, M. Zeman, O. Isabella, *Practical design of an optical filter for thermal management of photovoltaic modules*, Progress in Photovoltaics: Research and Applications **32**, 753-773 (2024).

8. P. Procel, **Y. Zhou**, M. Verkou, M. Leonardi, D. Di Girolamo, G. Giuliano, O. Dupre, Y. Blom, M.R. Vogt, R. Santbergen, F. Rametta, M. Foti, C. Gerardi, M. Zeman, O. Isabella, *PV multiscale modelling of perovskite / silicon two-terminal devices: from accurate cell performance simulation to energy yield prediction*, Solar Energy Materials and Solar Cells **293**, 113864 (2025).

[1] This article wins the best urban energy institution paper 2021.
[2] This article is featured on the cover of Solar RRL, Volume 6, Issue 5.

Early research contributions:

1. Y. Mi, L. Wen, Z. Wang, D. Cao, R. Xu, Y. Fang, **Y. Zhou**, Y. Lei, *Fe (III) modified BiOCl ultrathin nanosheet towards high-efficient visible-light photocatalyst*, Nano Energy **30**, 109-117 (2016).

2. Y. Mi, L. Wen, Z. Wang, D. Cao, H. Zhao, **Y. Zhou**, F. Grote, Y. Lei, *Ultra-low mass loading of platinum nanoparticles on bacterial cellulose derived carbon nanofibers for efficient hydrogen evolution*, Catalysis Today **262**, 141-145 (2016).

Conference proceedings:

1. **Y. Zhou**, A. Ibrahim, M. Muttillo, P. Manganiello, H. Ziar, O. Isabella, *Bandwidth Characterization of c-Si Solar Cells as VLC Receiver under Colored LEDs*, 8th International Conference on Smart and Sustainable Technologies (SpliTech), IEEE (2023)

Conference contributions as the first author:

1. **Y. Zhou**, M. Verkou, M. Zeman, H. Ziar, and O. Isabella, *High Resolution 3D Solar Photovoltaic (PV) Potential Map for TU Delft Campus and Real Estate*, 38th EU PVSEC, **5CO.12.3 (oral)**, online, (2021).

2. **Y. Zhou**, D. Wilmink, M. Zeman, O. Isabella, and H. Ziar, *A GIS-based Large-Scale Visibility Assessment Tool for PV Planning on Building Roofs*, WCPEC-8, **4CO.9.2 (oral)**, Milan, Italy, (2022).

3. **Y. Zhou**, D. Wilmink, M. Zeman, O. Isabella, and H. Ziar, *A GIS-based Large-Scale Visibility Assessment Tool for PV Planning on Building Roofs*, PVSEC-33, **WeP-22-8 (poster)**, Nagoya, Japan, (2022).

4. **Y. Zhou**, A. Ibrahim, M. Muttillo, P. Manganiello, H. Ziar, and O. Isabella, *Bandwidth Characterization of c-Si Solar Cells as VLC Receiver under Colored LEDs*, Splitech, **PV: Photovoltatronics (oral)**, Split-Bol, Croatia, (2023).

5. **Y. Zhou**, S. Marathera, M. Zeman, O. Isabella, and H. Ziar, *Effect of Urban Development on Local Albedo Based on LiDAR Data*, 40th EU PVSEC, **4CO.9.6 (oral)**, Lisbon, Portugal, (2023).

Curriculum Vitae

Yilong Zhou was born in China on February 27, 1993. He earned his bachelor's degree from the East China University of Science and Technology (ECUST), Shanghai, in 2015. During the final year of his undergraduate journey, he studied as an exchange student at the Technical University of Ilmenau, Germany, where he conducted his bachelor's thesis on *Enhanced PEC Water Splitting Ability: Thin Film TiO_2 Deposited by ALD on 3D-Nanocone Based Substrate* within the 3D-nanostructure group led by Prof. Dr. Yong Lei.

In 2017, he joined Delft University of Technology (TU Delft) for a Master's program in Sustainable Energy Technology (SET). Upon successfully completing his thesis on *Novel Doping-Free Metal-Oxide Carrier Selective Passivating Contacts for Solar Cells*, he began his PhD in 2020 in the Photovoltaic Materials and Devices (PVMD) group. Under the supervision of Prof. Dr. Miro Zeman, Prof. Dr. Olindo Isabella, and Dr. Hesan Ziar, his research focuses on PV potential in urban environments and innovative PV module demonstrators. He specializes in large-scale sustainable engineering, satellite-based remote sensing data analysis, and spatial analysis.